UNIVERSIDAD DE CHILE
FACULTAD DE CIENCIAS FÍSICAS Y MATEMÁTICAS
ESCUELA DE POSTGRADO Y EDUCACIÓN CONTINUA

THERMAL BEHAVIOR AND STABILITY STUDY OF A LITHIUM-ION BATTERY PACK WITH AIR COOLING

TESIS PARA OPTAR AL GRADO DE
DOCTOR EN CIENCIAS DE LA INGENIERÍA, MENCIÓN FLUIDODINÁMICA

EDWIN BLADIMIR PACCHA HERRERA

PROFESOR GUÍA:
DR. WILLIAMS CALDERÓN MUÑOZ

MIEMBROS DE LA COMISIÓN:
DR. ÁLVARO VALENCIA MUSALEM
DR. CHRISTIAN IHLE BASCUÑÁN
DR. GERARDO DIAZ OLIVARES
DR. ARAMIS PÉREZ MORA

SANTIAGO DE CHILE
2022

COMPORTAMIENTO TÉRMICO Y ESTUDIO DE ESTABILIDAD DE UN PAQUETE DE BATERÍAS DE IONES DE LITIO CON ENFRIAMIENTO POR AIRE

Las aplicaciones de las baterías de iones de litio están emergiendo cada vez más en la actualidad y es fundamental prestar especial atención a su rendimiento térmico. El mecanismo de enfriamiento juega un papel esencial como sistema de gestión térmica de la batería. El presente trabajo tiene como objetivo evaluar el comportamiento térmico de un módulo de baterías refrigerado por aire compuesto de baterías cilíndricas de iones de litio de tipo $LiCoO_2$ (LCO) 26650 (diámetro 26 mm y altura 65 mm).

Primero, se evaluó una sola celda comparando tres enfoques: un modelo térmico de parámetros concentrados o resistencia térmica despreciable, un modelo 3D de dinámica de fluidos computacional (CFD) y un modelo electroquímico. Antes de proveer más detalles, es importante definir la tasa C, la cual representa la medida de corriente de carga o descarga que se aplica a una celda con respecto a su capacidad nomimal. Por ejemplo, para una batería de 1 Ah cargada, 1C representa la corriente que descarga completamente la celda en una hora. A una tasa de descarga de 0.5C, el modelo electroquímico presenta el error más bajo. No obstante, este modelo proporciona el error más alto a 1.5C. Bajo un perfil de corriente que emula un ciclo de conducción, todos los modelos proporcionan el mismo orden de error.

Luego, se evaluó el comportamiento térmico de un módulo de baterías con quince (3×5) celdas cilíndricas. Durante la descarga a convección libre, la temperatura de las células aumenta a medida que aumenta la corriente de descarga. La zona central del módulo de baterías alcanza la temperatura más alta al final de la descarga. Las mediciones del perfil de temperatura de las celdas concuerdan con las simulaciones numéricas. Además, se aplicó un modelo basado en filtro de partículas para estimar la temperatura del paquete de baterías durante el proceso de enfriamiento. Esta técnica predice satisfactoriamente la temperatura de las celdas y se puede implementar en el monitoreo en línea de las mismas. Dicho modelo también proporciona la evolución artificial de parámetros. Alternativamente, se llevaron a cabo simulaciones numéricas mediante CFD, cuya ejecución demanda un tiempo considerable, logrando mejorar ligeramente la estimación de la temperatura de las celdas en comparación con el filtro de partículas.

Para tomar en consideración las condiciones extremas de funcionamiento de la batería, se describió el embalamiento o fuga térmica mediante un modelo de abuso térmico que se basa en la reacción térmica que tiene lugar en los distintos componentes de la batería. En términos generales, la fuga térmica ocurre cuando la tasa de generación de calor en la celda es mayor que el calor liberado. La temperatura de inicio de la fuga térmica depende principalmente del tipo de celda, la temperatura ambiente y el mecanismo de enfriamiento. Se describieron parámetros adimensionales que tienen en cuenta esos factores. Para una celda de LCO en convección libre, la fuga térmica se activa a una temperatura por sobre los 145 °C.

Abstract

Applications of lithium-ion batteries are increasingly emerging nowadays and it is crucial to pay special attention to their thermal performance. The cooling mechanism plays an essential role as battery thermal management system of the batteries. The present work aims to evaluate the thermal behavior of an air-cooled battery module comprised of LiCoO$_2$ (LCO) 26650 (26 mm diameter and 65 mm height) cylindrical Li-ion batteries.

First, a single cell was evaluated by comparing three approaches: a thermal lumped model, a 3D computational fluid dynamics (CFD) model, and an electrochemical model. Before providing more details, it is important to define what C-rate is. This represents the measurement of the charging or discharging current applied to a cell with respect to its rated capacity, for example, for a 1 Ah fully charged cell, 1C rate represents the current that completely discharges the battery in one hour. At 0.5C discharge rate, the electrochemical model has the lower error. Nonetheless, this model give the higher error at 1.5C. Under a current profile of a driving cycle, all the models provide the same order of error.

Then, the thermal behavior of a battery module with fifteen (3 × 5) cylindrical LCO cells was evaluated. During discharging at free convection, the temperature of cells rises as discharging current increases. The central zone of the battery module reach the highest temperature at the end of discharging. Measurements of the temperature profile of cells are in good agreement with numerical simulations. Furthermore, a model based on particle filtering was applied to estimate the temperature of the battery pack during the cooling-down process. This technique predicts well the temperature of cells and it can be implemented in online monitoring of cells. It also performs the artificial evolution of parameters in the model. Alternatively, CFD simulations were performed, characterized to be a time consuming process to simulate the cooling-down and slightly improves the temperature estimation of cells comparing with particle filter.

To take into consideration extreme operating conditions of the battery, thermal runaway was described by a thermal abuse model which is based on the heat reaction that take place in the distinct components of the battery. In general terms, thermal runaway occur when the rate of heat generation in the cell is greater than the released heat. Onset temperature of thermal runaway mainly depends on the type of cell, ambient temperature and cooling mechanism. Dimensionless parameters that take into account those factors were described. For a LCO cell under free convection, thermal runaway is triggered above 145 °C.

In memory of my parents: Bruno and María.
To my family, friends and teachers.

Acknowledgments

I would like to express my gratitude to my advisor, Dr. Williams Calderón, for his continued guidance with wisdom, patience and sens of humor.

Many thanks to Dr. Álvaro Valencia, Dr. Christian Ihle, Dr. Gerardo Díaz and Dr. Aramis Pérez for their valuable advice as members of the thesis committee.

I wish to acknowledge the help provided by Dr. Marcos Orchard and Dr. Kamal Medjaher. My sincere thanks go to *monsieur* Dr. Francisco Jaramillo for his friendship and collaboration.

The assistance in the laboratory provided by Mr. Jorge Reyes is greatly appreciated.

Thanks to the members of The Production Engineering Laboratory at The National Engineering School of Tarbes (France) for their cooperation and friendship.

I wish to show my appreciation to all my friends during my stay in Chile: Joseph, Natalia, Eduardo, Sebastián, Charlie, Paulo, Armando, Berenice, Manuel, Juan, Cinthia, Felipe, Marina, *Txema*, Pablo, Diana and many others.

I would also like to thank my family and friends in Ecuador who encourage me all the time. Thanks to my wife Jenny their unfailing support and continuous encouragement.

Content

List of Tables

List of Figures

Nomenclature

Acronyms

3D	Three dimensional
BTM	Battery thermal management
CFD	Computational fluid dynamics
Col.	Column
DoD	Depth of discharge
ECM	Equivalent circuit model
EIS	Electrochemical impedance spectroscopy
EV	Electric vehicle
HPPC	Hybrid pulse power characterization
HWFET	The Highway Fuel Economy Test
LCO	Lithium cobalt oxide
LFP	Lithium iron phosphate
Li	Lithium
LIB	Lithium-ion battery
LTI	linear time-independent
MSMD	Multi scale multi domain
NTGK	Newman, Tiedemann, Gu and Kim model
OCV	Open circuit voltage
P2D	Pseudo two dimensional
PCM	Phase change material
PDF	Probability density function
PF	Particle filter
RMS	Root mean square
SIMPLE	Semi-Implicit Method for Pressure Linked Equations

SOC	State-of-charge
SOH	State-of-health
SST	Shear stress transport
TR	Thermal runaway
UDF	User defined function

Constants and variables

$\hat{n}$	Unit normal vector
$\overline{Nu_D}$	Average Nusselt number across a bank of tubes
d	Battery diameter (m)
$\vec{V}$	Velocity ($\mathrm{m \cdot s^{-1}}$)
A	Area ($\mathrm{m^2}$). Frequency factor ($\mathrm{s^{-1}}$)
a_s	Active surface area per electrode unit volume ($\mathrm{m^{-1}}$)
c	Fraction of concentration
C_1	Constant for Nusselt number
C_N	Nominal capacity of the battery (Ah)
C_p	Heat capacity ($\mathrm{JK^{-1}}$)
c_p	Specific heat capacity ($\mathrm{J \cdot kg \cdot K^{-1}}$)
$c_{s,\mathrm{e}}$	Li concentration at the surface of solid particles
$c_{s,max}$	Maximum Li concentration in solid particles
E_a	Activation energy (J)
F	Faraday constant (96485 $\mathrm{C \cdot mol^{-1}}$)
$f_\pm$	Electrolyte activity coefficient
H	Enthalpy ($\mathrm{J \cdot kg^{-1}}$)

h	Heat transfer coefficient ($\text{Wm}^{-2}\text{K}^{-1}$)	Z	Impedance (Ω)
h_e	Sensible enthalpy ($\text{J} \cdot \text{kg}^{-1}$)	$\mathbf{w}$	Weights in particle filtering
I	Current (A)	$\mathbf{x}$	State vector
i_0	Exchange current density (Am^{-2})	$\mathbf{z}$	Measurement vector
j^{Li}	Current density (Am^{-2})	C	Rate of current discharge
kc, k_f	Thermal conductivity of cell and fluid ($\text{Wm}^{-1}\text{K}^{-1}$)	e	Internal energy (J)
		k	Time instant (s)
m	Specific mass or density ($\text{kg} \cdot \text{m}^{-3}$)	Nu	Nusselt number
n	Constant for Nusselt number	Ra	Rayleight number
N_s	Number of particles		

Greek Symbols

p, q	Probability density functions	α	Stretching factor, degree of conversion of cathode
Pr	Prandtl number		
Q	Heat transfer rate (W)	β	Stretching factor, thermal expansion coefficient (K^{-1})
q_ech	Electrochemical heat (W)		
Q_{cc}	Heat transfer through a conduction resistance (W)	ε	Emissivity
		κ	Ionic conductivity of electrolyte ($\text{S} \cdot \text{m}^{-1}$)
Q_{ht}	Total heat transfer rate (W)		
R	Universal gas constant (8.31 $\text{J} \cdot \text{mol}^{-1}\text{K}^{-1}$)	κ_m	Conductivity of electrolyte ($\text{S} \cdot \text{m}^{-1}$)
R_o	Ohmic resistance (Ω)	μ	kinematic viscosity ($\text{m}^{-2}\text{s}^{-1}$)
R_T	Total internal resistance (Ω)	∇	Divergence operator
R_{cc}	Conduction resistance ($\text{K} \cdot \text{W}^{-1}$)	ν	Noise measurement vector
R_{CT}	Charge transfer resistance (Ω)	ω	Noise process vector
R_in	Internal thermal resistance ($\text{K} \cdot \text{W}^{-1}$)	ϕ	Potential (V)
		Ψ	Parameter dependent on temperature
R_{out}	External thermal resistance ($\text{K} \cdot \text{W}^{-1}$)		
		ρ	Density ($\text{kg} \cdot \text{m}^{-3}$)
Re_D	Reynolds number for a tube with diameter D	σ	Steffan-Boltzmann constant $\sigma = 5.67 \cdot 10^{-8}$ $\text{Wm}^{-2}\text{K}^{-4}$, electrical conductivity (S/m)
S_h	Source term (Wm^{-3})		
T	Temperature (K)	τ	Thermal time constant (s^{-1})
t	Time (s)	ε	Volume fraction in electrode
T^*	Dimensionless temperature		

Subscripts

t_{TR}	Thermal runaway time (s)	$+$	Relative to cathode
U_eq	Equilibrium potential of the electrode (V)	$-$	Relative to anode
		0	Initial value
V	Voltage (V)	a	Anode, activation

amb	Ambient	ne	Negative electrode
c	Cell, cathode	OC	Open circuit
$comb$	combined	rad	radiation
$conv$	convection	ref	Reference
el	Electrolyte	s	Solid phase, surface
f	Fluid	sei	Solid electrolyte interface layer
in	Internal	sur	surround
N	Nominal	$surf,c$	Cell surface

Introduction

The use of electric vehicles (EVs) and hybrid electric vehicles (HEVs) is becoming increasingly relevant to reduce oil consumption and avoid environmental pollution. Nevertheless, the primary challenge for clean energy vehicles is the improvement of the energy storage system, which is comprised of lithium-ion batteries (LIBs). Furthermore, the study of LIBs is crucial in terms of energy efficiency and safety of several kind of electric and electronic devices.

LIBs were commercialized for the first time by Sony Corporation in August 1991 and have undergone noticeable progress in capacity, performance, and cost reduction. Nowadays, there exist LIB manufacturers for EVs that provide batteries sizing from 16 kWh (Mitsubishi I model) to 100 kWh (Tesla S model) [1].

In general, batteries are classified into primary (non-rechargeable) and secondary (rechargeable). There exist many types of secondary batteries utilized as energy source in EVs: lead-acid, nickel-iron, nickel-zinc, nickel-cadmium, nickel-metal hydrate (NiMH), lithium-ion (Li-ion), aluminum-air, zinc-air, etc. Moreover, flexible LIBs with high energy density have been created recently [2].

However, a weak point of LIBs is that their performance is chiefly dependent on temperature. This implies that it is highly important to study heat generation inside a battery, the relationship between temperature and capacity degradation, heat dissipation, and other topics. Consequently, a suitable thermal management system is a priority for optimal performance and safety of the battery [3].

As part of battery thermal management (BTM) system, there have been developed external cooling mechanisms such as active cooling with air or liquid, passive cooling with phase change material (PCM) and heat pipe [4]. Air forced as an active BTM system has been extensively used because of its simplicity, low cost of implementation and maintenance [5].

In order to model a LIB, there exist some models such as electrochemical, thermal, equivalent circuit model, or a combination among them, which may provide heat generation rate, the temperature profile of the battery, and many other important parameters. To study the thermal behavior of a battery module, it is necessary to couple the heat generation and the cooling system models.

There exist a few approaches to study the behavior of a BTM system for battery modules without expensive computational resources. For instance, Hu et al. [6] considered the cooling system as a linear time-independent (LTI) system and proposed a Foster network thermal

model for a battery module. This approach considerably reduces the simulation time comparing to conventional CFD. Tian et al. [7] presented a pioneer work in order to reconstruct the temperature field for a battery module by using an estimator based on Kalman filter approach. Another tool to face state estimation is particle filter which is used specially for nonlinear problems.

The main goal in this work is to evaluate the thermal behavior of a lithium-ion battery pack with air cooling by developing a study supported by experiments and numerical simulations. First, three models were implemented numerically to study the thermal behavior of LIBs: a lumped model, a 3D-CFD model, and an electrochemical approach using the NTGK model. Furthermore, voltage was simulated using NTGK formulation. All of these simulations were done at the same physical conditions of the experimental tests, at constant current discharge rate, and under a driving cycle. A 26650 lithium cobalt oxide (LCO) battery was used. Parameter estimation was carried out to determinate the values of unknown parameters and electrochemical impedance spectroscopy (EIS) was applied to measure the internal resistance of the battery.

Furthermore, thermal performance of a battery module with fifteen cells was analyzed. Experimental discharging and cooling-down tests were performed and compared to numerical simulations. For cooling-down process at forced convection, a particle filter was implemented to estimate online the surface temperature of each cell. A fractal thermal approach was used as a process model of the cells.

If a battery undergoes elevated temperatures, it may lead up to thermal runaway (TR). During this phenomenon, a chain of exothermic reactions may occur; even fire and explosions may be present. This phenomenon may be studied through a thermal abuse model proposed by Hatchard et al. [8] and extended by Kim et al. [9]. This approach is applied in this work to study TR by using a thermal lumped model for a cylindrical cell. In order to describe the thermal stability of the cell, physical conditions given by non-dimensional numbers that lead a Li-ion battery to thermal runaway are described.

This work is organized as follows: Chapter 1 presents a literature review of the developed topics. Chapter 2 describes the methodology to study the thermal behavior of a single cell and a battery pack including thermal runaway occurrence. The implementation of a model based on particle filter to estimate the cell surface temperature in a battery module is is also described in this Chapter. Results are presented in Chapter 3.

Research problem, hypothesis and objectives

Research problem statement

The weak point regarding the operation of many electric devices and electric vehicles is their energy supply and storage system comprised of lithium-ion batteries. Battery performance is strongly dependent on temperature, and at elevated temperatures, a critical event (named thermal runaway) may occur. An approach to estimate the temperature behavior of cells through a probabilistic and numerical approach will contribute to improve the battery thermal management system.

Studies on thermal stability of LIBs from a mathematical point of view are scarce, and an approach on the relationship between the thermal behavior of LIBs and electric vehicles' driving conditions are limited as well.

The following research question is formulated:

How to predict the thermal behavior of an air-cooled Li-ion battery module from the standard operating conditions straightforwardly until thermal runaway occurrence oriented to electric vehicle applications?

Hypotheses

The general hypothesis is formulated as follows:

Thermal behavior parameters of a LIB module such as temperature, convection coefficient, and cooling characteristics may be described satisfactorily in a wide range of operating conditions by using a lumped model for the cell domain even under thermal abuse conditions.

The following specific hypotheses are proposed:

1. Linear stability analysis based on a thermal abuse model describes physical parameters which let the temperature profile of a battery increases until thermal runaway occurs.
2. The thermal performance of the battery module depends on a proper estimation of the heat generation rate and convection coefficient.
3. CDF modeling of the battery module including driving data of an EV will corroborate

the heating and cooling phenomena predicted by a mathematical model to be proposed.

Objectives

General objective

To evaluate the thermal behavior of a LIB module with air cooling including thermal abuse conditions by developing a theoretical study supported by experiments and numerical results.

Specific objectives

1. Determine the physical conditions that lead a lithium-ion battery to thermal runaway under thermal abuse conditions.
2. Characterize the thermal behavior of a lithium-ion battery module with air as a coolant under natural convection and forced convection experimentally.
3. Carry out CFD numerical simulations of the battery arrangement focusing on the cooling effect and heat generation rate.
4. Predict the thermal performance of the battery module based on real driving data of an electric vehicle.

Contributions

This work present some contributions regarding the thermal performance of lithium-ion batteries:

- The most common approaches for thermal modeling of lithium-ion batteries are evaluated.
- Thermal parameters of a LCO battery are determined.
- Heat generation rate of a LCO cell is described experimentally.
- Temperature of cells under natural and forced convection are tested and computed numerically.
- Temperature of a battery module under forced convection is estimated based on a particle filter approach. Thus, it is possible to monitor cells in real time by indirect measurements.
- Thermal runaway of a lithium-ion battery is studied based on the thermal abuse model.

Moreover, the following works were published:

- E. Paccha-Herrera, W. R. Calderón-Muñoz, M. Orchard, F. Jaramillo and K. Medjaher, "Thermal Modeling Approaches for a LiCoO$_2$ Lithium-ion Battery—A Comparative Study with Experimental Validation," *Batteries*, vol. 6, pp. 40, 2020.
- R. A. Toledo-Quiroz, W. R. Calderón-Muñoz and E. Paccha-Herrera, "Modular packaging effect on thermal performance of LiCoO$_2$ lithium-ion cells: An experimental study," *Journal of Energy Storage*, vol. 44, pp. 103394, 2021.

Chapter 1

Literature review

This chapter introduces some basic definitions to understand how LIBs work. Moreover, a discussion about thermal management systems for batteries, thermal models and abuse conditions is also covered. A description about particle filtering to estimate a state of a system is presented as well.

1.1 Working principle and types of lithium-ion batteries

Nowadays, the industry of electric vehicles (EVs) requires an increasing production of LIBs. Figure 1.1 shows the most common types of LiBs configurations that have been used in EV applications as well as for other general purposes.
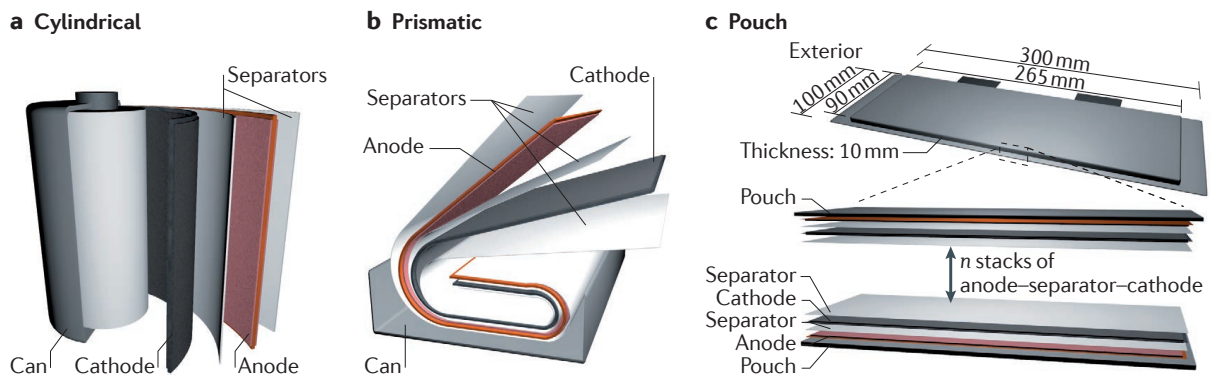
Figure 1.1: Common configurations of lithium-ion batteries: (**a**) cylindrical, (**b**) prismatic, and (**c**) pouch [10].

The main components of LIBs are: anode (negative electrode), cathode (positive electrode), separator, electrolyte and collector plates as shown in Figure 1.2a. A solid electrolyte interface (SEI) layer is formed on the anode surface usually during the first charge cycles as shown Figure 1.2b. The SEI layer is crucial for the lifetime of the battery because it prevents electrolyte decomposition [11]. During the discharge process (when a load is connected to the

battery terminals), lithium ions inside the active material of negative electrode travel to the positive electrode; ions are diffused through the SEI layer passing the porous separator and moving through the electrolyte. At the same time, an equal quantity of electrons flows to the anode current collector. Thereby, a redox reaction occurs (oxidization at the anode and reduction at the cathode). During the charging process, an opposite movement of lithium ions and electrons occurs, and the redox reaction is inverted as well [12]. Here is an example of reactions during the discharging process of an LCO cell [13]:

$$\text{Cathode}: \ \text{Li}_{1-x}\text{CoO}_2 + x\text{Li}^+ + x\text{e}^- \xrightarrow{\text{discharge}} \text{LiCoO}_2 \tag{1.1a}$$

$$\text{Anode}: \ \text{Li}_x\text{C}_6 \xrightarrow{\text{discharge}} x\text{Li}^+ + x\text{e}^- + \text{C}_6 \tag{1.1b}$$

$$\text{Full reaction in the cell}: \ \text{LiC}_6 + \text{CoO}_2 \xrightarrow{\text{discharge}} \text{C}_6 + \text{LiCoO}_2; \ E = 3.7\,\text{V at } 25\,^\circ\text{C} \tag{1.1c}$$

(a)   (b)
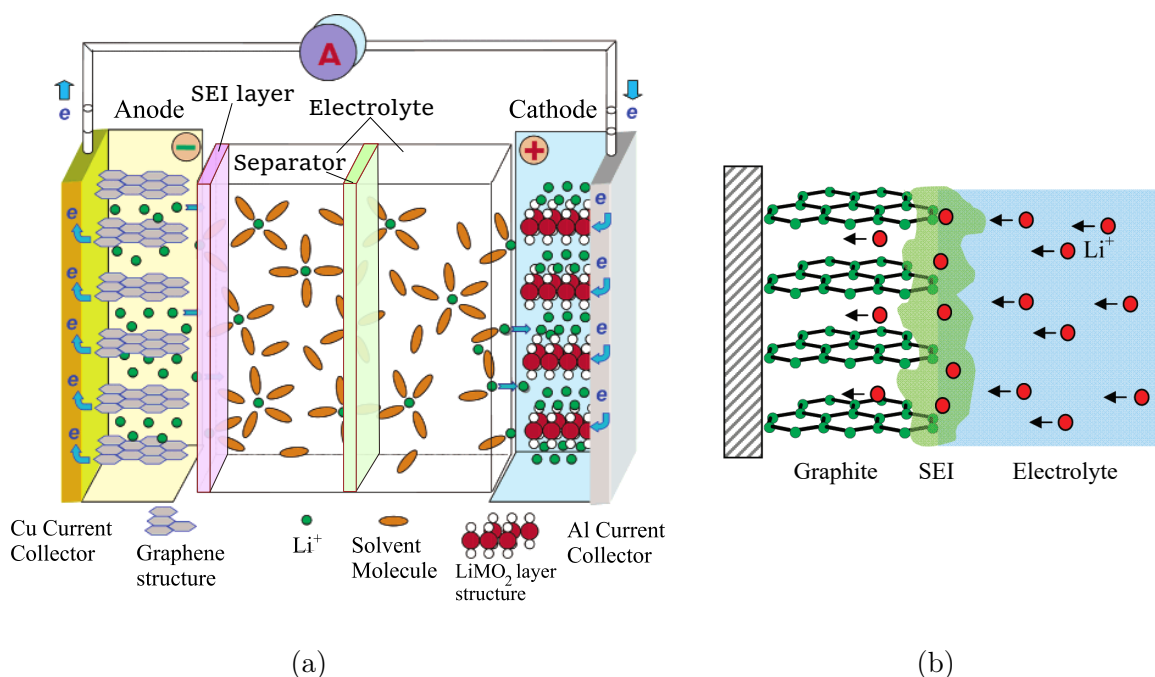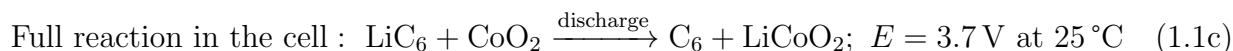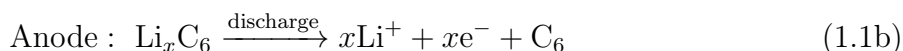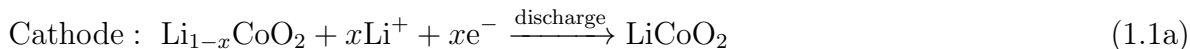
Figure 1.2: Working principle of a lithium-ion battery: (**a**) Scheme of discharge process. Adapted from [14]. (**b**) Solid electrolyte interface (SEI) layer formation process [15].

The LIB electrodes consist of active material, a conductive filler, a polymer binder, and electrolyte [16]. The anode active material is made of graphite or carbon materials such as Li_xC_6. The cathode active material describes the chemistry of a battery and it is typically made of layered oxides, e.g., lithium cobalt oxide (LCO - LiCoO_2), lithium manganese oxide (LMO - LiMn_2O_4), lithium nickel cobalt aluminum oxide (NCA - $\text{LiNi}_{0.8}\text{Co}_{0.15}\text{Al}_{0.05}\text{O}_2$), lithium nickl manganese cobalt oxide (NMC - $\text{LiNi}_x\text{Mn}_y\text{Co}_{1-x-y}\text{O}_2$), lithium iron phosphate (LFP - LiFePO_4), lithium titanium oxide (LTO - $\text{Li}_4\text{T}_5\text{O}_{12}$), among others. Some characteristics of Li-ion cells according to the cathode material are shown in Table 1.1. The electrolyte is a lithium salt (e.g., lithium hexafluorophosphate, LiPF_6) in an organic solvent (e.g., ethylene carbonate, dimethyl carbonate, and propylene carbonate) [1, 17]. Regarding to the separator, it is commonly made of a porous membrane of polyethylene (PE) or polypropylene (PP). The collector plates are usually made from copper and aluminum, for anode and cathode,

Table 1.1: Characteristics of different types of cathodes [1, 19].

Cathode material	Specific capacity (Ah/kg)	Characteristics	Thermal runaway temperature (°C)
LCO	155	High energy density. Good cycle life. Thermal stability issue. Used in portable electronics.	150
LMO	100-120	Great thermal stability. Acceptable cycle life. Used in power tools and EVs.	250
NCA	180	Excellent energy and cycle life. Sensitive to moisture. Used in selected electronics and EVs.	210
NMC	160	Good energy, thermal stability, and cycle life. Patent issues. EVs and industrial uses.	210
LFP	160	Good thermal stability and cycle life. Minor energy density. High endurance applications.	270

respectively. LMO and LFP batteries have had more opportunities in EVs applications in the last years [18].

1.2 Battery thermal management system

A battery system (such as an EV battery) consists of a set of battery packs, while a battery pack is a group of modules, modules are formed by single cells. The target of a battery thermal management (BTM) system is to guarantee that cells operate at an adequate temperature with small fluctuations of temperature and voltage. Besides, it should have compactness and a suitable ventilation system [20, 21]. According to the instructions of battery manufacturers, the reliable operating temperatures required by a majority of current automotive LIBs are given in the following range: charging from $0\,°C$ to $45\,°C$, and discharging from $-20\,°C$ to $55\,°C$ [22]. Nevertheless, Zhao et al. [23] suggest that an optimum temperature range of operation for LIBs is 25-40 °C. It is convenient that the temperature difference between modules might be less than $5\,°C$ [24].

There exist some mechanisms used for battery cooling, and the main ones are listed as follows:

- Air cooling. It is the more straightforward and low-priced method; it is used for heating/ventilation as well. The main issue is the low thermal conductivity of the air. For instance, if the cell temperature is above $66\,°C$, it would be decreased no more than $14\,°C$ by using air forced convection [21] and then, the battery would operate in the limit of the suggested temperature range.

- Liquid cooling. Because of the heat capacity of liquids, it has a better performance than air cooling, especially in abuse conditions. This system has some disadvantages such as more weight and the risk of leakage [25]. Strategies for liquid cooling may include

direct or indirect systems. Indirect mechanisms of cooling may include tube cooling, micro channels, jacket cooling, and heat pipe [4].

- Phase change material (PCM) cooling. Many works have been developed in regards to this passive method which was firstly proposed by Mills and Al-Hallaj [26] in 2005 by using paraffin wax. At discharging, PCM absorbs heat, while during standby PCM may reject heat from the batteries. Nevertheless, PCM can melts under hot environments or due to progressive use of the cell [4].

Battery module configurations based on air and liquid cooling are discussed in [4]. Characteristics of many thermal management methods, especially the thermal behavior of PCMs are compared and discussed in [21]. Design principles of existing and emerging thermal management systems are reported in [27]. Moreover, Mondal et al. [28] studied vortex generation for active BTM. Hunt et al. [29] experimented with pouch cells and proposed tab cooling rather than surface cooling in order to increase the lifespan of a pack.

1.2.1 ANSYS Fluent

ANSYS Fluent is a computational package widely used to solve incompressible, compressible, laminar and turbulent fluid flow problems. Integral equations for the conservation of mass, momentum, energy an other scalars are numerically computed based on finite volume discretization. Steady-state or transient studies can be implemented. Furthermore, distinct heat transfer modes can be computed, including natural, forced, and mixed convection. Two numerical solvers are available in Fluent: pressure-based and density-based approach. Generally, the pressure-based method is used for low-speed incompressible flows, while the density-based approach is mainly implemented for high-speed compressible flows [30].

1.3 Battery modeling

This section exposes the thermal models solved in the present study.

1.3.1 3D-CFD model

The energy equation employed by CFD solver to model the battery as a solid is governed by [30]:

$$\frac{\partial}{\partial t}\left(\rho h_{\mathrm{e}}\right) + \nabla \cdot \left(\vec{V}\rho h_{\mathrm{e}}\right) = \nabla \cdot (k\nabla T) + S_h, \tag{1.2}$$

where ρ is the density, $h_{\mathrm{e}} = \int c_p \mathrm{d}T$ is the sensible enthalpy, c_p is the specific heat, k is the thermal conductivity, T is the temperature, S_h is the volumetric source term, and the velocity $\vec{V}$ is obtained from the motion of the fluid. In the present study, instead of solving flow equations around the battery, an experimental heat transfer coefficient was utilized.

1.3.2 Thermal lumped model

Energy balance for a single cell also can be written as:

$$C_p \frac{\partial T}{\partial t} = Q_{conv} + Q_{rad} + Q_{gen}, \tag{1.3}$$

where C_p is heat capacity, Q_{gen} is the heat generation (source term), and heat exchange rate is transferred by convection Q_{conv} and radiation Q_{rad}.

This work employs a thermal lumped model proposed by Forgez et al. [31], which simplifies Eq. 1.3 into Eq. 1.4:

$$\frac{dT_s}{dt} = \frac{T_{amb} - T_s}{C_p \left(R_{in} + R_{out}\right)} + \frac{Q_{gen} R_{out}}{C_p \left(R_{in} + R_{out}\right)}, \tag{1.4}$$

where T_s, and T_{amb} are the surface temperature of the battery, and ambient temperature, respectively. The heat capacity, conduction resistance in the inner of the cell R_{in}, and external resistance R_{out} between the surface of the cell and surrounding fluid; can be determined via parameter identification such as Refs. [32, 33]. An equivalent thermal circuit is illustrated in Figure 1.3, where Q_{gen} is represented as a source of current, and C_p allows to store energy as a capacitor. Internal cell temperature T_{in} could be compute as well.
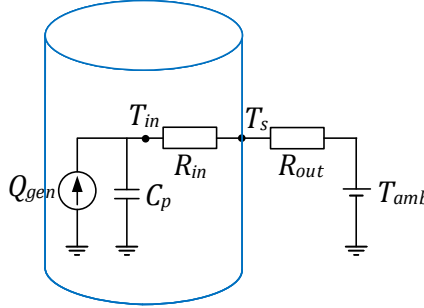
Figure 1.3: Simplified lumped model. Adapted from [31].

1.3.3 Heat transfer

The heat transfer rate by convection, and radiation are defined as:

$$Q_{conv} = -A_{surf,c} h_{conv} \left(T_s - T_{amb}\right) \tag{1.5}$$

$$Q_{rad} = -A_{surf,c} \varepsilon \sigma \left(T_s^4 - T_{sur}^4\right), \tag{1.6}$$

where $A_{surf,c}$ is the surface area of the cell, h_{conv} is the convection heat transfer coefficient, ε is the emissivity of the cell surface, $\sigma = 5.67 \cdot 10^{-8}$ Wm^{-2}K^{-4} is the Steffan-Boltzmann constant, and T_{sur} is the surrounding temperature for radiative heat transfer.

Considering that $T_{amb} = T_{sur}$, total heat transfer rate $Q_{ht} = Q_{conv} + Q_{rad}$ can be expressed

in terms of a combined heat transfer coefficient h_{comb} as follows [34]:

$$Q_{ht} = h_{comb}A_{surf,c}\left(T_s - T_{amb}\right) \tag{1.7}$$

$$h_{comb} = h_{conv} + h_{rad} \tag{1.8}$$

$$h_{rad} = \varepsilon\sigma(T_s^2 + T_{amb}^2)(T_s + T_{amb}). \tag{1.9}$$

Then, the following expression for R_{out} in Eq. 1.4 can be written:

$$R_{out} = \frac{1}{h_{comb}A_{surf,c}}. \tag{1.10}$$

Convection coefficient h_{conv} is governed by:

$$h_{conv} = \frac{\mathrm{Nu}_D \cdot k_f}{d}, \tag{1.11}$$

where k_f is the thermal conductivity of the fluid, d is the battery diameter, and Nu_D is Nusselt number computed through Eq. 1.12, formulated by Morgan for free convection from a horizontal cylinder [34]:

$$\mathrm{Nu}_D = C_{Nu} \cdot Ra_D^n, \tag{1.12}$$

where C_{Nu} and n are constants according to the Rayleigh number Ra_D.

1.3.4 Heat generation

Bernardi et al. [35] developed the following expression to compute the heat generation inside a battery:

$$Q_{gen} = I\left(V_{OC} - V\right) - I\left(T\frac{\mathrm{d}V_{OC}}{\mathrm{d}T}\right) = I^2R_T - I\left(T\frac{\mathrm{d}V_{OC}}{\mathrm{d}T}\right), \tag{1.13}$$

where the current I is positive for discharging and negative for charging. Both open circuit potential (V_{OC}) and the total internal resistance of the battery R_T depend on the state-of-charge (SOC) and temperature of the cell. The term $I\left(V_{OC} - V\right)$ of Eq. 1.13 represents the heating due to the Joule effect (irreversible heat generation). The second term is the entropy change (reversible heat generation), attributed to electrochemical reactions [36]. Besides, phase change effect, mixing effect, and simultaneous reactions are neglected in the Bernardi's formulation.

In the present approach, the battery state-of-charge (SOC) is estimated by ampere-hour integration or Coulomb counting method [37]:

$$SOC = SOC_{t=0} - \frac{1}{C_N}\int I(t)\mathrm{d}t, \tag{1.14}$$

where $SOC_{t=0} = 1$ when the battery is fully charged, and C_N is the nominal capacity of the cell.

Regarding the total internal resistance of a cell, the most common method to determine its value is the hybrid pulse power characterization (HPPC) test [38, 39]; nonetheless, electrochemical impedance spectroscopy (EIS) can help to characterize the internal impedance of the battery, and evaluate individually all components of total resistance [40].

1.3.5 NTGK model

The NTGK model is based on dual potential MSMD framework and computes the thermal and electric field of the battery as follows [30]:

$$\frac{\partial \rho C_p T}{\partial t} - \nabla \cdot (k_c \nabla T) = \sigma_{pos} |\nabla \phi_{pos}|^2 + \sigma_{neg} |\nabla \phi_{neg}|^2 + q_{ech} \tag{1.15}$$

$$\begin{aligned} \nabla \cdot (\sigma_{pos} \nabla \phi_{pos}) &= -j \\ \nabla \cdot (\sigma_{neg} \nabla \phi_{neg}) &= j, \end{aligned} \tag{1.16}$$

where σ is the electric conductivity, ϕ is the electric potential, and subscripts *pos* and *neg* refer to positive and negative electrode, respectively.

The volumetric current transfer rate j is formulated as [41]:

$$j = \frac{C_N}{C_{ref} Vol} Y \left[U - (\phi_{pos} - \phi_{neg}) \right], \tag{1.17}$$

where Vol is the volume of active zone, C_{ref} is the capacity of the battery used to obtain the parameters of the functions U and Y, which are determined by the Parameter Estimation Tool in ANSYS Fluent software by using discharging experiments. Based on the Depth-of-discharge (DoD), these functions are computed as follows [41]:

$$\begin{aligned} U &= \left(\sum_{n=0}^{5} a_n (DoD)^n \right) - C_2 (T - T_{ref}) \\ Y &= \left(\sum_{n=0}^{5} b_n (DoD)^n \right) \exp\left[-C_1 \left(\frac{1}{T} - \frac{1}{T_{ref}} \right) \right], \end{aligned} \tag{1.18}$$

where C_1 and C_2 are constants for a specific battery, and T_{ref} is the reference temperature (in Kelvin units).

The heat due to electrochemical reactions q_{ech} is written as [30]:

$$q_{ech} = j \left[U - (\phi_{pos} - \phi_{neg}) - T \frac{dU}{dT} \right], \tag{1.19}$$

where the first term represents the overpotential heat, and the second term is the entropic component.

1.4 Thermal runaway

When a Li-ion battery undergoes abuse conditions, a chain of exothermic reactions happens swiftly ending up with the cell damage. This phenomenon is named Thermal runaway (TR). Abuse conditions can be provoked by many factors such as mechanical abuse (penetration,

crush, immersion, drop, rollover, etc.), electrochemical abuse (overdischarge, overcharge, short-circuit, etc.), and thermal abuse (thermal shock, fire, overheat, etc.) [42]. During TR, it may occur explosions, emission of smoke, gasses and fire if heat is not properly dissipated [3]. The temperature of TR onset varies depending upon the type of battery chemistry (see Table 1.1). Nonetheless, this temperature is also affected by State-of-charge (SOC), electrode materials of electrodes, separator and electrolyte [42]. Melcher et al. [43] describe the beginning of TR through a parameter called *thermal runaway time* and proposed 10^2 K/s as a threshold.

A chain reaction scheme of TR for an NMC Li-ion battery with PE-based ceramic coated separator is showed in Figure 1.4. After abuse conditions occur, temperature continuously rises. The first damage is the SEI layer decomposition at 90-120 °C. Next, a reaction between intercalated lithium and the electrolyte occurs when the temperature is greater than 120 °C. Then, the PE-base separator melts followed by the cathode decomposition. Next, at more elevated temperatures ($> 200°C$), the electrolyte reaction decomposition occurs. When the ceramic cover of the separator melts, it produces short circuits and finally, the battery undergoes TR, and even combustion of the electrolyte may happen [44, 45]. TR onset may take a few seconds or many hours depending on initial and boundary conditions such as temperature of the cell, ambient temperature, heat transfer coefficient, fraction of lithium and electrolyte in the battery, etc.
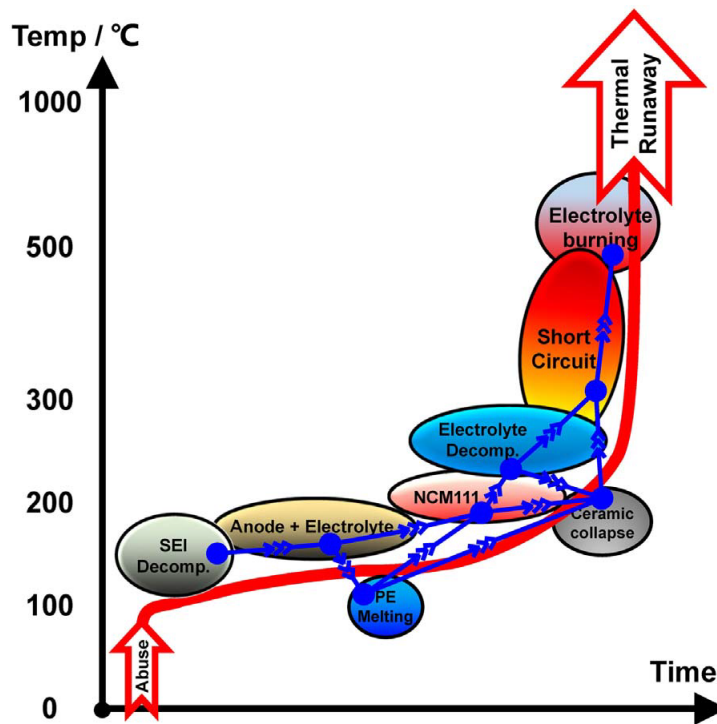
Figure 1.4: Thermal runaway chain reaction [44].

Many studies have been carried out in order to study TR. Most of them are based on a modeling based on thermal abuse. For instance, Xu et al. [46] showed that TR propagation in a battery pack could be prevented by employing a minichannel with water as a coolant. Hoffman et al. [47] reported that reducing pressure (e.g., by using a vacuum pump) lead to

prevent TR. Moreover, phase change materials (PCM) have been used to absorb the heat generated by batteries (without transfer the heat away) [23, 48]. Coman et al. [49] used a thermal lumped model combined with FEM to analyze TR induced by an internal short circuit. Venting effects during TR were studied in another work with a lumped model approach [50]. Qi et al. [51] modeled a battery pack under overcharge by coupling an electrochemical model with a thermal abuse model. Lopez at. al [52] experimentally studied the propagation of TR in a battery module. In many cases, the test procedure has been performed by employing high-quality equipment such as ARC [53, 54, 55], DSC [56] or a heatable reactor [57].

Table 1.2 presents a summary of the tests carried out in order to simulate abuse conditions for LIBs. This study is focused on thermal abuse model frequently experimented by oven test.

Table 1.2: Abuse test methods [58].

Type	Abuse Test	Description	Level*
Mechanical	Mechanical shock	Device under test is exposed to shock forces, through a sudden acceleration.	CMPV
	Drop	When a battery accidentally drops.	CP
	Penetration	Penetration of a sharp nail induces a short circuit.	CMP
	Immersion	Simulates when a battery is submerged or partially flooded.	MP
	Crush/crash	Battery is undergone to compression or until a brusque voltage drop is evidenced.	CMPV
	Rollover	Battery pack or module rotates 360°, simulating a overturn.	MP
	Vibration	It evaluates the impact of long-term vibration profiles.	CMP
Electrical	External short circuit	A low resistance element is connected through the cell terminals.	CMP
	Internal short circuit	It includes: evaluation of shutdown separator at elevated temperatures, forced internal shortcircuit caused by insertion of a nickel particle, a deformation of outer electrode layers caused by a blunt rod.	C
	Overcharge/overdischarge	To charge or discharge the battery beyond of its nominal values setting up a predefined SOC.	CMPV
Environmental	Thermal stability	The temperature of the cell is continuously increased until elevated values, even thermal runaway could occur.	CMP
	Oven test	Battery is placed in an oven at elevated temperature, e.g. 150°C [45].	C
	Thermal shock and cycling	Cells are exposed to two limits of temperature (heat and cold) during a certain period of time .	CMP
	Overheat	It evaluates the protections or control failures which produce internal overheating of the battery.	CMPV
	Extreme cold temperature	Performance of the cell at low temperatures.	CMP
	Fire	The battery is exposed to fire.	CMPV
Chemical	Emissions	Hazardous substances have to be at a certain limits trying to avoid toxic gases release.	CMP
	Flammability	To determine the flammability of battery components	CMP

Level* is denoted as C: Cell, M: Module, P: Pack, and V: Vehicle.

Theoretical analyses of TR are scarce. Wang et al. [59] presented an initial study based on a catastrophe analysis and showed that TR during the discharge process corresponds to a swallowtail catastrophe. Shah et al. [60] proposed a non-dimensional parameter named Thermal Runaway Number, that evaluate whether TR will occur or not based on a mathematical model of the heat dissipation. Feng and Zhang [61] proposed a symmetry breaking study for parallel-connected batteries including a stability criterion based on an electrical circuit

model. Smyshlyaev et al. [62] characterized the thermal dynamics in a battery pack with cooling pipes via 2D PDEs as a simplification of the CFD model. Parhizi et al. [63] presented an analytical model based on heat transfer conduction to predict the core temperature of a LIB during TR.

The stability analysis of a system could be represented from a geometric point of view by using a phase portrait. Figure 1.5 depicts an example of a phase portrait for a one-dimensional or first order system given by $\dot{x} = \sin x$. Points at $\dot{x} = 0$ are known as fixed points. Solid black dots are stable fixed points while open circles are unstable fixed points [64].
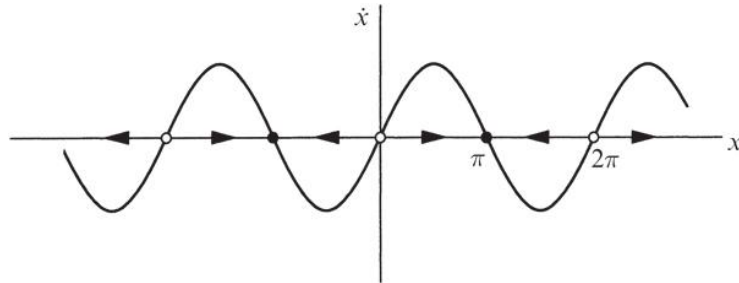
Figure 1.5: Phase portrait of the function $\dot{x} = \sin x$ [64].

1.5 Electrochemical impedance spectroscopy (EIS)

EIS is a non-destructive method based on frequency analysis that characterizes the internal impedance of battery cells at a given SOC value. A small amplitude signal, either voltage (potentiostatic) or current (galvanostatic) is applied to the battery during the test trying to minimize disturbances on the actual battery SOC. Then, the collected data allow to identify a model for the battery, capturing the electrical dynamic response in terms of an equivalent circuit model (ECM) such as a lumped-parameter Thévenin Equivalent Circuit [65].

Results of EIS test are normally presented through a Nyquist plot as shown in Figure 1.6. Pure ohmic resistance R_o is the value at the interception of the curve and the horizontal axis. The real part of the impedance at local minimum point A corresponds to the total resistance quantified from methods such as HPPC test [40, 66]. Hence, the total internal resistance of the battery is considered as the sum of ohmic resistance and charge transfer resistance R_{CT}.
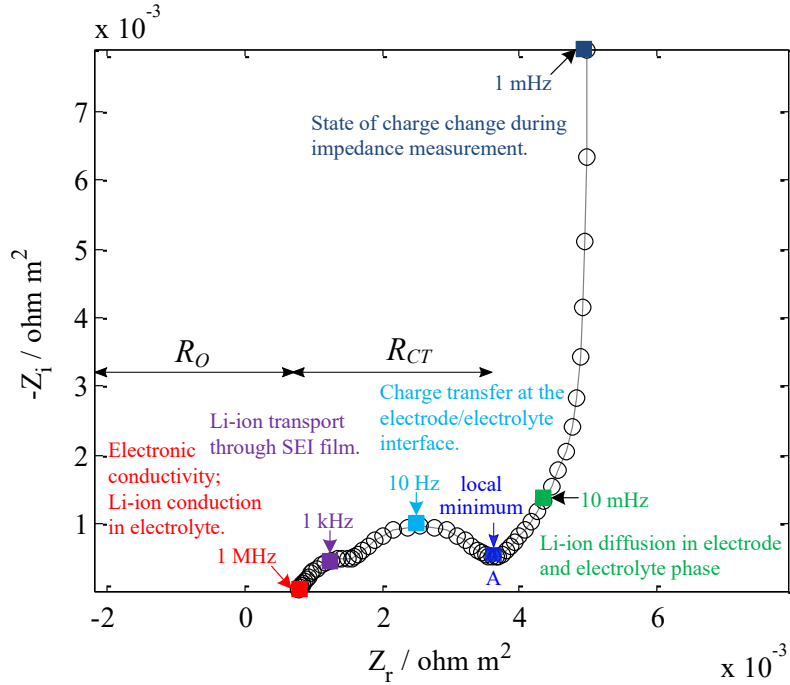
Figure 1.6: Nyquist plot scheme for an electrochemical impedance spectroscopy (EIS) experiment. Adapted from Reference [67].

1.5.1 Equivalent circuit models

An ECM describes the input/output behavior of a battery. Frequently, either an ideal voltage source or a capacitor denotes the open circuit voltage (OCV), while the other elements of the circuit include the ohmic resistance of the battery R_0 and dynamic effects [68]. The dynamical performance of the battery depends on internal parameters such as SOC, State-of-health (SOH), alternating and direct current resistance, design parameters, and external factors (temperature, direct current, short-term history, and long-term history) [69]. Figure 1.7 displays distinct ECMs where V_L is the terminal voltage of the battery and I_L is the load current. These models are computed by applying basic electric calculations. Each parameter of the circuit is generally estimated via regression analysis. An adequate ECM can even describe the battery electrochemical principles [70].
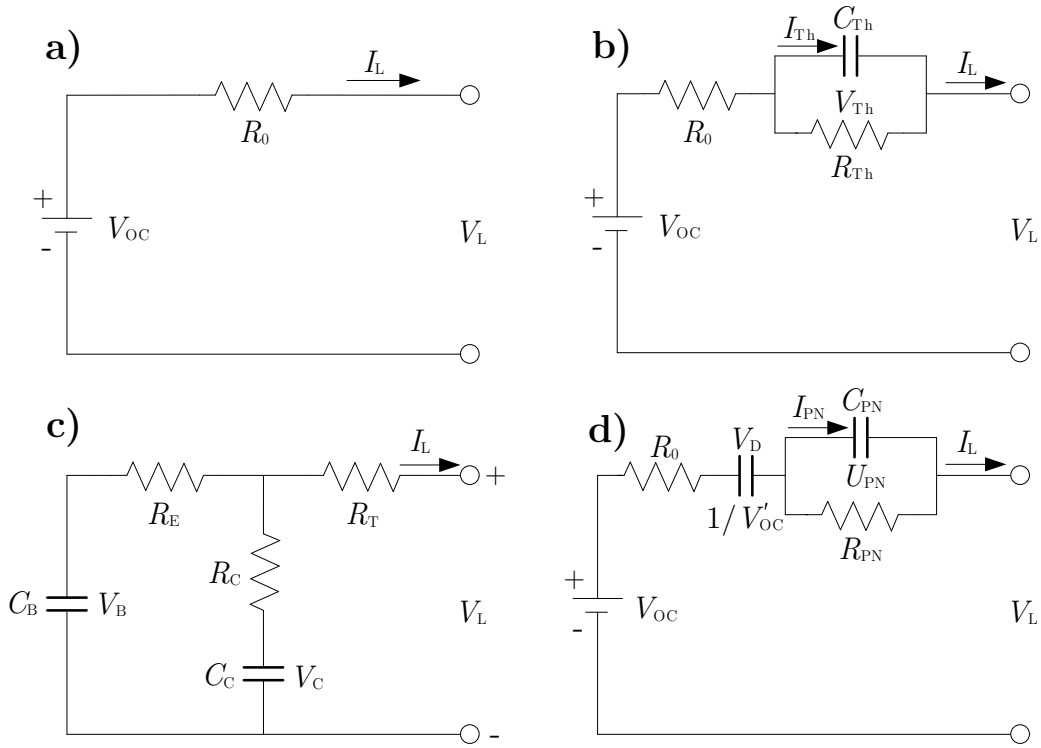
Figure 1.7: Equivalent circuit models. (**a**) Rint model, (**b**) Thevenin model, (**c**) RC model, (**d**) PNGV model. Adapted from [71, 68]

.

1.6 State estimation

The state estimation is widely applied in many fields of engineering. State-space models can be classified into linear models and nonlinear models. Mathematical tools are more accessible for linear systems. Nevertheless, states estimation for nonlinear models can be accomplished by using estimators based on Kalman filter and Particle filter (PF). These filters are capable of online monitoring for state estimation. In [37], A dual Kalman filter, a combination of a Kalman filter and an extended Kalman filter, was implemented to estimate the temperature inside the battery and convection coefficient. An adaptive temperature estimation method based on dual extended Kalman filtering and was developed in [72] considering variable ambient temperature. In [73], a thermal model coupled with electrical impedance measurement was presented, the battery core and surface temperature were indirectly estimated by using an extended Kalman filter based on a polynomial approximation of the temperature. The aforementioned works were developed for a single cell. A Foster network thermal model for a battery module considerably reduces the simulation time comparing to conventional CFD [6], but this model can not be implemented for online monitoring. In [74], the core temperature for a battery module was estimated by a Kalman Filter approach using surface temperature measurements. Tian et al. [7] reconstructed the temperature field for a battery module using an estimator based on Kalman filter. Another powerful tool to face state estimation is PF. This approach is widely used to estimate SOC and SOH of cells, but in the present work it is employed to estimate the surface cell temperature for a battery module.

PF or sequential Monte Carlo approach is a technique for implementing a method to estimate hidden process states (i.e., when a state can not be directly measured by sensors) in real-time by combining the power of Monte Carlo methods with the Bayesian inference [75]. In PF approach, difference equations are utilized to model a non-linear system, and measurements are given at discrete times. PF is based on two steps: prediction and update. At the prediction stage, the probability density function (PDF) is recursively predicted from a measurement time to the next one. During the update, the latest measurement is used to adjust the prediction PDF. This is executed through the Bayes theorem, which is the technique to update knowledge about the target state considering extra information from new data [76].

1.6.1 Bayesian estimation

In order to define the Bayesian estimation problem, a discrete-time model (process model) is considered by using Eq. 1.20 that describes the evolution of the state vector $\mathbf{x} \in \mathbb{R}^{n_x}$:

$$\mathbf{x_k} = \boldsymbol{f_k}\left(x_{k-1}, \omega_{k-1}\right), \tag{1.20}$$

where $k \in \mathbb{N}$ is the time instant, and $\boldsymbol{f}$ is generally a nonlinear function that depends on both the state vector $\mathbf{x}$ and the noise process vector $\omega \in \mathbb{R}^{n_\omega}$ iid (independent and identically distributed).

Moreover, it is also considered a measurement vector $\mathbf{z} \in \mathbb{R}^{n_z}$ that is linked to the state vector $\mathbf{x}$ and a noise measurement vector $\nu \in \mathbb{R}^{n_\nu}$ iid, through a possibly nonlinear function $\boldsymbol{h}$ according to Eq. 1.21:

$$\mathbf{z_k} = \boldsymbol{h_k}\left(x_k, \nu_k\right), \tag{1.21}$$

The goal of the state estimation problem is to know $\mathbf{x_k}$ based on both the state evolution model (Eq. 1.20) and the measurements $\mathbf{z_{1:k}} = \{\mathbf{z_i}, i = 1, ..., k\}$ given by the measuring model (or observation model) defined through Ec. 1.21. Thereby, the PDF $p\left(\mathbf{x_k} \mid \mathbf{z_{1:k}}\right)$ is required. It is assumed that the initial PDF of the state vector (*a priori* PDF) $p\left(\mathbf{x_0} \mid \mathbf{z_0}\right) = p\left(\mathbf{x_0}\right)$ is available. Then, the PDF $p\left(\mathbf{x_k} \mid \mathbf{z_{1:k}}\right)$ can be recursively obtained taken into account two stages: prediction and update.

Assuming that the PDF $p\left(\mathbf{x_{k-1}} \mid \mathbf{z_{1:k-1}}\right)$ at the time $k-1$ is available, the prediction stage uses the process model to obtain the *a priori* PDF at the time k by using the Chapman-Kolmogorov equation [76]:

$$p\left(\mathbf{x_k} \mid \mathbf{z_{1:k-1}}\right) = \int p\left(\mathbf{x_k} \mid \mathbf{x_{1:k-1}}\right) p\left(\mathbf{x_{k-1}} \mid \mathbf{z_{1:k-1}}\right) \mathrm{d}\mathbf{x_{k-1}} \tag{1.22}$$

For the update stage, the measurement $\mathbf{z_k}$ available at the time k is employed to update the PDF *a priori* using the Bayes' theorem:

$$p\left(\mathbf{x_k} \mid \mathbf{z_{1:k}}\right) = \frac{p\left(\mathbf{z_k} \mid \mathbf{x_k}\right) p\left(\mathbf{x_k} \mid \mathbf{z_{1:k-1}}\right)}{p\left(\mathbf{z_k} \mid \mathbf{z_{1:k-1}}\right)}, \tag{1.23}$$

where the normalizing constant (Eq. 1.24) depends on the likelihood function $p\left(\mathbf{z_k} \mid \mathbf{x_k}\right)$ defined by Eq. 1.21.

$$p\left(\mathbf{z_k} \mid \mathbf{z_{1:k-1}}\right) = \int p\left(\mathbf{z_k} \mid \mathbf{x_k}\right) p\left(\mathbf{x_k} \mid \mathbf{z_{1:k-1}}\right) \mathrm{d}\mathbf{x_k} \tag{1.24}$$

At the update stage, the measurement $\mathbf{z_k}$ is employed to modify the *a priori* PDF to obtain the *a posteriori* PDF of the current state vector.

1.6.2 Particle filter

The particle filter (PF) approximates the optimal Bayesian solution when it is very hard to find an analytical solution. The PF is a recursive Bayesian filter implemented by Monte Carlo simulations. The main idea is to represent the required *a posteriori* PDF through the use of random samples with their respective weights and to calculate estimates based on these samples and weights [76].

PF is based in the sequential importance sampling (SIS) algorithm. To build the PF algorithm, first, the particles $\left\{\mathbf{x}_k^i, i = 1, ..., N_s\right\}$ with the associated weights $\left\{\mathbf{w}_k^i, i = 1, ..., N_s\right\}$ are considered, where N_s is the number of particles and $\mathbf{x}_k$ is the state vector at time k. Then, the weights are normalized by $\sum_{i=1}^{N_s} \mathbf{w}_k^i = 1$. The weights are chosen according to the principle of *importance sampling*. Therefore, the *a posteriori* PDF at the time k can be approximated through Eq. 1.25, where $\delta(\cdot)$ is the delta Dirac function [76]:

$$p\left(\mathbf{x_k} \mid \mathbf{z_{1:k}}\right) \approx \sum_{i=1}^{N_s} \mathbf{w}_k^i \delta\left(\mathbf{x_k} - \mathbf{x_k^i}\right), \tag{1.25}$$

The update for the weights is written as:

$$\mathbf{w}_k^i = \mathbf{w}_{k-1}^i \frac{p\left(\mathbf{z_k} \mid \mathbf{x_k^i}\right) p\left(\mathbf{x_k^i} \mid \mathbf{x_{k-1}^i}\right)}{q\left(\mathbf{x_k^i} \mid \mathbf{x_{0:k-1}^i}, \mathbf{z_{1:k}}\right)}, \tag{1.26}$$

where $p\left(\mathbf{z_k} \mid \mathbf{x_k^i}\right)$ is the likelihood and $q(\cdot)$ is named an *importance density* that generates the samples N_s. It can be observed that as $N_s \to \infty$, the approximation given by Eq. 1.25 converges to the true posterior PDF $p\left(\mathbf{x_k} \mid \mathbf{z_{1:k}}\right)$. A graphical illustration about PF is depicted in Figure 1.8.

1.6.3 Artificial evolution of parameters

Models generally consider time invariant and unknown parameters. Nevertheless, when these parameters are time variant, it can harm the process of PF estimation. To address this problem, the concept of artificial evolution can be applied [77]. This methodology is based on extending the dimension of the state vector, implementing the parameter as an additional state which is modeled like a random walk with small variance [78]. Then, the extended model process utilized by the PF is written as:

$$\mathbf{x_k} = \boldsymbol{f_k}\left(x_{k-1}, \theta_{k-1}, \omega_{k-1}\right), \tag{1.27a}$$
$$\theta_k = \theta_{k-1} + \eta_{k-1}. \tag{1.27b}$$
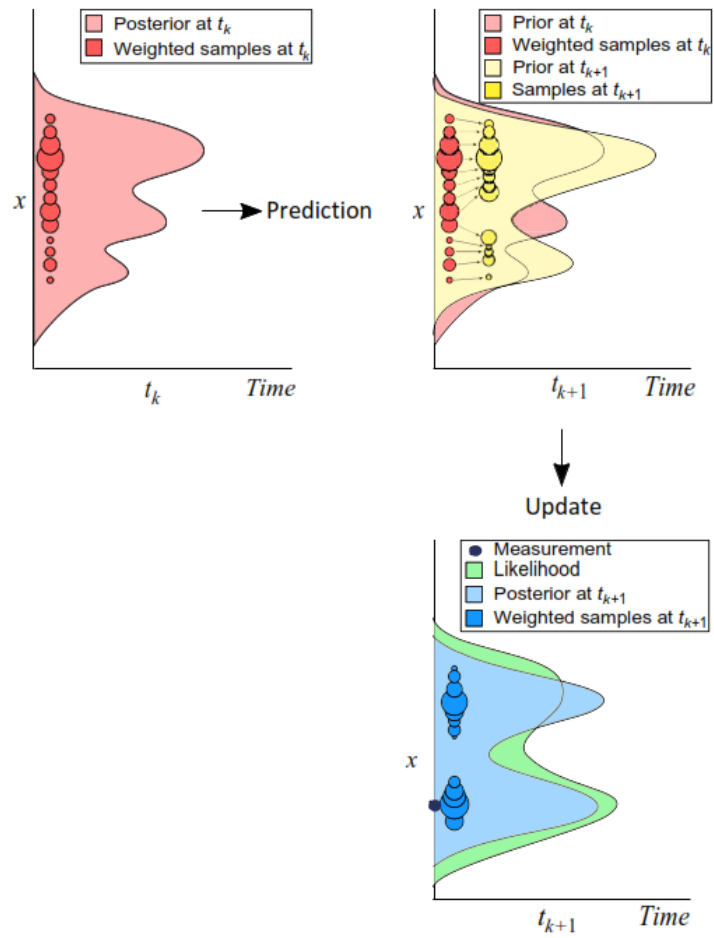
Figure 1.8: Posterior estimation PDF of a state using particle filter. Adapted from [79].

Chapter 2

Methodology

This chapter presents the methodology to study the thermal behavior of a single cell and a battery pack. The approaches to study the state estimation based on particle filtering, and thermal runaway are also presented.

2.1 Methodology for thermal modeling of a single cell

Some geometry considerations are necessary to take into account depending on the model applied. The lumped model solves the cell surface temperature which is considered uniformly distributed. The battery geometry employed to solve the 3D-CFD model is a solid cylinder 65 mm length and 26 mm diameter. The cell geometry for the NTGK model has three components: anode (negative tab), cathode (positive tab), and jelly-roll, as shown in Figure 2.1a. A detail of the jelly-roll is provided in Figure 2.3b. Thermal resistance through the shell is considered negligible, then it is not modeled. Also, the thermal effect due to battery holder is not studied.

| (a) | (b) |
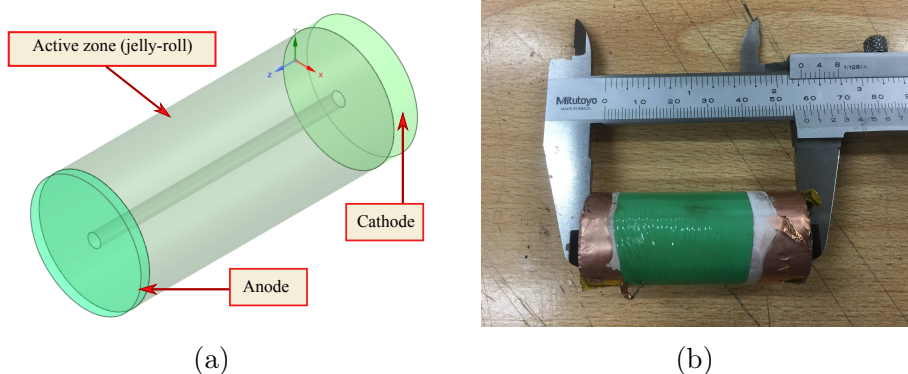
Figure 2.1: Battery details for NTGK model: (**a**) Cell geometry. (**b**) Jelly-roll of the LCO 26650 cell.

Figure 2.2 depicts the general procedure to develop the present study. The first step is to obtain the heat generation rate of the battery by estimating the internal resistance

R_T using EIS, and the entropic coefficient applying the potentiometric method. Next stage is to estimate heat capacity and internal thermal resistance of the cell R_{in} via parameter identification. The following step is to perform battery discharging tests while ambient temperature, cell surface temperature, and heat flux from the LIB are recorded. Discharging tests allow to obtain U and Y functions using parameter estimation tool in Fluent. Finally, the models are numerically solved using MATLAB for lumped model, and ANSYS Fluent 19.2 based on finite volume method, for both 3D-CFD and NTGK models.
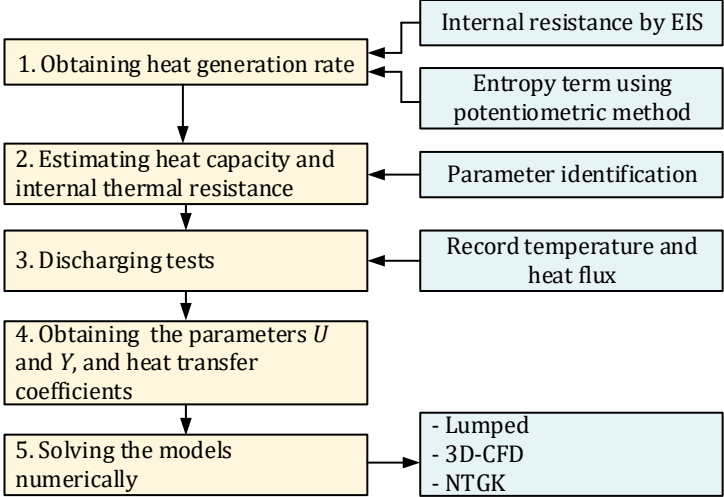
Figure 2.2: Methodology scheme.

2.1.1   Experimental set-up

An ICR 26650 battery (see specifications in Table 2.1) was fully charged following the constant-current constant-voltage (CC-CV) protocol using a battery charger (iCharger 208B). The first stage (constant-current) was at 2 A, then the iCharger switches to the constant voltage phase. Subsequently, the battery was discharged using a BK Precision 8500 programmable DC load (Figure 2.3a). Current rates applied were 2 A (0.5C), 4 A (1C), 6 A (1.5C), and also a variable current profile. This last profile was obtained by ADVISOR software selecting a highway HWFET-driving cycle as velocity input for an electric vehicle. The simulated current was scaled at a maximum of 5.5 A, as shown in Figure 2.4, and this cycle was repeatedly applied to the cell until the energy extracted was 4 Ah. Regeneration current was not considered.

Table 2.1: Battery specifications.

Property	Value
Diameter	26 mm
Height	65 mm
Mass (measured)	0.088 kg
Cathode material	$LiCoO_2$
Anode material	Graphite
Nominal capacity	4 Ah
Tested capacity	4.3 Ah
Nominal voltage	3.7 V
Cut off voltage	2.75 V
Charge limit voltage	4.2 V
Maximum charge current	1 C
Maximum discharge current	2 C
Emissivity [50]	0.8
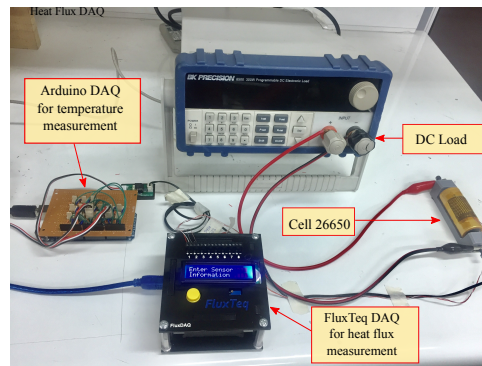
(a)   (b)
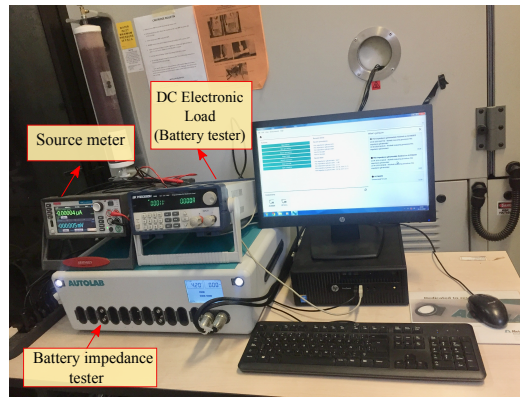
(c)   (d)

Figure 2.3: Experimental set-up. (**a**) Set-up for a discharging test. (**b**) Detail of the heat flux sensor. (**c**) Thermal chamber. (**d**) Equipment for EIS test.
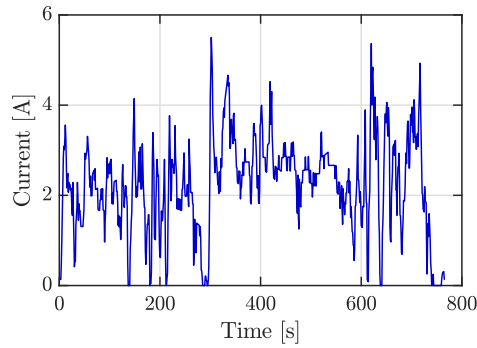
Figure 2.4: Scaled current profile of a HWFET-driving cycle.

All discharging tests were repeated five times to ensure repeatability measurements. Ambient temperature and cell temperature were recorded through a negative temperature coefficient (NTC) thermistor (ZX-Thermometer) connected to an Arduino processor board. This sensor operates between $-20\,°C$ and $85\,°C$ with an uncertainty of $\pm\ 0.5\,°C$. It requires a direct-current supply voltage between $+1.8$ V and $+5.0$ V. A code was developed using MATLAB software to convert voltage input (from Arduino board) into temperature. Since ambient temperature fluctuations were less than $1\,°C$ during all tests, this value was assumed to be constant. Heat flux from the cell was measured by a PHFS-01 FluxTeq heat flux sensor (Figure 2.3b) connected to a FluxTeq DAQ (see Figure 2.3a). Measurements of heat flux are plotted in Figure 2.5.
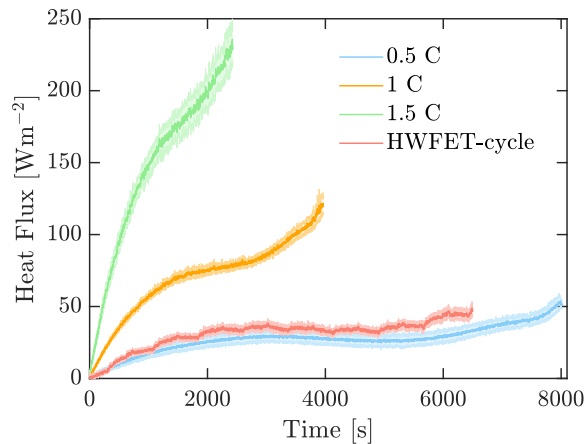
Figure 2.5: Measured heat flux at different discharging rates.

2.1.2   Heat generation estimation

Heat generation in the cell was computed from Eq. 1.13 that includes internal resistance and entropy change.

Experiment to characterize the battery internal resistance

Electrochemical impedance spectroscopy (EIS) was carried out to estimate the internal resistance of the battery. First, the fully charged battery was placed in a thermal chamber

23

EZT-570i (see Figure 2.3c) at 15 °C. After 2 hours of rest, galvanostatic EIS was conducted by using an impedance tester equipment PGSTAT302N (see Figure 2.3d). Details of the setup are listed in Table 2.2. This process was repeated at 25 °C, 35 °C, and 45 °C. After performing the experiment at 45 °C, the battery was discharged at 90 % SOC and overnighted. The whole process was repeated until the cell was completely discharged (0 % SOC), decreasing the battery SOC in intervals of 10 % between each of the EIS tests.

Table 2.2: Parameters for the EIS experiment.

Parameter	Description
First applied frequency	10^4 Hz
Last applied frequency	0.005 Hz
Number of frequencies	10 per decade
Frequency step type	Points per decade
Amplitude	0.05 A
Wave type	Sine

Figure 2.6 shows results of EIS experiments at 100% SOC represented by a Nyquist plot. This plot depicts how the internal impedance of the LCO battery varies at different temperatures and according to the frequencies applied (see Figure 1.6). Internal impedance at 100% SOC is the only value that it is possible to know for sure, the rest of values at another SOC are estimations. It can be observed that as temperature increases, radius of semicircles associated to real component of impedance (resistance) decreases, i.e., internal resistance of cell decreases as well.
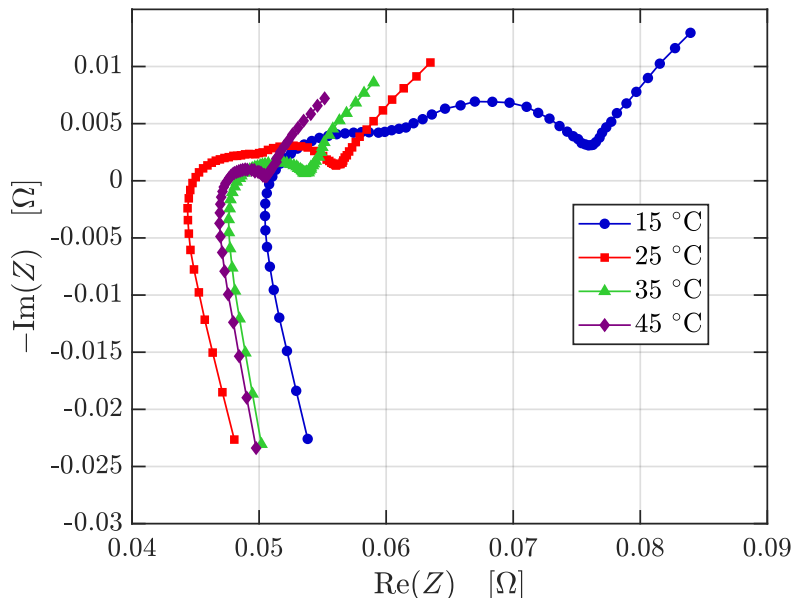
Figure 2.6: Nyquist plot for the LCO battery at 100% SOC.

The experimental characterization of the battery internal resistance at different temperatures based on EIS tests is depicted in Figure 2.7. It reveals that at a lower temperature,

and near to 0 % of SOC, the cell resistance increases. At 35 °C and 45 °C, the resistance has practically the same value.
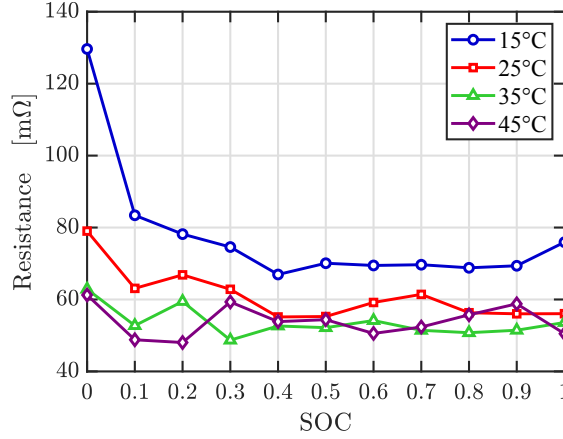
Figure 2.7: Battery internal resistance.

Average battery resistance for each discharging rate test is detailed in Table 2.3. Each value represents R_T in Eq. 1.13, i.e., it allows to compute the irreversible heating. It is evident that at lower discharge rates, the resistance increases. The reason is mainly due to the fact that at lower discharge rates, the cell temperature decreases while the resistance increases as shown in Figure 2.7.

Table 2.3: Average cell resistance.

Current	Resistance (mΩ)	Ambient temperature (°C)
0.5C	57.7	24
1C	55.3	24
1.5C	53.9	23
HWFET-cycle	56.8	25

Entropy coefficient experiment

Entropy change term is expressed as a relationship between Open circuit voltage and cell temperature, and was obtained by applying the potentiometric method: the battery 100 % charged was put into a thermal chamber at 15 °C. After it rested for two hours to reach thermal equilibrium [36], and the voltage was measured by using a KEITHLEY 2460 sourcemeter. In order to obtain the relationship dV_{OC}/dT, the same process was performed progressively at 25, 35, and 45 °C, respectively. Next, the cell was discharged at 90 % SOC and overnighted. The whole test described before was repeated with intervals of 10 % of SOC until the charge of the battery drops to 0 % of SOC [80].

Experimental values for the entropy term are presented in Figure 2.8. There does not exist a significant variation of entropy change at the different temperatures. In the interval

of 20 % to 80 %, the entropy change is positive with a maximum value near to 0.2 mV/K. A similar entropy profile was reported by Zhang et al. [81].
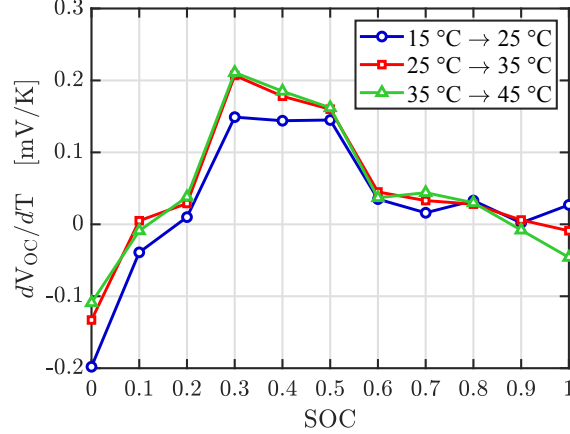
Figure 2.8: Battery entropy change coefficient.

2.1.3 Heat capacity and internal thermal resistance

To estimate heat capacity and internal thermal resistance, a consecutive current pulse of 0.4 A, 2 A, 4 A, and 3 A, each one of them with a duration of 10 s, was continuously applied until the battery was discharged. Ambient and battery temperatures, and heat flux were recorded as depicted in Figure 2.9a, and Figure 2.9b, respectively. These measurements allow to compute h_{comb} by least squares regression from Eq. 1.7, and then, R_{out} from Eq. 1.10. After obtaining h_{comb}, it is possible to figure out an experimental h_{conv} from Eq. 1.8.

Following a similar procedure proposed by Bryden et al. [32], the next stage was to estimate C_p and R_{in} from Eq. 1.4 by fitting the *initial section* of the measured cell temperature (see Figure 2.9a), where the temperature gradient is greater. This region was taken for the first 2700 seconds. Fitted temperature for parameter estimation is shown in Figure 2.9c. Parameters obtained are given in Table 2.4. Then, specific heat is obtained by $c_p = m^{-1} C_p = 1197$ Jkg^{-1}K^{-1}. The aforementioned authors reported values of $R_{in} = 1.4$ KW^{-1} and $c_p = 1169$ Jkg^{-1}K^{-1} for a 26650 LFP battery.

Table 2.4: Thermal parameters obtained.

R_{out} (KW^{-1})	R_{in} (KW^{-1})	C_p (JK^{-1})
15.8 ± 2.7	1.8 ± 0.4	105.3 ± 3.8
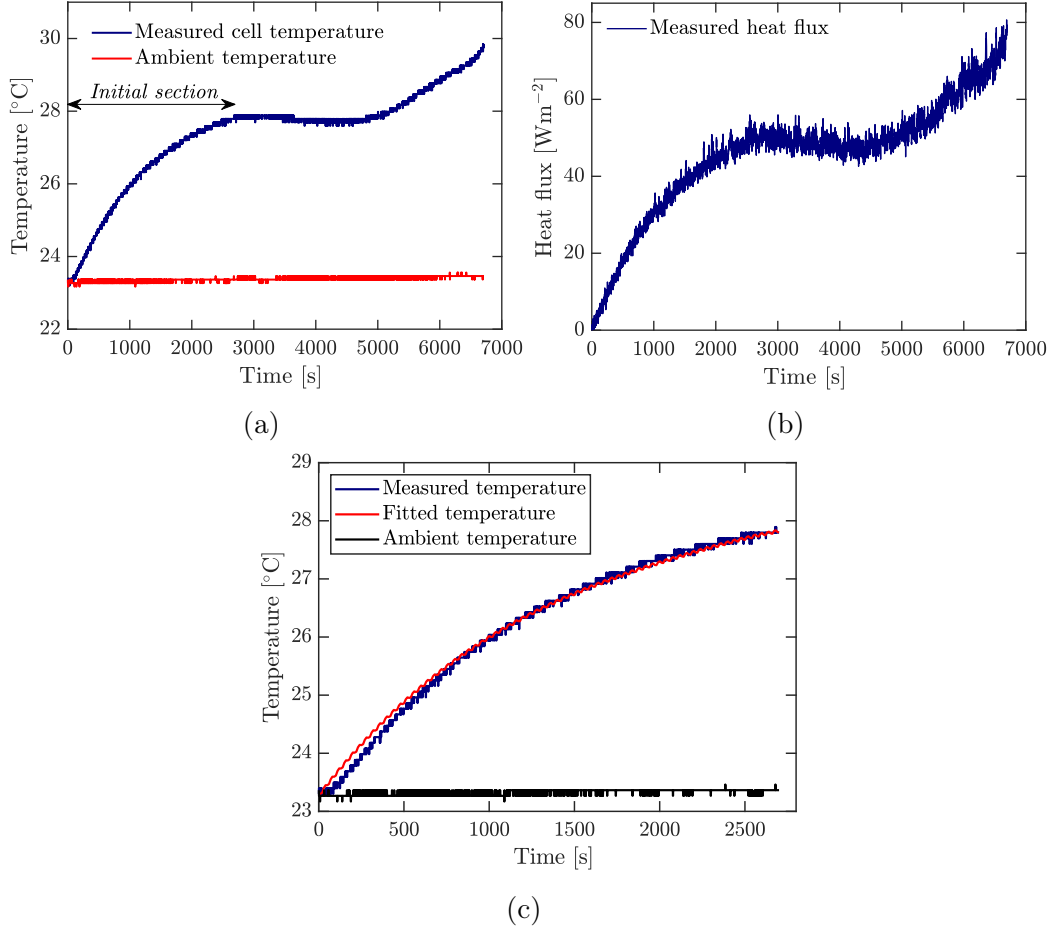
Figure 2.9: Measurements and temperature fitting under applying a current pulse of 0.4 A, 2 A, 4 A, and 3 A: (**a**) Battery surface temperature and ambient temperature. (**b**) Battery heat flux. (**c**) Fitted surface temperature of cell for parameter estimation.

2.1.4 Physical properties and solving

Properties of a 26650 LCO battery detailed in Table 2.5 were used to solve the lumped and 3D-CFD models. For NTGK approach, parameters and properties are given in Table 2.6 and Table 2.7, respectively. Besides, for all three proposed models, there were utilized experimental heat transfer coefficients based on heat flux and temperature measurements of the cell surface. These coefficients are listed in Table 3.2 and were obtained following a similar procedure described in the section 2.1.3. Furthermore, it was assumed that the external radiation temperature is the same as the ambient temperature. The nominal capacity of the cell is 4 Ah; however, the average tested capacity was 4.3 Ah, and this last value was employed for thermal modeling. An experimental-based heat transfer coefficient (h_{conv}) was applied and radiation effects were considered so that the boundary condition on the cell surface is expressed as:

$$-k\frac{\partial T}{\partial n}\bigg|_{surface} = h_{conv}\left(T|_{surface} - T_{amb}\right) + \varepsilon\sigma\left(T^4|_{surface} - T_{amb}^4\right), \qquad (2.1)$$

where $\hat{n}$ is a unit normal vector.

Table 2.5: Properties of materials for lumped and 3D-CFD models.

Property	Value	Lumped	3D-CFD
Density (kgm^{-3})	2550[a]	✓	✓
Specific heat (Jkg^{-1}K^{-1})	1197 [b]	✓	✓
Thermal conductivity: radial, tangential, axial (Wm^{-1}K^{-1})	0.8, 27, 27 [82]	✗	✓
Inner thermal resistance (KW^{-1})	1.8 [b]	✓	✗

[a] Computed.   [b] Parameter estimation.

Table 2.6: Parameters for NTGK model. Obtained in Fluent using discharging tests.

	a_0	a_1	a_2	a_3	a_4	a_5
U	4.0682	-1.2669	-0.9072	3.7550	-2.3108	-0.1701
	b_0	b_1	b_2	b_3	b_4	b_5
Y	16.5066	-27.0367	237.3297	-632.603	725.0825	-309.8760

Table 2.7: Properties of materials for MSMD model.

Property	Active zone (jelly-roll)	Positive tab (aluminium)	Negative tab (steel)
Density (kgm^{-3})	2226[a]	2719	8030
Specific heat (Jkg^{-1}K^{-1})	1197[b]	871	502.48
Thermal conductivity: radial, tangential, axial (Wm^{-1}K^{-1})	0.8, 27, 27 [82]	202.4	16.27
Electric conductivity (Sm^{-1})	0	3.541·10^7	8.33·10^6

[a] Measured.   [b] Parameter estimation.

Based on the current profile applied to simulate the 3D-CFD approach, there are two considerations to couple the heat generation per unit volume to the energy equation. Firstly, for constant current rates, a User Defined Function (UDF) was utilized. Secondly, for variable currents (HWFET-cycle), a transient table was employed. In contrast, the NTGK model automatically computes the heat generation rate.

Numerically, the lumped model was solved by Runge Kutta Fourth order method, and the other two models were computed through a Semi-Implicit Method for Pressure Linked Equations (SIMPLE) scheme. For current rates of 2 A, 4 A, 6 A, and HWFET-cycle, the simulation time was 8015 s, 3964 s, 2430 s, and 6500 s, respectively. Furthermore, 1 s time step was utilized in all cases.

According to the description above, an example of boundary conditions set-up in Fluent applied to the battery walls at 1.5C-rate is shown in Figure 2.10. In case of the NTGK

model, boundary conditions of walls are also managed in the same way, but the Battery Model in Fluent have to be enabled (Figure 2.11). Initial conditions are ambient and battery temperature, which are assumed to be the same at the beginning of the discharge.
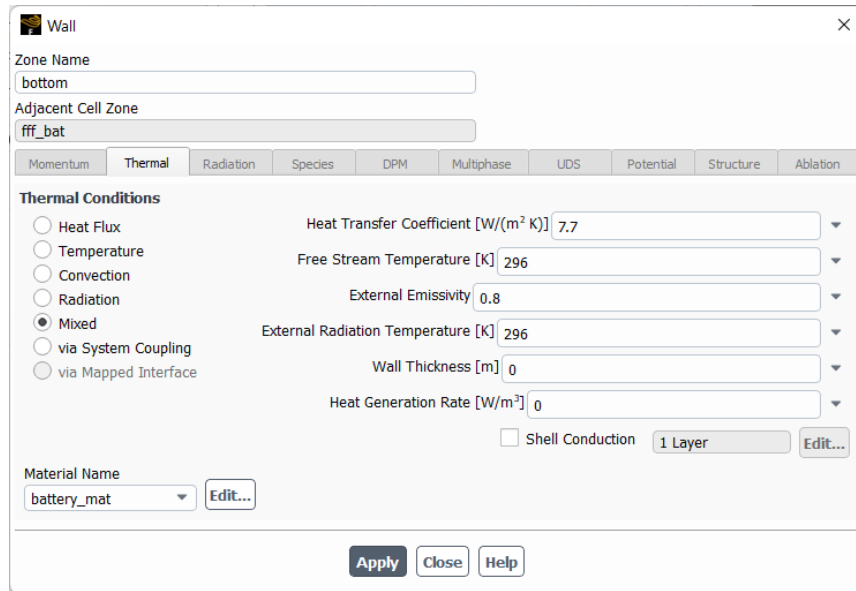
Figure 2.10: Boundary conditions set-up in Fluent for CFD-3D model at 1.5C-rate.
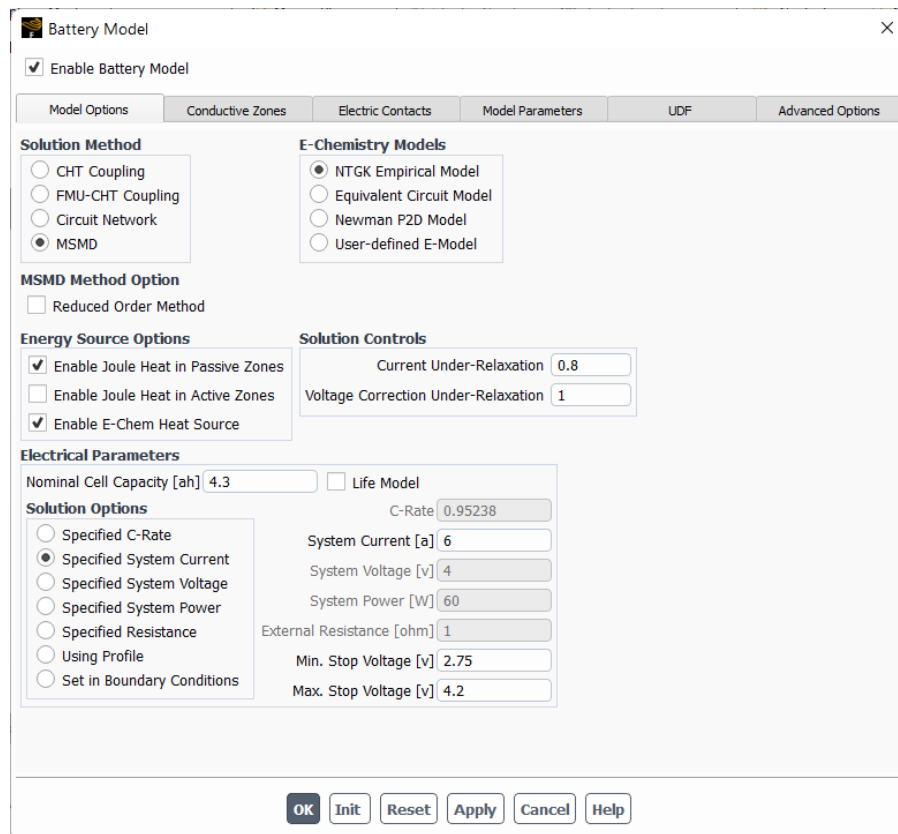
Figure 2.11: Screenshot of battery model in Fluent for NTGK approach at 1.5C-rate.

2.1.5 Battery meshing

Meshing is the operation in which a continuous geometric space of an object is divided into small elements or cells. A mesh independence study was carried out to solve the 3D-CFD (Table 2.8), and NTGK model (Table 2.9), both modeled with a discharge current of 6 A. In each case, mesh 2 was selected taking into account that maximum temperature and total heat transfer rate do not vary when the number of mesh elements is increased. Moreover, for the energy equation, the convergence criterion was satisfied once the residuals took a value around 1×10^{-7} and 1×10^{-14} for the 3D-CFD and the NTGK model, respectively. In this way, a mesh with 45604 elements was selected for 3D-CFD model, and a mesh with 38777 elements was chosen for NTGK model. Figure 2.12 shows a detail of batery meshing in Fluent.

Table 2.8: Mesh independence test for 3D-CFD model.

Description	Mesh 1	Mesh 2	Mesh 3
Number of elements	1104	45604	161124
Maximum temperature (°C)	41.30	41.42	41.43
Total heat transfer rate (W)	1.51	1.52	1.52

Table 2.9: Mesh independence test for NTGK model.

Description	Mesh 1	Mesh 2	Mesh 3
Number of elements	1812	38777	132892
Maximum temperature (°C)	39.23	39.10	39.10
Total heat transfer rate (W)	1.31	1.31	1.31

(a)

(b)
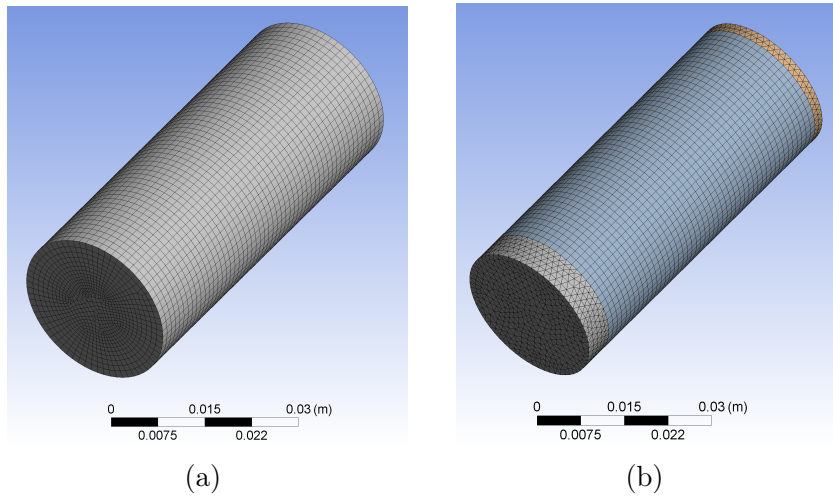
Figure 2.12: Battery meshing: (**a**) 3D-CFD model. (**b**) NTGK model.

2.2 Methodology for thermal modeling of a battery pack with air cooling

Natural and forced convection in the battery pack with fifteen cells was modeled numerically and tested experimentally.

The experimental test was performed using an arrangement of fifteen LCO cylindrical cells (type ICR 26650) represented in Figure 2.13 under natural and forced convection. Forced convection was carried out using two direct current axial fans (Ebmp-Papst 4412FNH) at two different airflow velocities (1.5 and 2.7 ms^{-1}, respectively). These values of velocity yield turbulent flow. Measurement points of air velocity are shown in Figure 2.13a. In order to obtain a developed velocity profile, it is remarkable to take into consideration that the mean velocity profile turns into fully developed about 25 to 40 diameters of the pipe from the entrance [83]. In line with this criterion, A PVC tube (0.11 m diameter, and 3 m length) conducted the air to the battery arrangement. Velocity was measured in six points into the tube according to the recommendations given by ASHRAE standard (see Figure 2.15).

Temperature sensors (NTC thermistors) were placed on the surface of each battery, and at inlet and outlet of the battery pack. Ambient room temperature was measured as well. An Arduino interface was used to acquire temperature data. Cells have been connected in series. The discharge process was performed at constant current: 0.25C, 0.5C and 1C-rate. High discharging rates are not feasible due to the chemistry of cells. For example, the LCO cell used in this study decreased its capacity from 4.3 Ah to around 3.6 Ah when a discharging current of 8 A was applied.
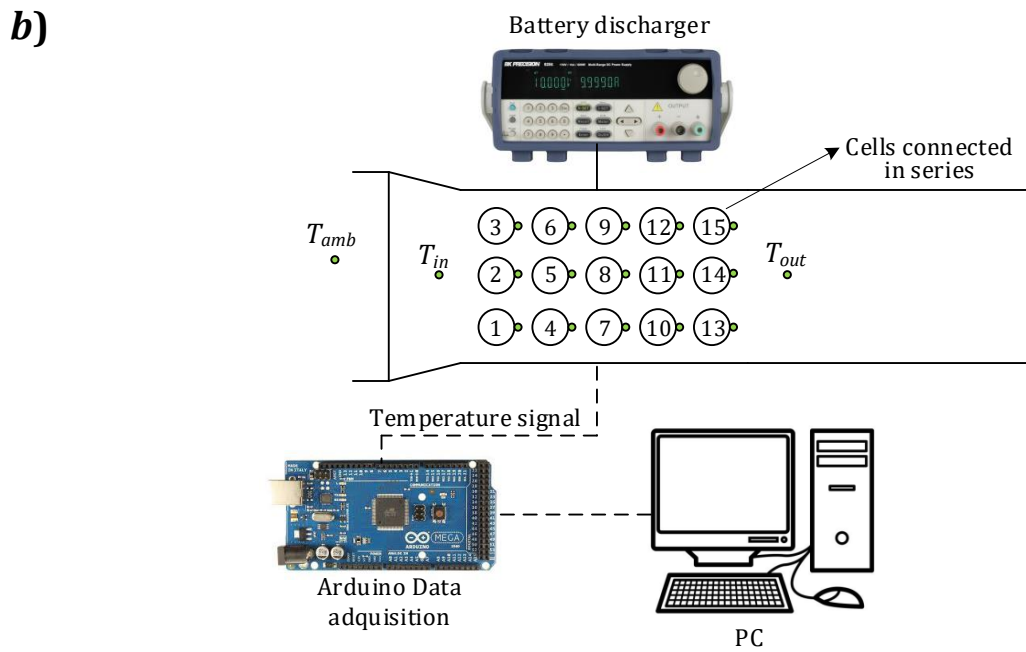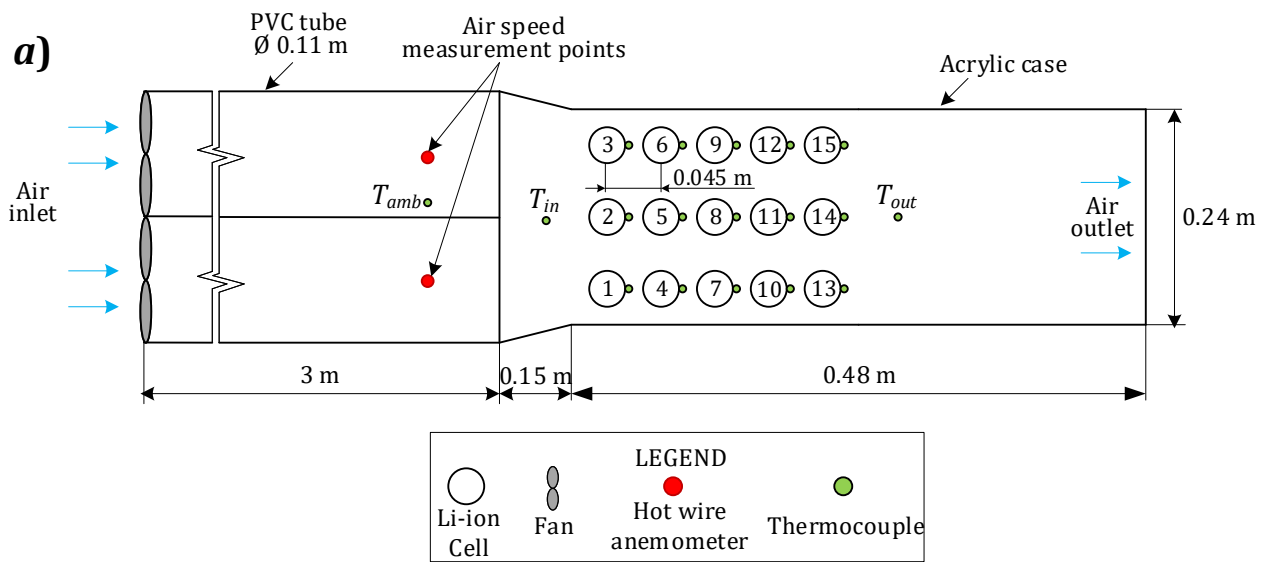
Figure 2.13: Scheme of the battery pack experiment: (**a**) Top view of the experimental layout. (**b**) Test set-up.

(a)

Electric wires
to connect batteries

Power source

Arduino DAQ

NTC Thermistor

Battery tester
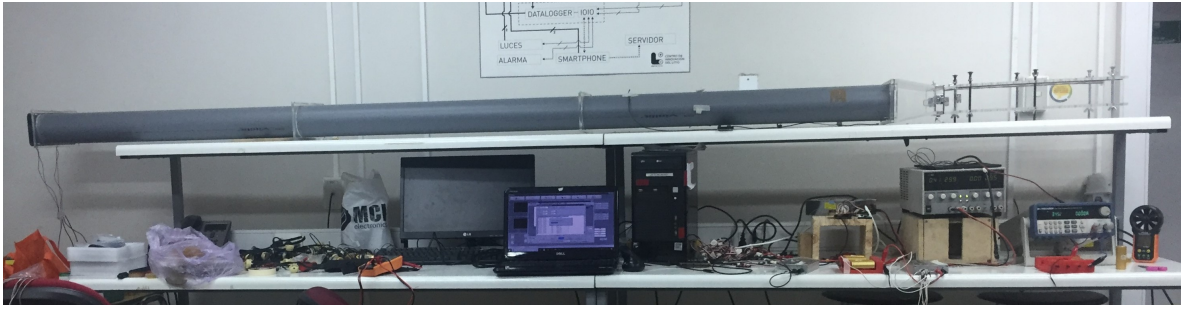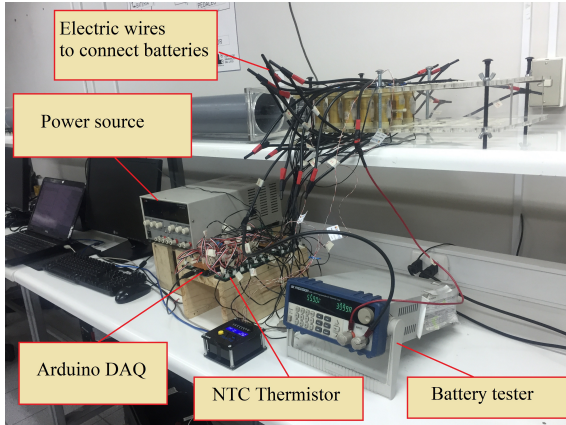
(b)
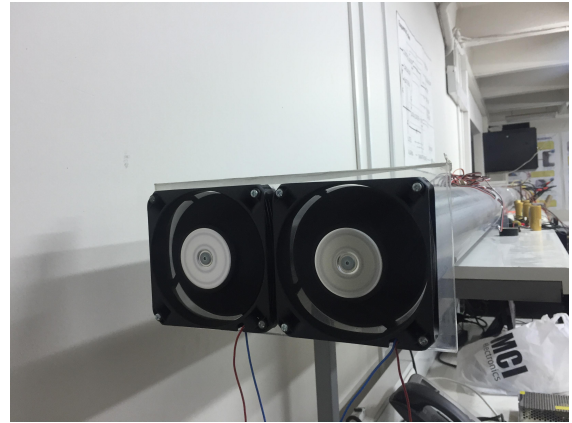
(c)

Figure 2.14: Experimental set-up. (**a**) Wind tunnel. (**b**) Detail of the battery module and testing equipment. (**c**) Fans.

$0.032D$
$0.135D$
$0.321D$
$0.679D$
$0.865D$
$0.968D$
D

No. of Measuring Points per Diameter	Position Relative to Inner Wall
6	0.032, 0.135, 0.321, 0.679, 0.865, 0.968
8	0.021, 0.117, 0.184, 0.345, 0.655, 0.816, 0.883, 0.979
10	0.019, 0.077, 0.153, 0.217, 0.361, 0.639, 0.783, 0.847, 0.923, 0.981

Log-Linear Rule for Circular Ducts
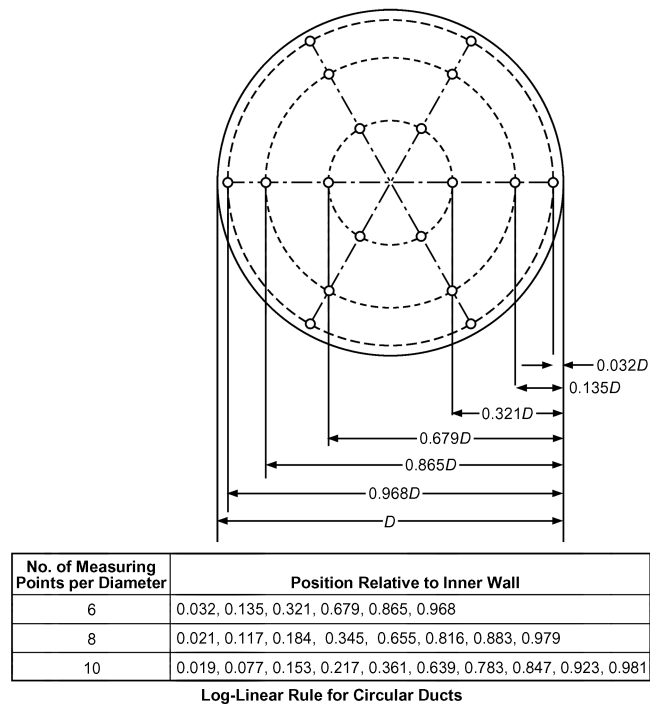
Figure 2.15: Distribution of velocity measuring points [84].

2.2.1 Materials and equipment for battery pack thermal behavior test

Materials and equipment needed for this experimental work are listed as follows:

- Test bench, provided with two fans (Ebmp-Papst 4412FNH) and two PVC tubes. Cells were placed into an acrylic case (8 mm thickness).
- 15 new Li-ion batteries type 26650 with $LiCoO_2$ chemistry.
- 18 temperature sensors type NTC thermistors (ZX-Thermometer).
- 2 temperature controller (Arduino DAQ).
- 2 battery chargers (iCharger 208B).
- 1 battery discharger (BK Precision 8500 programmable DC load).
- 1 hot wire anemometer (ALNOR 8525).
- 1 Multimeter.

2.2.2 Temperature profile of experiments

All the performed experiments have a typical profile cell temperature as shown in Figure 2.16 where the temperature behavior of fifteen cells is represented. It can be seen that the central cell of the battery pack (cell number 8 in Figure 2.13) reaches the highest temperature at the end of the discharging process. Then, cells are cooled-down until their temperature fall to the ambient temperature.
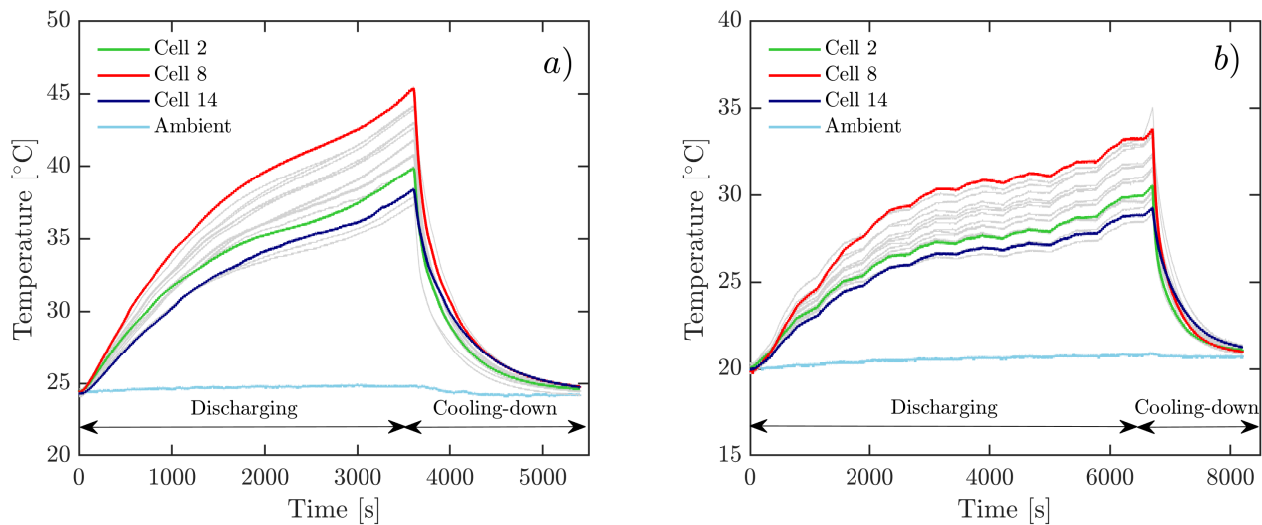
Figure 2.16: Temperature profile of experiments. Discharging at natural convection and cooling-down by forced convection. (**a**) Discharging under 1C. (**b**) Discharging under the HWFET-driving cycle.

2.2.3 Numerical modeling of air flow using CFD

Thermal behavior of the battery pack was modeled numerically using ANSYS Fluent software. Each battery of the module was modeled as a solid cylinder. The heat generation rate in the

cell was customized through the use of a *User Defined Function* (UDF) coded in C language programming. Heat generation in the UDF was implemented by fitting Eq. 1.13 to a Fourier series with seven terms using Matlab Curve Fitting Tool.

Dimensions of the domain and boundary conditions are displayed in Figs. 2.13 and 2.17. On the battery surface was considered the no-slip condition. The condition at the inlet was the inlet velocity, and at the outlet, the atmospheric pressure. Furthermore, a heat transfer coefficient of 5 $\text{Wm}^{-2}\text{K}^{-1}$ was imposed on the battery case. Pressure spatial discretization for natural and forced convection was Body Force Weighted and PRESTO!, respectively. For both cases, a transient simulation was executed with 1 s time step. To obtain a more robust convergence (in both cases), A COUPLED scheme was applied for pressure-velocity coupling. Initial conditions for the temperature of each cell were applied using Patch option in Fluent.
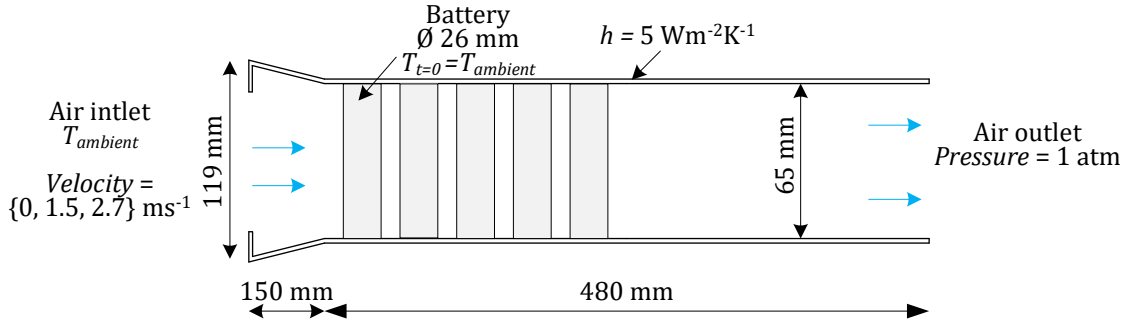
Figure 2.17: Boundary conditions for CFD simulations.

The airflow in the battery pack is considered to be incompressible flow since the maximum velocity of air in a battery pack of an EV is below than 111 ms^{-1}, which is less than one-third of the sound speed [85]. Thus, the governing equations of continuity, momentum, and energy, respectively are formulated as follows [86]:

$$\nabla \cdot \vec{V} = 0, \tag{2.2}$$

$$\frac{\partial \vec{V}}{\partial t} + \left(\vec{V} \cdot \nabla\right)\vec{V} = -\frac{\nabla p}{\rho} + \frac{\mu}{\rho}\nabla^2 \vec{V}, \tag{2.3}$$

$$\frac{\partial (\rho \text{e})}{\partial t} + \nabla \cdot \left(\rho \text{e}\vec{V}\right) = -p\nabla \cdot \vec{V} + \nabla \cdot (k\nabla T) + \Phi, \tag{2.4}$$

where μ is the kinematic viscosity, e is the internal energy (e $= C_v T$ for an ideal gas), and Φ is the viscous dissipation term defined as:

$$\Phi = \mu \left[2\left(\frac{\partial u}{\partial x}\right)^2 + 2\left(\frac{\partial v}{\partial y}\right)^2 + 2\left(\frac{\partial w}{\partial z}\right)^2 + \left(\frac{\partial v}{\partial x} + \frac{\partial u}{\partial y}\right)^2 + \left(\frac{\partial w}{\partial y} + \frac{\partial v}{\partial z}\right)^2 + \left(\frac{\partial u}{\partial z} + \frac{\partial w}{\partial x}\right)^2 \right]$$
$$\tag{2.5}$$

For natural convection modeling, the buoyancy effect in the air is considered through Boussinesq approximation. This approach is suitable for small variations of density:

$$\rho = \rho_0 \left(1 - \beta \Delta T\right), \tag{2.6}$$

where ρ_0 is the constant density of the flow, and β is the thermal expansion coefficient defined as:

$$\beta = -\frac{1}{\rho} \left(\frac{\partial \rho}{\partial T} \right)_p \tag{2.7}$$

Turbulence model

To describe turbulent flows in battery modules, the standard $k - \varepsilon$ model has been widely adopted in many studies due to its robustness [87, 88, 89, 90], and this approach is used in the present study. Furthermore, the shear stress transport model (SST) could be used as well.

The first transport equation for the standard $k - \varepsilon$ model is the kinetic turbulent energy k which is expressed as [30]:

$$\frac{\partial (\rho k)}{\partial t} + \frac{\partial (\rho k u_i)}{\partial x_i} = \frac{\partial}{\partial x_j} \left[\left(\mu + \frac{\mu_t}{\sigma_k} \right) \frac{\partial k}{\partial x_j} \right] + P_k + P_b - \rho \varepsilon - Y_M + S_k, \tag{2.8}$$

where Y_M is the effect of compressibility on turbulence and S_k is the turbulent kinetic source term.

The second equation is the dissipation of turbulent kinetic energy ε, which is given for the following expression [30]:

$$\frac{\partial (\rho \varepsilon)}{\partial t} + \frac{\partial (\rho \varepsilon u_i)}{\partial x_i} = \frac{\partial}{\partial x_j} \left[\left(\mu + \frac{\mu_t}{\sigma_\varepsilon} \right) \frac{\partial \varepsilon}{\partial x_j} \right] + C_{1\varepsilon} \frac{\varepsilon}{k} (G_k + C_{3\varepsilon} G_b) - C_{2\varepsilon} \rho \frac{\varepsilon^2}{k} + S_\varepsilon \tag{2.9}$$

where S_ε is the source term for the turbulent dissipation, and ν_t is the turbulent viscosity described by:

$$\mu_t = \rho C_\mu \frac{k^2}{\varepsilon} \tag{2.10}$$

The component of turbulent kinetic energy owing to the mean velocity gradients P_k, named production, is formulated as follows:

$$P_k = -\rho \overline{u_i' u_j'} \tag{2.11}$$

The component of turbulent kinetic energy owing to buoyancy P_b is

$$P_b = \beta g_i \frac{\mu_t}{\mathrm{Pr}_t} \frac{\partial T}{\partial x_i} \tag{2.12}$$

where $\mathrm{Pr}_t = 0.85$ is the turbulent Prandtl number.

The constants of the model are given by:

$$C_\mu = 0.09, \ C_{1\varepsilon} = 1.44, \ C_{2\varepsilon} = 1.92, \ \sigma_k = 1.0 \text{ and } \sigma_\varepsilon = 1.3$$

Battery module meshing

A discharging test at 1C for the battery module with fifteen cells was simulated to perform a mesh independence test. Three meshes were evaluated (see Table 2.10). Maximum temperature of the hottest cell (number 8) at the end of discharging was the parameter of comparison among the meshes. A mesh with 751740 elements (mesh number 3) was selected for future simulations and the convergence criterion was once the residuals took a value around 1×10^{-3}, 1×10^{-6} and 1×10^{-8} for continuity, velocity and energy equation, respectively. Moreover, five inflation layers were developed around each cell (see Figure 2.18) to capture boundary layer effects.

Table 2.10: Mesh independence test for the battery module.

Description	Mesh 1	Mesh 2	Mesh 3
Number of elements	49116	247820	751740
Inflation	No	No	Yes
Maximum temperature of cell number 8 (°C)	42.41	42.69	42.73
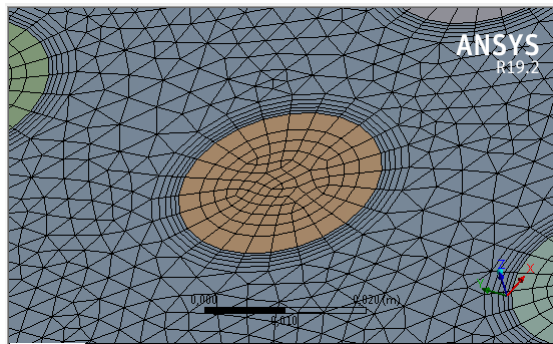
Figure 2.18: Meshing detail around one cell in the battery bank.

2.3 Methodology for temperature estimation based on particle filter

To estimate the temperature in the battery pack using particle filter approach, a mathematical model of the battery system (process equation) and measurements are needed. In the present study, temperature measurements of one cell per string are employed. PF is implemented solving Eqs.1.25, 1.26 and 1.27.

2.3.1 Thermal model for a single battery string

The surface temperature of a cell T_s can be estimated through the use of a lumped model given by:

$$\frac{\mathrm{d}T}{\mathrm{d}t} = \frac{1}{\tau} \left(T_{amb} - T(t) \right) + \frac{Q_{gen}(t)}{C_p}, \tag{2.13}$$

where τ is the thermal time constant written as:

$$\tau = \frac{C_p}{hA_s}. \tag{2.14}$$

Moreover, heat generation can be simplified as follows:

$$Q_{gen} = I^2 R_T \tag{2.15}$$

A thermal model of a battery string is formulated extending the single-cell thermal model and considering the cell to cell heat transfer. The scheme of a single battery string and its equivalent thermal model is displayed in Figure 2.19.
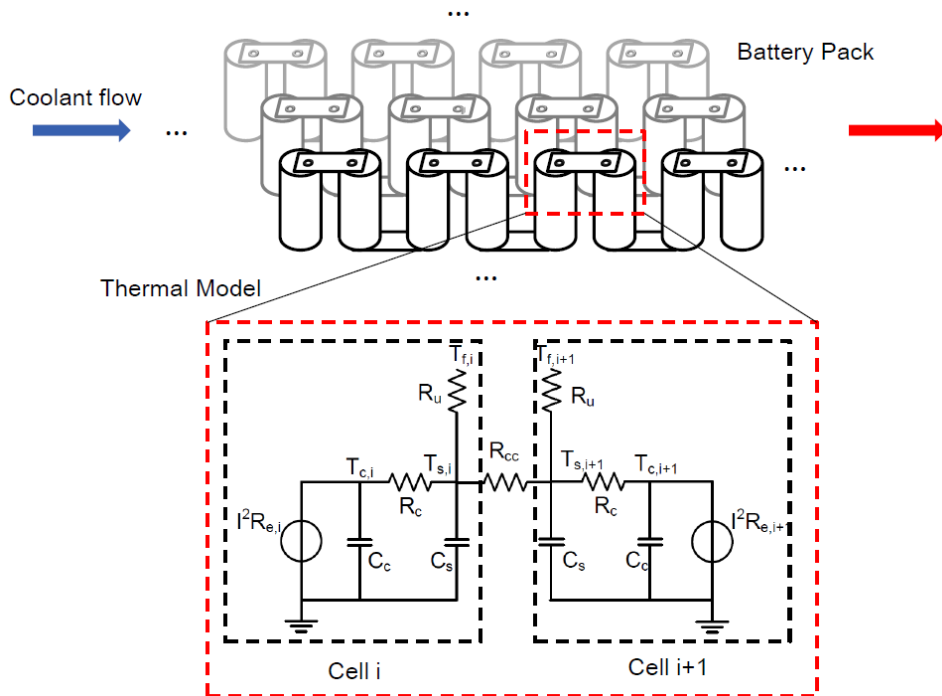
Figure 2.19: Scheme of a single battery string and a equivalent-circuit thermal model [91].

The temperature behavior of the kth cell for a string with n cells can be computed by Eqs. 2.16, 2.17, 2.18, which are formulated based on the work proposed by Lin et al. [91]::

$$\frac{dT_{s,i}}{dt} = \frac{1}{\tau}\left(T_{amb,i} - T_i\right) + \frac{Q_{gen,i}}{C_p} + \frac{Q_{cc,i}}{C_p}, \tag{2.16}$$

$$Q_{cc,i} = \begin{cases} \left(T_{s,2} - T_{s,1}\right)/R_{cc}, & i = 1 \\ \left(T_{s,i-1} + T_{s,i+1} - 2T_{s,i}\right)/R_{cc}, & i = 2, ..., n-1 \\ \left(T_{s,n-1} - T_{s,n}\right)/R_{cc}, & i = n \end{cases} \tag{2.17}$$

$$T_{amb,i} = \begin{cases} T_{amb,in}, & i = 1 \\ T_{amb,i-1} + \frac{T_{s,i-1} - T_{amb,i-1}}{R_{out}C_f}, & i = 2, ..., n, \end{cases} \tag{2.18}$$

where Q_{cc} is the heat transfer through a conduction resistance R_{cc}, $R_{out} = \tau/C_p$ is the convection resistance, τ is a thermal time constant (given by Eq. 2.14), and C_f is the heat capacity of the air.

2.3.2 Fractal time model as process equation

A better agreement between experimental measurements of cell temperature and a fitting model is obtained employing a fractal formulation which takes into consideration an anomalous temperature relaxation [92]. A fractal derivative can be written as [93]:

$$\frac{dF^\beta}{dt^\gamma} = \lim_{\Delta t \to 0} \frac{F^\beta(t + \Delta t) - F^\beta(t)}{(\Delta t + t)^\gamma - t^\gamma}, \tag{2.19}$$

where $\beta > 0$ and $\gamma > 0$ are scaling factors for the dependent variable and time, respectively.

Using only one scaling factor α and combining Eq. 2.16 and Eq. 2.19 yields [92]:

$$\frac{dT^\alpha}{dt^\alpha} = \frac{1}{\tau^\alpha}\left(T_{amb}^\alpha - T^\alpha(t^\alpha)\right) + \frac{Q_{gen}^\alpha(t^\alpha)}{C_p^\alpha} + \frac{Q_{cc,i}^\alpha(t^\alpha)}{C_p^\alpha}, \tag{2.20}$$

where $\tau = C_p R_{out}$ is the thermal time constant.

To apply the particle filter, a discrete formulation for the process equation is needed. Then, based on the Euler discretization of Eq. 2.20, the process equation to estimate the temperature of a single cell in the string at each time step k is written as:

$$T_k(t^\alpha) = \left\{\left(t_k^\alpha - t_{k-1}^\alpha\right)\left[-\frac{1}{\tau_{k-1}^\alpha}\left(T_{k-1}^\alpha(t^\alpha) - T_{amb}^\alpha\right) + \frac{Q_{gen,k-1}^\alpha(t^\alpha)}{C_p^\alpha} + \frac{Q_{cc,i}^\alpha(t^\alpha)}{C_p^\alpha}\right] + T_{k-1}^\alpha(t^\alpha)\right\}^{1/\alpha} \tag{2.21}$$

2.3.3 Experiments

The array of 15 cells was used to estimate the cell temperature using particle filter. Two sets of temperature measurements on the surface of each cell were performed: at discharging and cooling-down process. Experiments for discharging process were carried out at 1C-rate. First, the cells were discharged under natural convection during 1800 s, and then, the cells were cooled-down by forced convection (at 1.5 m/s and 2.7 m/s) during 1800 s. Only temperature measurements during forced convection were considered to implement the particle filtering because of the limitations of process equation to model natural convection in a battery module. For the second type of experiments, cells were discharged under natural convection at constant current of 0.25C, 0.5C, and 1C-rate, respectively. When a discharge finished, immediately batteries were cooled-down by forced convection at 1.5 and 2.7 m/s, respectively for each discharging rate applied. Measurements at forced convection were used for particle filtering as well. A description of experiments is detailed in Figure 2.20.
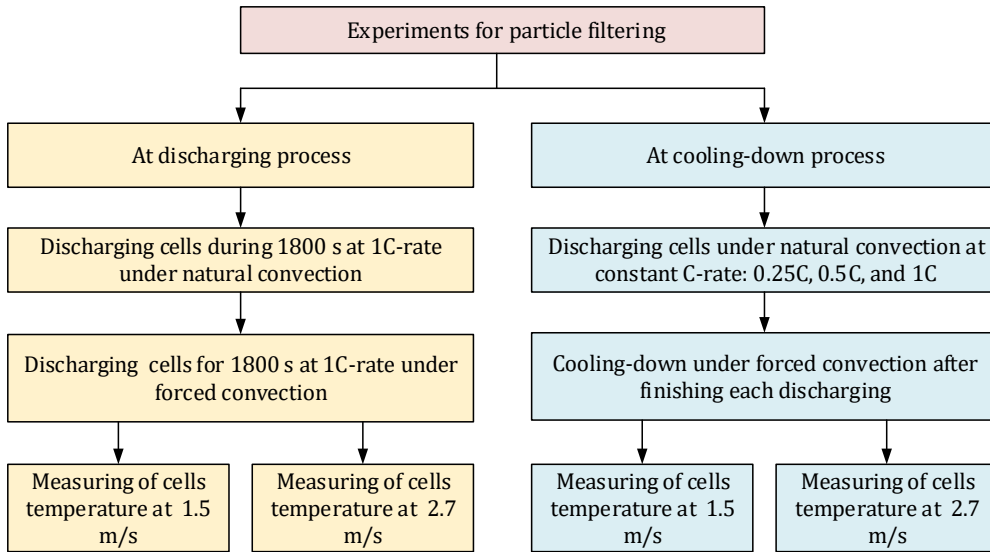
Figure 2.20: Scheme of experiments for particle filtering.

2.3.4 Implementation of particle filter

The battery module was arranged into three strings as shown in Figure 2.21. Seven states were estimated per each string: α, τ, and the temperature of the five cells. The temperature of the first cell of each string (cell number 1, 2, and 3, respectively) was taken as the observation state (Eq. 1.21) while the temperature of the other four cells (per string) were estimated by PF. It is not mandatory to estimate the state of the cells taken as observation, but it lets to know the behavior of the fractal model. After temperature and parameters α and τ are formulated as a state space vector (Eq. 1.20), temperature states were estimated using Eqs. 1.25 and 1.26 while parameters α and τ were obtained by artificial evolution using Eqs. 1.27. The general goal of using PF in this study is to save temperature sensors in the battery module. Thus, only three temperature sensors are required to estimate the temperature of the whole module.
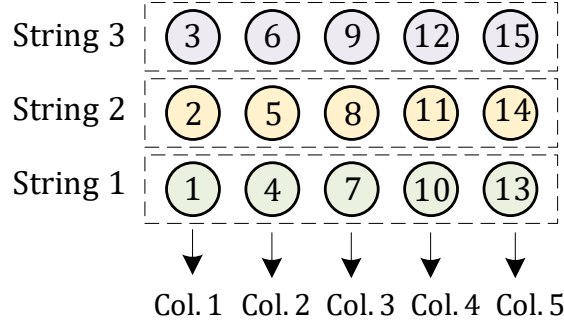
Figure 2.21: Arrangement of cells for particle filtering estimation.

The following considerations were made:

- Ambient temperature was assumed as constant.
- All measurements were performed using fifteen cells at once.
- Thermal effects due to battery connectors (thermal contact resistance) were considered as negligible.
- Changing of internal resistance of cells due to aging was not considered.

Parameters of particle filtering

The particle filter was implemented using the following parameters:

- Number of particles: 100.
- Process noise for α: 0.05.
- Process noise for τ: 1.25.
- Process noise of cells temperature for each i string: $T_{\mathrm{i},col_1} = 0.025$; $T_{\mathrm{i},col_2} = 0.05$; $T_{\mathrm{i},col_3} = 0.05$; $T_{\mathrm{i},col_4} = 0.05$; $T_{\mathrm{i},col_5} = 0.05$.
- Observation noise: 0.5.
- Initial condition of stretching factor α: 1.
- Initial condition of thermal time constant τ: τ_0.

Taking into consideration that $\tau = C_p/(hA_s)$, the initial condition τ_0 was taken for the cells in the first column (see Figure 2.21) based on the Zukauskas' correlation for external forced convection across bank of tubes [34]:

$$\overline{Nu}_D = C_1 C_2 Re_{D,max}^m Pr^{0.36} \left(\frac{Pr}{Pr_s}\right)^{1/4}, \tag{2.22}$$

$$h = \frac{\overline{Nu}_D k_f}{D}, \tag{2.23}$$

where $\overline{Nu}_D$ is the average Nusselt number, C_1, C_2 and m are constants, Pr is the Prandtl number, Pr_s is the Prandtl number evaluated at surface temperature of the cell, and $Re_{D,max}$ is the maximum Reynolds number.

41

Due to the air flow speed was measured in the tubes of the bench (see Figure. 2.13a), air speed just at the inlet of the battery module v_{inlet} (in front of cells number 1, 2 and 3) was computed using the continuity flow equation:

$$A_{tubes} \times v_{tubes} = A_{\mathrm{inlet}} \times v_{\mathrm{inlet}}, \tag{2.24}$$

where A_{tubes} and A_{inlet} are the tubes and inlet battery module cross-sectional area, respectively, and v_{tubes} is the air speed in the tubes. Thereby, applying Eq. 2.24, when v_{tubes} was 1.5 and 2.7 ms^{-1}, v_{inlet} was 2.6, and 4.60 ms^{-1}, respectively. These last two values were employed for PF modeling.

2.4 Methodology for thermal runaway modeling and stability study

In this section, a methodology to explore thermal runaway by mathematical modeling is presented. First, the thermal abuse model is described and then, a non-dimensional analysis is proposed to evaluate the stability of the cell.

2.4.1 Thermal abuse modeling

The profile of temperature during TR is predicted by thermal abuse model. This model was firstly proposed by Harchard et al. [8] and then extended by Kim et al. [9]. The model is based on Arrhenius equation and it embraces a system of equations which describes the reactions during the decomposition of the positive electrode, negative electrode and SEI as follows:

$$\frac{\mathrm{d}c_{sei}}{\mathrm{d}t} = -c_{sei}A_{sei} \cdot \exp\left(-\frac{E_{a,sei}}{RT}\right) \tag{2.25}$$

$$\frac{\mathrm{d}c_{ne}}{\mathrm{d}t} = -c_{ne}A_{ne} \cdot \exp\left(-\frac{z_{sei}}{z_{sei,0}}\right)\exp\left(-\frac{E_{a,ne}}{RT}\right) \tag{2.26}$$

$$\frac{\mathrm{d}z_{sei}}{\mathrm{d}t} = c_{ne}A_{ne} \cdot \exp\left(-\frac{z_{sei}}{z_{sei,0}}\right)\exp\left(-\frac{E_{a,ne}}{RT}\right) \tag{2.27}$$

$$\frac{\mathrm{d}\alpha}{\mathrm{d}t} = \alpha\left(1-\alpha\right)A_{pe} \cdot \exp\left(-\frac{E_{a,pe}}{RT}\right) \tag{2.28}$$

$$\frac{\mathrm{d}c_{el}}{\mathrm{d}t} = -c_{el}A_{el} \cdot \exp\left(-\frac{E_{a,el}}{RT}\right), \tag{2.29}$$

where subscripts sei, ne, pe and el represent SEI layer decomposition reaction, reaction between the negative electrode and the electrolyte, reaction between the positive electrode and the electrolyte, and electrolyte decomposition reaction, respectively, z_{sei} is a dimensionless measure of a SEI layer thickness, $z_{sei,0}$ is the reference SEI layer thickness, c_{sei} is the fraction of concentration of meta-stable species containing lithium in the SEI layer, c_{ne}, is the fraction of concentration of lithium in the negative electrode, z_{sei} refers to the SEI layer thickness, α represents the degree of conversion of the cathode, and c_{el} is the concentration of electrolyte. All these variables are dimensionless. R is the universal gas constant. Table 2.11 shows the description of initial conditions and values of the parameters.

Based on Eq. 1.3, energy balance for a single cell under abuse conditions can be rewritten as:

$$C_p\frac{\partial T}{\partial t} = Q_{conv} + Q_{rad} + Q_{gen} + Q_{r,ab}, \tag{2.30}$$

where heat of reactions per unit volume under abuse conditions $Q_{r,ab}$ is given by:

$$Q_{r,ab} = H_{sei}m_{ne}\left|\frac{\mathrm{d}c_{sei}}{\mathrm{d}t}\right| + H_{ne}m_{ne}\left|\frac{\mathrm{d}c_{ne}}{\mathrm{d}t}\right| + H_{pe}m_{pe}\left|\frac{\mathrm{d}\alpha}{\mathrm{d}t}\right| + H_{el}m_{el}\left|\frac{\mathrm{d}c_{el}}{\mathrm{d}t}\right|, \tag{2.31}$$

where the meaning of each term on the right hand side in Eq. 2.31 is the heat released due to: SEI decomposition, anode decomposition, cathode decomposition, and electrolyte decomposition, respectively (more details of the rest of parameters are presented in Table 2.11).

Table 2.11: Parameters for thermal abuse model

Parameter	Description	Value	Reference
A_{el}	Frequency factor for electrolyte decomposition	$5.14 \cdot 10^{25}$ s^{-1}	[45]
A_{ne}	Frequency factor for anode decomposition	$2.5 \cdot 10^{13}$ s^{-1}	[8]
A_{pe}	Frequency factor for cathode decomposition	$6.67 \cdot 10^{13}$ s^{-1}	[8]
A_{sei}	Frequency factor for SEI decomposition	$1.67 \cdot 10^{15}$ s^{-1}	[8]
$E_{a,el}$	Activation energy for electrolyte decomposition	$4.55 \cdot 10^{-19}$ J	[8]
$E_{a,ne}$	Activation energy for anode decomposition	$2.24 \cdot 10^{-19}$ J	[8]
$E_{a,pe}$	Activation energy for cathode decomposition	$2.32 \cdot 10^{-19}$ J	[45]
$E_{a,sei}$	Activation energy for SEI decomposition	$2.24 \cdot 10^{-19}$ J	[8]
H_{el}	Heat released by electrolyte decomposition	$1.55 \cdot 10^5$ J kg^{-1}	[45]
H_{ne}	Enthalpy of anode decomposition	$1.714 \cdot 10^6$ J kg^{-1}	[8]
H_{pe}	Enthalpy of cathode decomposition	$3.14 \cdot 10^5$ J kg^{-1}	[8]
H_{sei}	Heat released by SEI decomposition	$2.57 \cdot 10^5$ J kg^{-1}	[8]
m_{el}	Specific electrolyte content in jellyroll	406.9 kg m^{-3}	[9]
m_{ne}	Specific carbon content in jellyroll	610.4 kg m^{-3}	[9]
m_{pe}	Specific positive active content in jellyroll	1221 kg m^{-3}	[9]
$c_{el,0}$	Initial value of fraction of electrolyte	1	[9]
$c_{ne,0}$	Initial value of fraction of Li in anode	0.75	[8]
$c_{sei,0}$	Initial value of fraction of Li in SEI	0.15	[8]
$z_{sei,0}$	Initial value of dimensionless SEI thickness	0.033	[8]
α_0	Initial value of degree of conversion of cathode	0.04	[8]

Kim. et al. [9] found that most of the time 3D models match with the lumped model. Thus, a thermal abuse model based on a lumped system is proposed. The heat generation rate term is not included when oven test is modeled (discharging current is equal to zero). Substituting Eqs. (1.5), (1.6) and (2.31) into Eq. (2.30) yields:

$$
\frac{\mathrm{d}T}{\mathrm{d}t} = \left[\frac{-A_{surf,c}}{Vol_c} \left[h\left(T - T_{amb}\right) + \varepsilon\sigma\left(T^4 - T_{amb}^4\right) \right] + Q_{gen} \right.
$$
$$
\left. - H_{sei}m_{ne}\frac{\mathrm{d}c_{sei}}{\mathrm{d}t} - H_{ne}m_{ne}\frac{\mathrm{d}c_{ne}}{\mathrm{d}t} + H_{pe}m_{pe}\frac{\mathrm{d}\alpha}{\mathrm{d}t} - H_{el}m_{el}\frac{\mathrm{d}c_{el}}{\mathrm{d}t} \right] / C_p, \qquad (2.32)
$$

where $Vol_c = 2.8166 \cdot 10^{-5}$m^3 refers to the measured volume of jelly roll of the 26650 cell, which is the core of the battery where the anode, cathode, and separator are rolled (in a cylindrical cell).

2.4.2 Non-dimensional analysis on of LIB thermal stability

To evaluate the stability of the LIB system. First, we consider that the sum of heat of reaction can be simplified as [59]:

$$
\sum \Delta H m A \exp\left(\frac{-E_a}{RT}\right) = H'm'A'\exp\left(\frac{-E_a'}{RT}\right). \qquad (2.33)
$$

Then, neglecting the entropy term in heat generation rate, the following expression for a cell can be formulated:

$$\rho Vol_c \frac{\mathrm{d}T}{\mathrm{d}t} = H'm'A' \exp\left(\frac{-E_a'}{RT}\right) + I^2 R_T$$
$$- A_{surf,c} h \left(T - T_{amb}\right) - A_{surf,c} \varepsilon \sigma \left(T^4 - T_{amb}^4\right), \tag{2.34}$$

Equation 2.34 is nondimensionalized using the following transformations [94]:

$$T^* = \frac{R}{E_a} T \tag{2.35}$$

$$t^* = \frac{H'm'A'R}{\rho Vol_c E_a} t \tag{2.36}$$

$$\tag{2.37}$$

Thus, equation 2.34 can be written as:

$$\frac{\mathrm{d}T^*}{\mathrm{d}t^*} = \alpha + \exp\left(-\frac{1}{T^*}\right) - \beta T^* - \gamma T^{*4}, \tag{2.38}$$
$$= f\left(T^*\right),$$

where

$$\alpha = \frac{I^2 R_T}{H'm'A'} + \beta T_{amb} + \gamma T_{amb}^4 \tag{2.39}$$

$$\beta = \frac{h A_{surf,c} E_a}{H'm'A'R} \tag{2.40}$$

$$\gamma = \frac{A_{surf,c} \varepsilon \sigma}{H'm'A'} \tag{2.41}$$

Fixed points are given when $\dot{T}^* = 0$ and they can be classified as stable fixed points (attractors or sinks given by a negative slope of the tangent line at that point) and unstable fixed points (repellers or sources given by a positive slope of the tangent line at that point), which represent stable and unstable equilibrium, respectively [64]. These fixed points are located at the intersection of the horizontal axis with $f(T^*)$.

Chapter 3

Results and discussion

In this chapter, results of thermal behavior of a single cell and a battery module are exposed. An application of particle filter to estimate the temperature of cells in a battery pack is also presented. Moreover, thermal abuse model for a single cell is implemented to describe thermal runaway, and a non-dimensional analysis is performed to study the stability of a cell.

3.1   Results of thermal modeling of a single cell

This section presents a comparative study among three of the most employed approaches to study the thermal behavior of LIBs: a lumped model, a 3D-CFD model, and an electrochemical approach using the Newman, Tiedemann, Gu and Kim (NTGK) model. These formulations were solved numerically. Furthermore, voltage was simulated using NTGK model. All of these simulations were compared with experimental tests, at constant current discharge rate, and under the highway fuel economy test (HWFET) driving cycle using a 26650 lithium cobalt oxide (LCO) battery.

3.1.1   Heat generation rate

The behavior of the volumetric heat generation rate computed by Eq. 1.13 and the NTGK model is depicted in Figure 3.1. Heat generation given by NTGK approach at constant current tends to increase, specially at the beginning and at the end of the discharge time (Figure 3.1a). The curves based on Bernardi's equation (dashed lines) have a concave region due to the effect of the entropic term. For HWFET driving cycle, heat generation varies according to the current profile as shown in Figure 2.4.

Average of volumetric heat generation is reported in Table 3.1. In general, experimentally-based values (Equation 1.13) are moderately close to values obtained numerically by NTGK model, but there exists a maximum percentage of variation of 30.1 % at 0.5C.
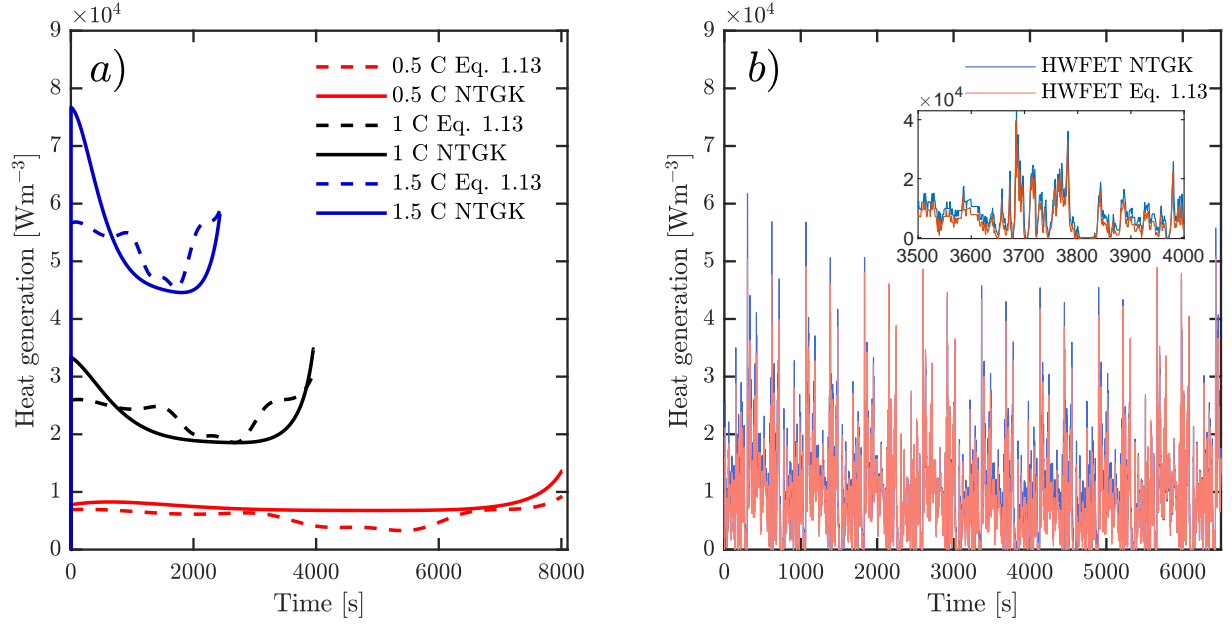
Figure 3.1: Battery volumetric heat generation: (**a**) At constant C-rate, (**b**) Under HWFET driving cycle.

Table 3.1: Average heat generation.

Current	Eq. 1.13 (Wm^{-3})	NTGK model (Wm^{-3})	Percentage of variation (%)
0.5C	5761	7542	30.9
1C	23588	22228	5.8
1.5C	52715	52465	0.5
HWFET-cycle	8597	9861	14.7

3.1.2 Heat transfer coefficient

According to Table 3.2, experimental heat transfer coefficients are in moderate agreement with their computed values, although the first ones are slightly higher than predicted results. Moreover, h_{conv} is very close to a value of 5 Wm^{-2}K^{-1} used by some authors [95, 96, 97] for studies on LIBs performance under natural convection. Experimental h_{conv} coefficient was utilized in all simulations. Besides, it is evident from Table 3.2 that h_{rad} has practically the same contribution of h_{conv} in terms of heat exchange under free convection. This was also reported by Allafi et al. [98]. Radiation effects were considered in simulations. In general, heat transfer coefficient raises as discharge current increases.

47

Table 3.2: Convection coefficient comparison.

| Current | h_{comb} (Wm^{-2}K^{-1}) | | h_{conv} (Wm^{-2}K^{-1}) | | h_{rad} (Wm^{-2}K^{-1}) |
	Exp.	Computed Eqs. 1.8, 1.9, 1.11	Exp.	Computed Eq. 1.11	Computed Eq. 1.9
0.5C	8.4	8.5	3.6	3.7	4.8
1C	10.2	9.2	5.3	4.3	4.9
1.5C	12.8	9.8	7.7	4.8	5.0
HWFET-cycle	8.8	8.7	3.9	3.8	4.9

3.1.3 Temperature performance comparison

All three evaluated approaches successfully estimate the cell temperature as displayed in Figure 3.2. The standard deviation of the experimental temperatures at each discharging test is 0.3 °C, 0.2 °C, 0.3 °C, and 0.2 °C for 0.5C, 1C, 1.5C, and HWFET-cycle, respectively. The maximum temperature increase was 18.1 °C for 1.5C rate. Moreover, measured temperature profile of the cell is the same as its respective heat flux curve (Figure 2.5).

Figure 3.2: Comparison of temperature increase among different methods at different discharging currents: (**a**) 0.5C-rate. (**b**) 1C-rate. (**c**) 1.5C-rate. (**d**) HWFET-cycle. Ambient temperature was 24 ± 0.3 °C, 24 ± 0.3 °C, 23 ± 0.2 °C, and 25 ± 0.3 °C, respectively
.

All the simulated models are consistent with their experimental temperature. The lumped and 3D-CFD models have practical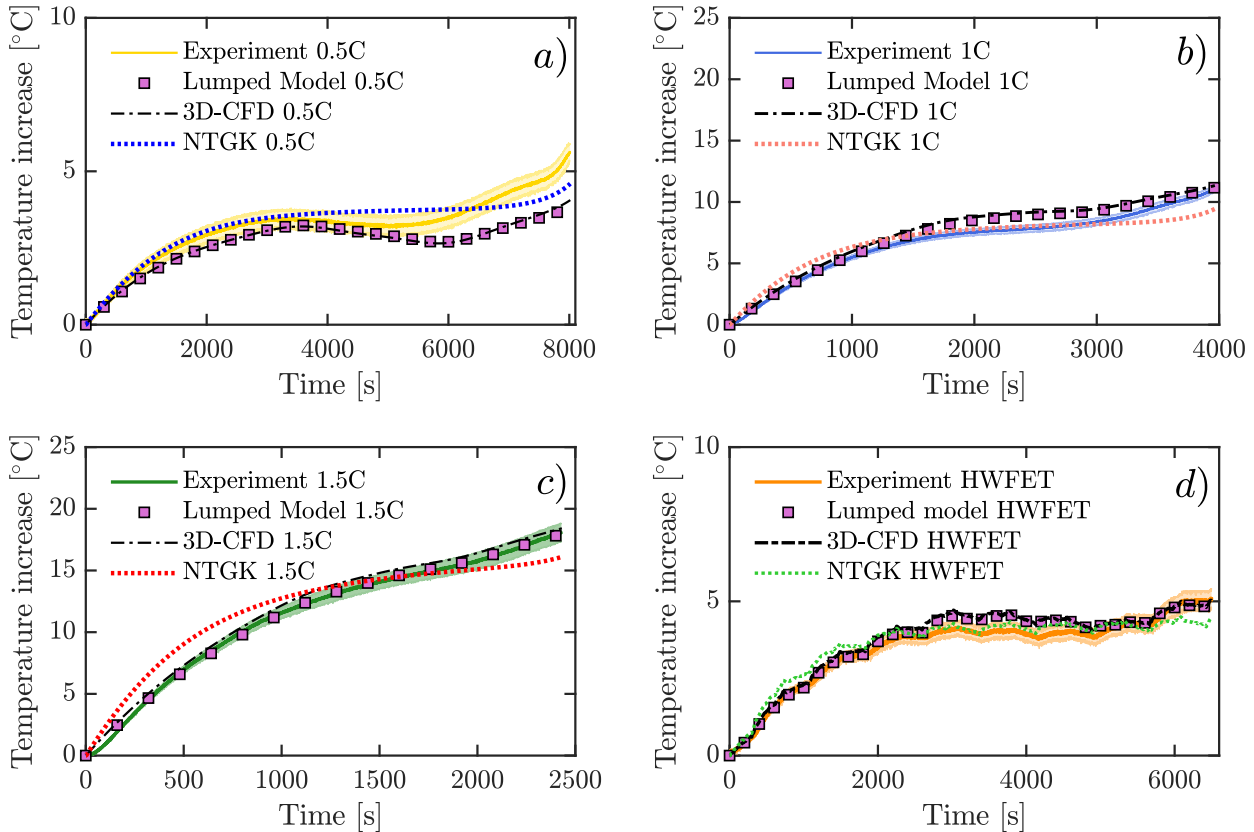ly the same temperature distribution, it is mainly due to the heat generation term is the same for both. Nevertheless, there exist minimal discrepancies comparing the temperature profile among the proposed methods. This fact is supported by computing root mean square (RMS) errors, which are detailed in Table 3.3, where NTGK model has the lower error at 0.5C and 1C; however, this model has the maximum error (1.3 °C) at 1.5C. For the HWFET-cycle, all models are in the same order of RMS error capturing satisfactorily the dynamics of the battery temperature under a real driving cycle (Figure 3.2d). One advantage of CFD-based models is the computation of spatial temperatures, and also their flexibility to combine cells into a pack under different cooling conditions. In general, electrochemical models are widely used to model temperature and voltage of batteries due to their good agreement between numerical and experimental data [68], although these models require cautious attention to determine parameters. For instance, in [99] the ionic electrical conductivity of the liquid phase, and the diffusion coefficient of lithium ions in the liquid and solid phases are formulated in terms of electrolyte concentration and temperature. Moreover, in [100] authors expose different procedures to determine internal resistance and thermal conductivity of a cell.

Table 3.3: RMS errors for the different cases. Units °C.

Current	Lumped	3D-CFD	NTGK	Experimental ΔT (°C)
0.5C	0.7	0.6	0.3	5.6
1C	0.7	0.9	0.8	11.1
1.5C	0.2	0.6	1.3	18.1
HWFET-cycle	0.3	0.3	0.3	5.1

Moreover, lumped model can be more practical to evaluate long simulation time profiles. For instance, Figure 3.3 (bottom) shows the temperature behavior of the LCO battery considered in this study, simulated at different ambient temperatures under a real driving-cycle of a Nissan Leaf in a rural road with light traffic during approximately 5.2 hours. The simulation time for each temperature distribution was 29.1 s. The application of the lumped model could be extended to estimate the temperature of a battery pack [101, 91], and also battery degradation in electric vehicles [102]. Currently, the application of lumped model to estimate the temperature of an EV battery pack under different real driving cycles is being investigated. Further results will be reported in future research publications.

Besides, the models also estimate the battery temperature under forced convection. For example, Figure 3.4 shows a simulation of the models under the maximum discharging rate (2C) of the battery studied here considering $h_{conv} = 100 \, \mathrm{Wm^{-2}K^{-1}}$. As the discharge current increase, the temperature given by the NTGK model tends to be greater with respect to the other models at the beginning of the discharge time. This behavior mainly depends on the functions U and Y, and could be improved by adjusting the constant C_1. Moreover, one characteristic of the ICR 26650 battery is that its tested capacity decreases to approximately 3.6 Ah when the maximum discharging current is applied.
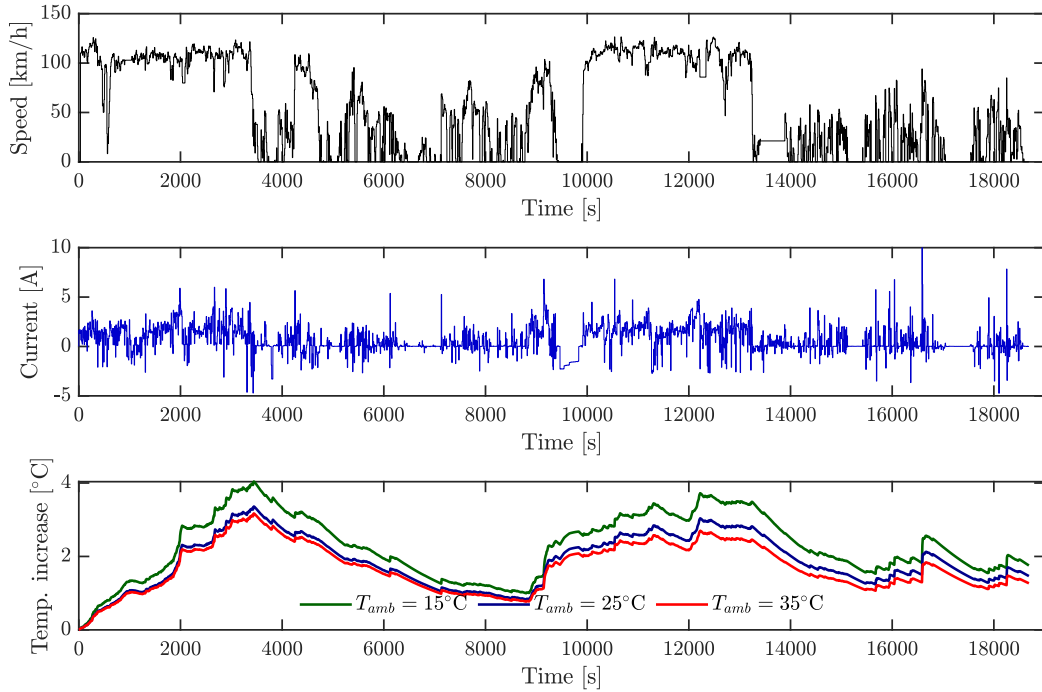
Figure 3.3: Battery temperature simulation under a real driving cycle. *Top*: Velocity profile of a Nissan Leaf in a rural road with light traffic. *Middle*: Scaled current. *Bottom*: Temperature increase of the LCO 26650 LIB simulated at different ambient temperatures using the lumped model.
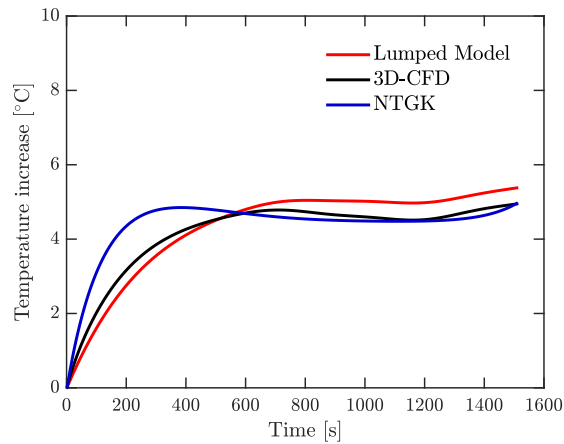
Figure 3.4: Comparison of methods for a simulated discharge at 2C under $h_{conv} = 100$ $Wm^{-2}K^{-1}$.

The behavior of all the approaches can be improved. For instance, the heat capacity is the most sensitive parameter for thermal modeling while thermal conductivity has a minor impact on the simulations [103]. Then, a more accurate value of thermal parameters can be found by using calorimetric techniques. Moreover, the use of a full electrochemical model (Newman formulation) is relevant to study the physical phenomena of Li-ion transport.

50

3.1.4 Voltage

Figure 3.5 depicts the comparison between experimental and simulated voltage by using NTGK model. Both values are in good agreement. For HWFET driving-cycle, peak values of experimental voltage are slightly higher than the numerical result. In general, the dynamical behavior of the system is well captured. There exist some discrepancies specially at the end of the discharge process, where the minimal voltage is not reached; this behavior was also reported by Celik et al. [104] using NTGK model, and by Li et al. [105] using the MSMD approach under the electric circuit model. Voltage given by NTGK model could be improved by adjusting the C_2 constant.
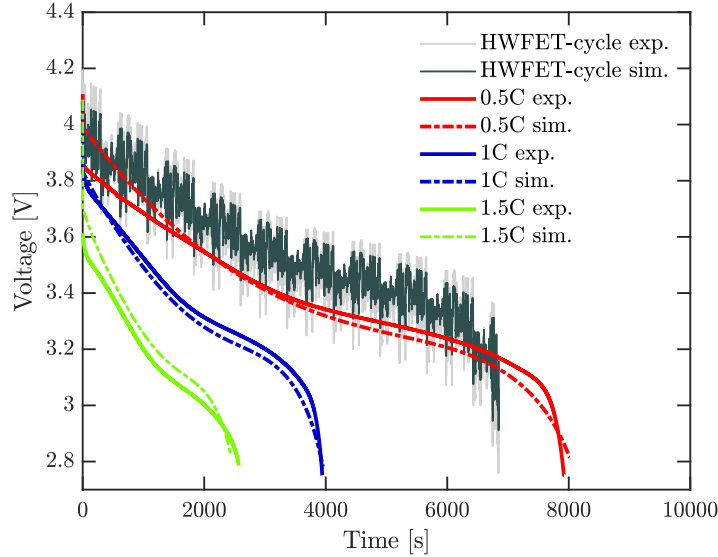
Figure 3.5: Comparison of experimental and simulated voltage using the NTGK model.

Computational time

CPU time consuming is a relevant aspect while comparing among different proposed models in this work. All cases were run using a standard CPU (3.5 GHz, 16 GB RAM). As indicated in Table 3.4, the lumped model requires time in the order of seconds for solving the temperature profile. NTGK model is more time consuming since it has to evaluate many electrochemical equations in the battery domain, even under the consideration that its mesh has fewer number of elements with respect to 3D-CFD approach. Moreover, if a mesh with more number of elements is used, and if fluid flow around them is solved, the computational time will increase considerably.

Table 3.4: Execution time for the different models.

Current	Lumped	3D-CFD	NTGK
0.5C	2.03 s	1612 s	27120 s
1C	1.08 s	776 s	14280 s
1.5C	0.61 s	463 s	8989 s
HWFET-cycle	7.23 s	1296 s	26460 s

The temperature profile of a LCO 26650 lithium-ion battery under constant and complex current rates was evaluated by comparing three of the most used methods to study the thermal behavior of LIBs: a lumped model, 3D-CFD approach and an electrochemical method based on NTGK with dual potential approach. The heat generation rate, heat capacity, and heat transfer coefficients were estimated to predict the temperature at the cell surface.

In general, NTGK model has the best performance over the rest of the studied models due to that it is capable to solve not only the temperature field of the cell, but also voltage, heat generation and other properties. This approach provides the lower temperature error at rates of 0.5C and 1C. Nevertheless, this model presents the higher RMS error of 1.3 °C at 1.5C, where the maximum temperature increase of the cell was 18.1 °C. Under the driving cycle, the temperature increase was 5.1 °C, and all the models were in the same order of error. Lumped model is suitable to be used satisfactorily in a wide range of LIB operating conditions and it presents a very similar temperature profile as 3D formulation since both models depend on the same heat generation rate and thermal parameters. Under free convection, radiation plays a relevant role in terms of heat transfer rate, this contribution is practically the same as convection. Besides, the heat transfer coefficient increases as the discharging current does.

3.2 Results of thermal modeling of a battery pack

An evaluation of thermal performance of a battery pack is crucial to avoid loss of capacity of cells and accidents. Many studies on thermal behavior of a battery arrangement have been developed numerically using computational packages such ANSYS, e.g. see [6, 106, 107, 86, 87]. To describe turbulent flows in battery modules, the standard $k-\varepsilon$ model has been widely adopted in many studies due to its robustness [87, 88, 89, 90]. Furthermore, the shear stress transport model (SST) has been used as well. This turbulence model is enhanced to predict the separation of flow under adverse pressure gradients [86]. In this chapter, the thermal behavior of a battery pack with fifteen cells is analyzed. Experimental temperature of cells was compared to numerical simulations obtained by Fluent-CFD.

3.2.1 Results for discharging under natural convection

Under natural convection, the temperature distribution of the battery module shows that the center of the domain is the hottest zone. This phenomenon is observed in all the experiments. Thus, Figures 3.6, 3.7, 3.8, and 3.9 shows the temperature at the end of the discharging at 1C, 0.5C, 0.25C, and HWFET-cycle, respectively, where the initial temperature of the cells was 24 °C, 24 °C, 18 °C, and 20 °C, respectively. Temperature of cells is higher as discharging rate increases because heat generation rate of LIBs is directly proportional to discharge current. According to simulations, air temperature in the battery case mainly increases in the vicinity of cells and it is slightly higher at the top of the battery case rather than the bottom due to the density variation of the fluid. The 3D-CFD formulation with the Bousinessq approximation were used to capture the free convection phenomenon.
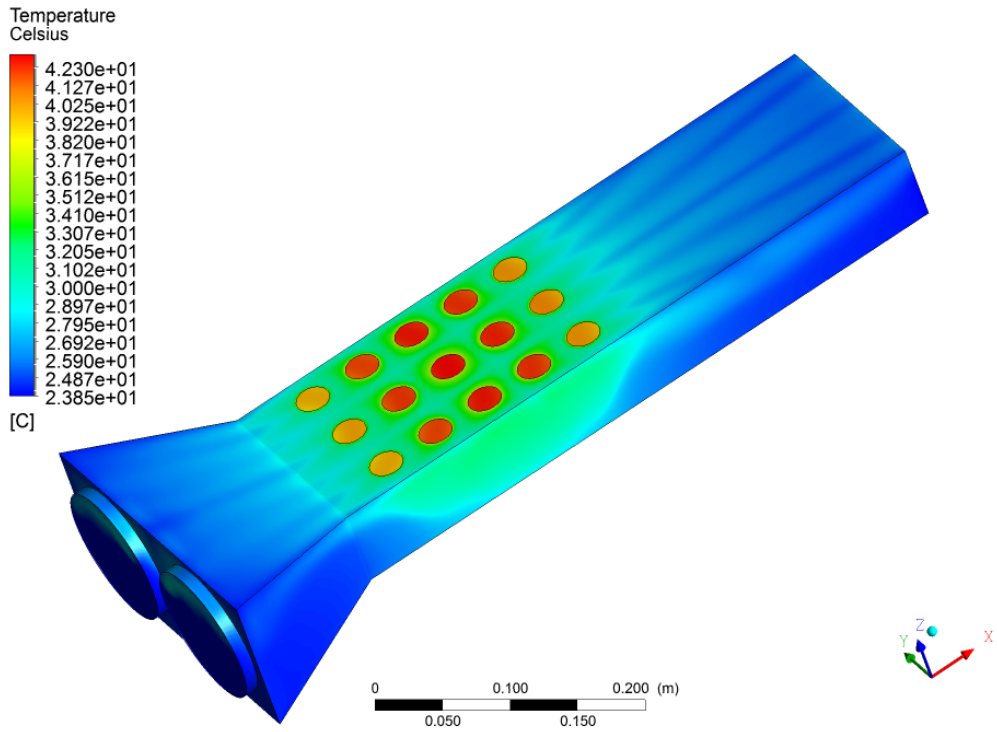
Figure 3.6: Temperature distribution of the module at the end of discharging under 1C and $T_{initial} = 24\,°\mathrm{C}$.
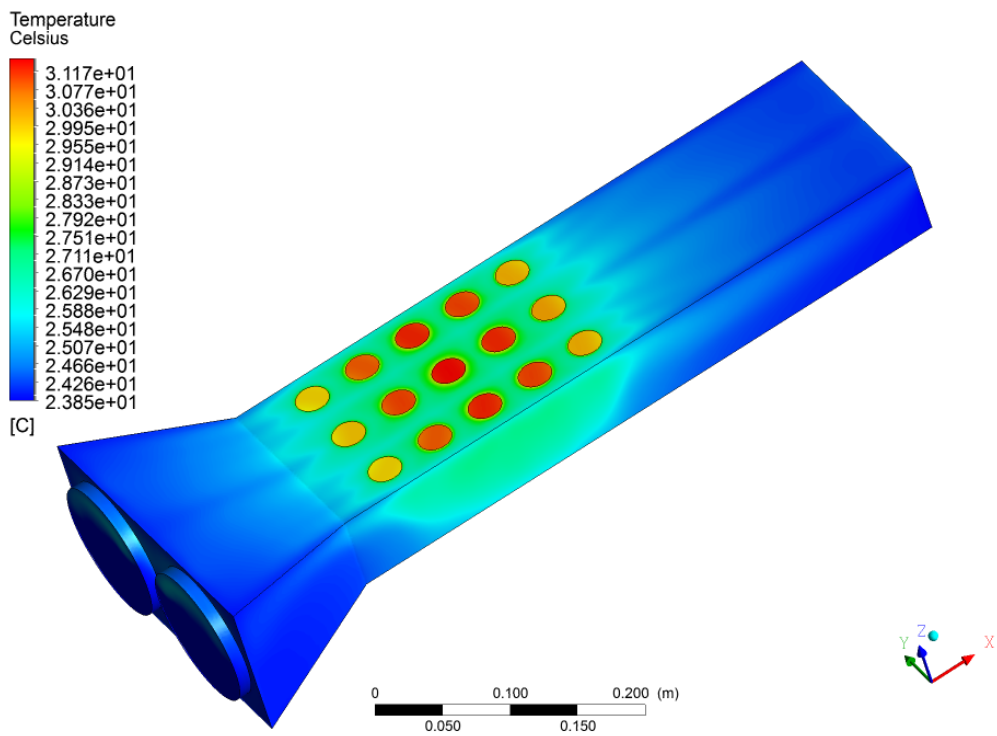
Figure 3.7: Temperature distribution of the module at the end of discharging under free convection at 0.5C and $T_{initial} = 24\,°\mathrm{C}$.
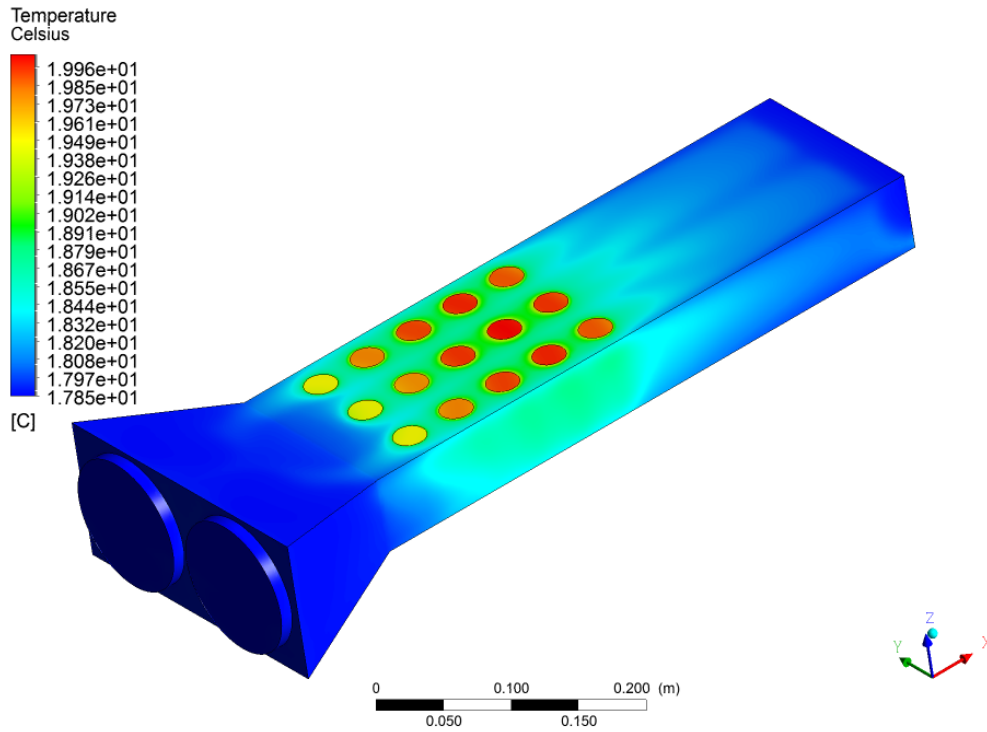
Figure 3.8: Temperature distribution of the module at the end of discharging under free convection at 0.25C and $T_{initial} = 18\,^{\circ}\mathrm{C}$.
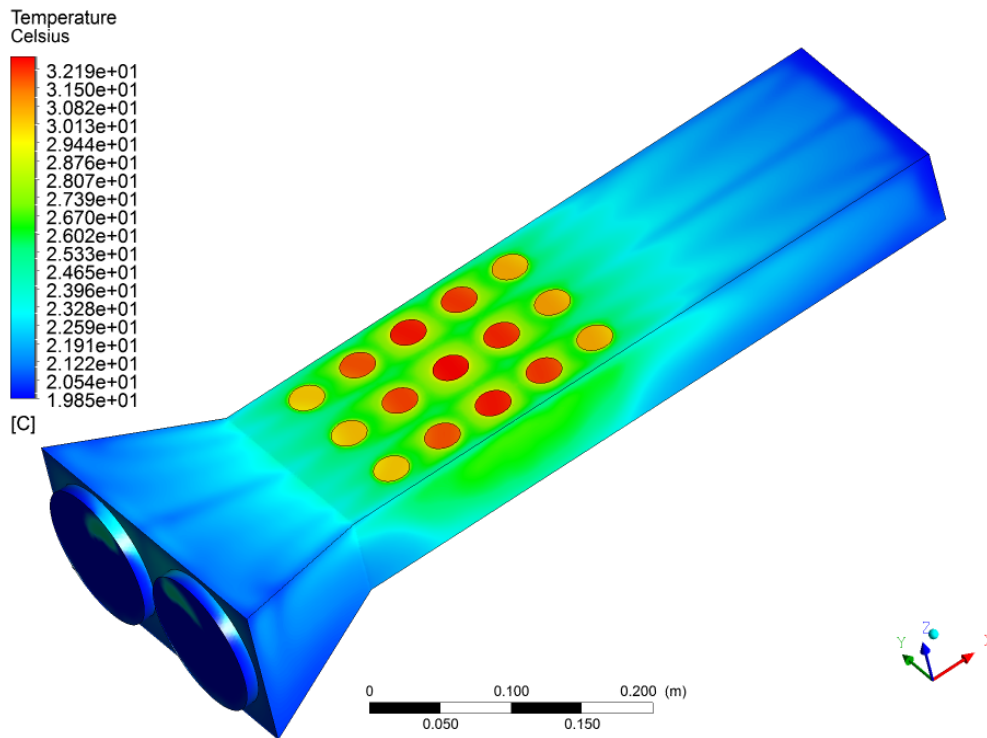
Figure 3.9: Temperature distribution of the module at the end of discharging under free convection at the HWFET-cycle and $T_{initial} = 20\,^{\circ}\mathrm{C}$.

In order to compare the simulated temperature of cells in the module with the experimental data under natural convection, the temperature profile of the central cell of the module (cell number 8) under different discharge rates is depicted in Figure 3.10, which shows that there exists a good agreement between numerical and experimental data.
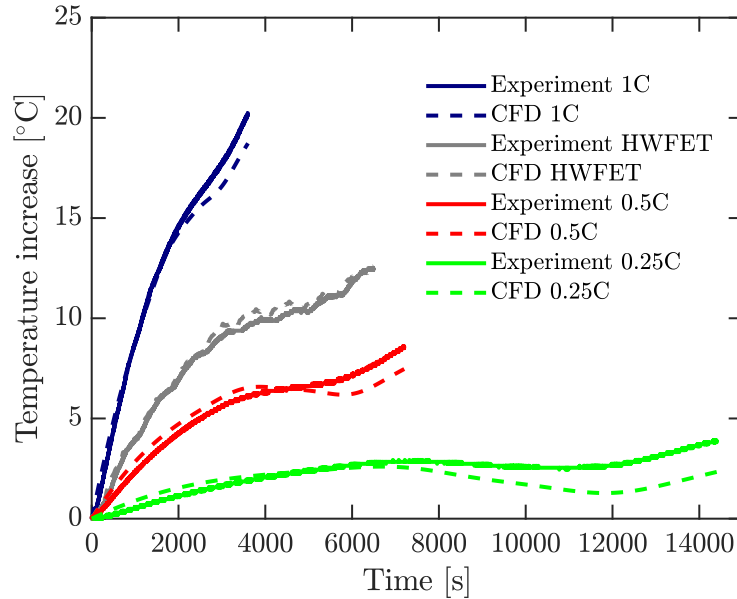
Figure 3.10: Comparison between 3D-CFD model and experimental temperature of the hottest cell (number 8) in the battery module at different discharging rates under free convection.

Figure 3.11 displays the maximum temperature of each cell in the battery module at the end of discharging. In general, temperature increases at a higher discharging rate current. The higher temperature of approximately 44 °C was reached at 1C when the ambient temperature was 24 °C. This cell temperature exceeds the suggested operation temperature of 40 °C [23]. The lowest temperature was about 21 °C at 0.25C when the ambient temperature was 18 °C. The temperature difference among cells in the module is less than 5 °C which is favorable to the useful life of cells [24]. Numerical simulations show that the temperature in the cells tends to be symmetrically distributed.
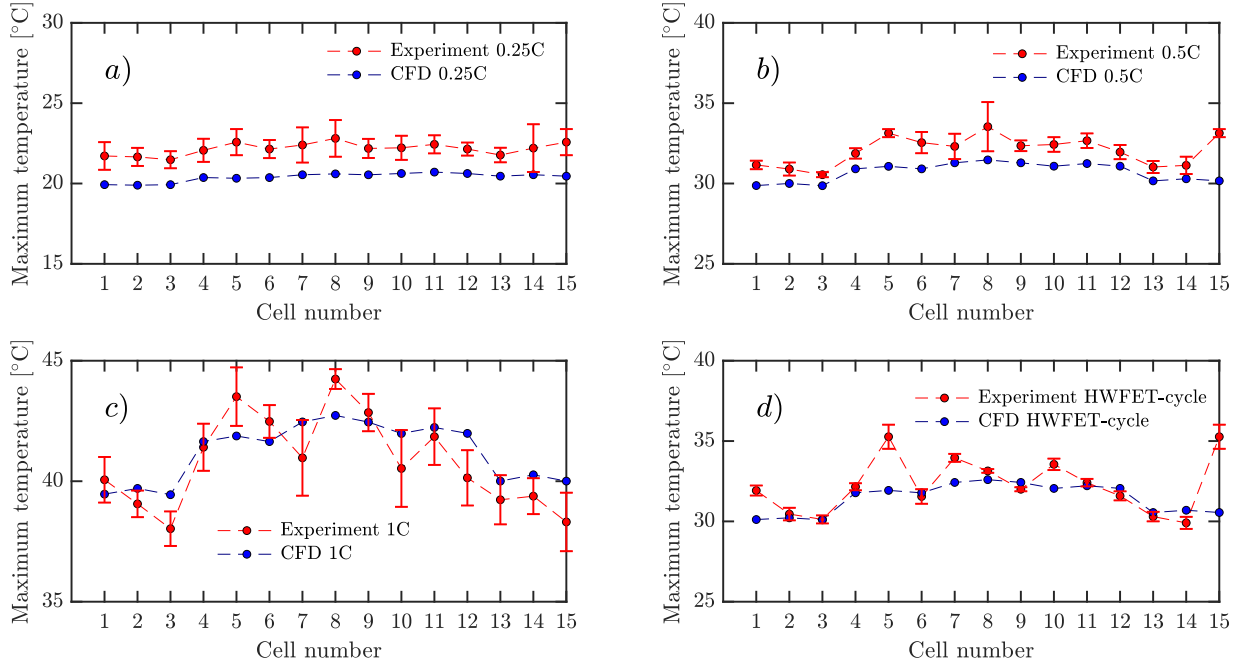
Figure 3.11: Maximum temperature under discharging at free convection. (**a**) 0.25C, $T_{amb} = 18\,°C$. (**b**) 0.5C, $T_{amb} = 24\,°C$. (**c**) 1C, $T_{amb} = 24\,°C$. (**d**) HWFET-cycle, $T_{amb} = 20\,°C$.

The RMS error between experimental and numerical data for each cell in the battery module is listed in Table 3.5. This error is given for all the discharging period. The biggest RMS error ($2.24\,°C$) was found for the cell number 12 at 1C rate while the smallest error ($0.32\,°C$) was for the cell number 8 discharged under the HWFET-driving cycle. These differences are mainly due to electrical connections and quality of cells.

Table 3.5: RMS error between experimental and CFD data under discharging at different current rates. Units °C.

Cell Number	1C	0.5C	0.25C	HWFET
1	0.42	0.51	0.84	0.55
2	1.37	0.58	0.79	0.68
3	1.98	0.72	0.64	0.92
4	0.99	0.53	0.82	0.55
5	0.60	0.69	0.96	0.69
6	0.43	0.83	0.79	1.02
7	2.02	0.58	0.83	0.65
8	0.69	0.67	0.82	0.32
9	0.80	0.59	0.72	1.04
10	1.88	0.60	0.66	0.82
11	1.27	0.53	0.79	0.56
12	2.24	0.66	0.77	1.23
13	1.23	0.54	0.65	0.84
14	1.69	0.44	0.65	1.63
15	2.04	0.45	0.71	1.89

3.2.2 Cooling-down by forced convection

After finishing the discharge process, forced convection was applied. This phenomenon was modeled using the standard $k-\varepsilon$ model under two speeds: 1.5 m/s and 2.7 m/s. Figures 3.12 and 3.13 display their respective streamlines. Simulations show that a wake is developed downstream in the flow separation region. The maximum local air velocity is about 7 m/s when air inlet speed in the tubes was 1.5 m/s and the flow tend to be uniform (Figure 3.12). On the other hand, when the inlet velocity in the tubes was 2.7 m/s, the maximum local airflow speed was approximately 13 m/s and turbulent flow regions are observed (Figure 3.13). It is noticed that the velocity field between two adjacent cells in the direction of the flow in the battery module tend to be zero due to the aligned configuration of the battery module (see Figure 3.12). This behavior was also reported in [108]. Moreover, when the flow is less turbulent, velocity field in that zone (between two adjacent cells) tends to increase. The thermal behavior of cells under forced convection are presented with more detail in section 3.3 to compare it with the temperature prediction based on particle filter.

The thermal behavior of a battery module with fifteen cylindrical LCO cells was evaluated. Discharging current was performed at free convection while forced convection was applied for cooling-down process. During discharging, the temperature of cells rises as discharging current increases. Furthermore, the central zone of the battery module reach the highest temperature at the end of discharging. Measurements of the temperature profile of cells are in good agreement with numerical simulations. Heat generation in each cell is one of the most important parameters to take into account to perform the simulations. Aging effect of cells was not considered.

Figure 3.12: Velocity field at 1.5 m/s in the tubes.

Figure 3.13: Velocity field at 2.7 m/s in the tubes.
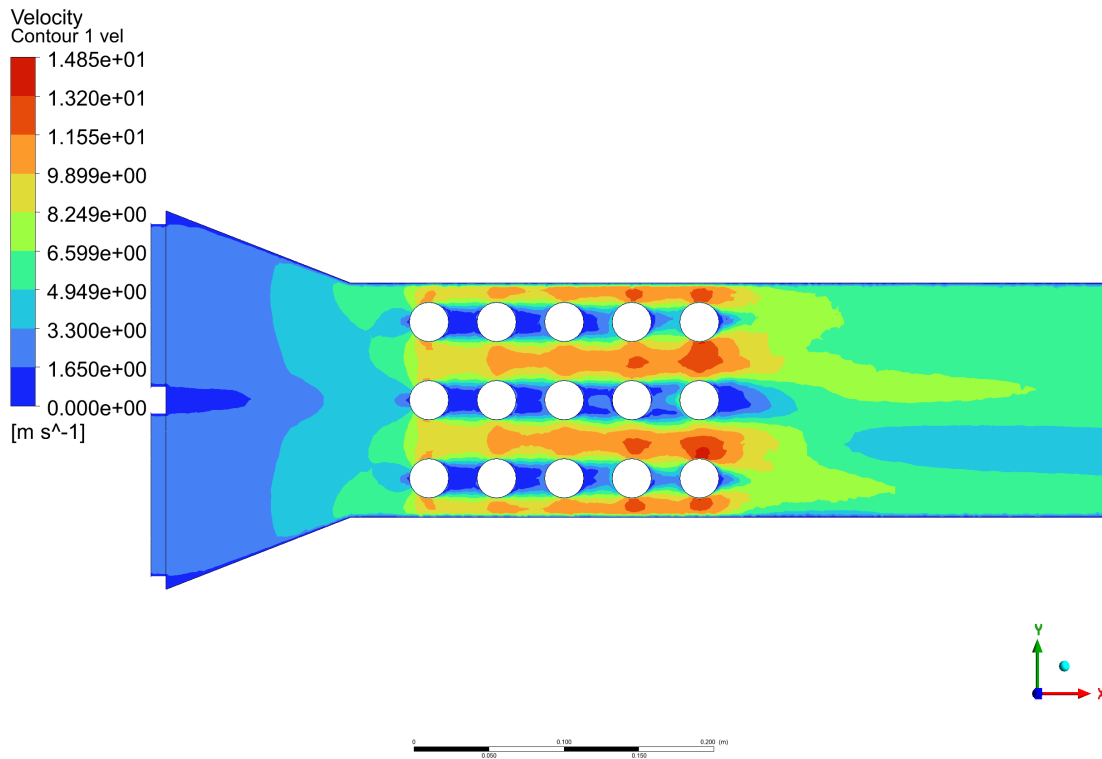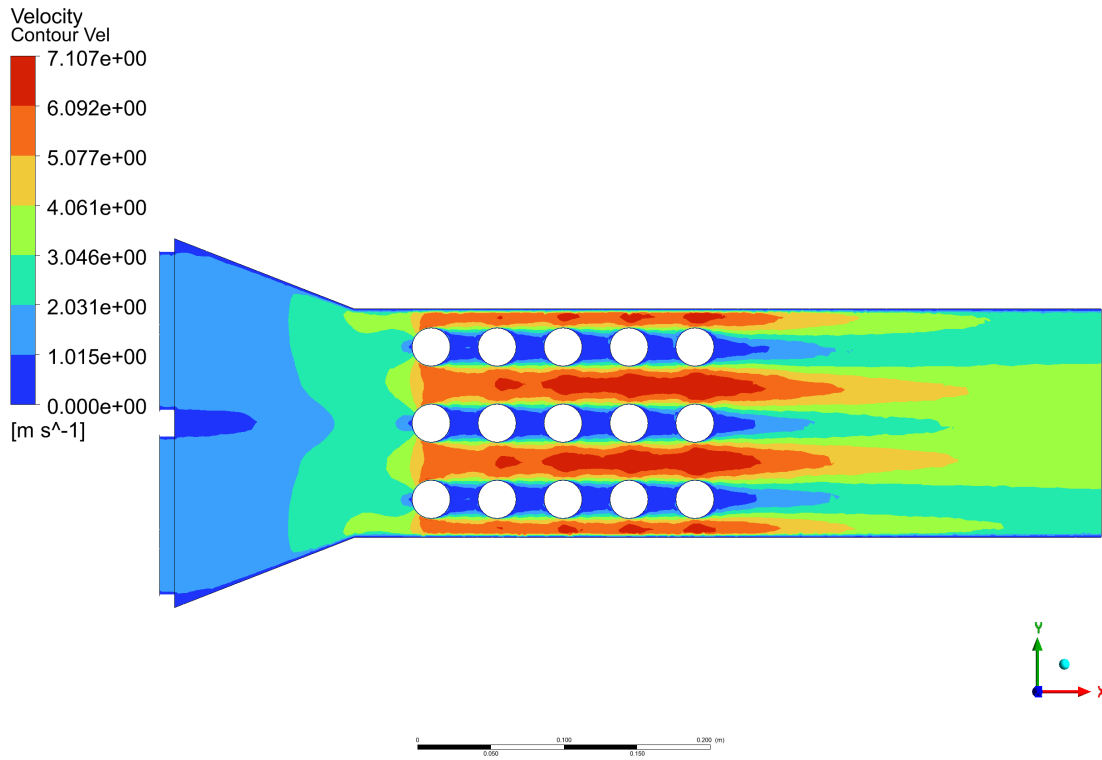
3.3 Results of temperature estimation of the battery module using particle filter

The temperature of each string of five cells in the module was estimated independently during discharging and at cooling-down (when discharging finished).

3.3.1 Particle filter applied during the discharging process

The battery module was completely discharged at 1C. During the first 1800 s, the module underwent natural convection, and after 1800 s, the module was cooled by forced convection. Two velocities were applied independently: 1.5 and 2.7 m/s (speed measurements were taken in the PVC tubes). One example of the temperature profile of cells is depicted in Figure 3.14. It can be observed that under discharging at natural convection (during the first 1800 s), a maximum temperature of about 40 °C was reached for the cell located in the central zone of the module (cell number 8). Moreover, cells number 12 and 14 do not reach the same temperature due to the boundary conditions. Then, cooling-down was applied by air forced convection and the temperature of cells fell without reach to the ambient temperature.
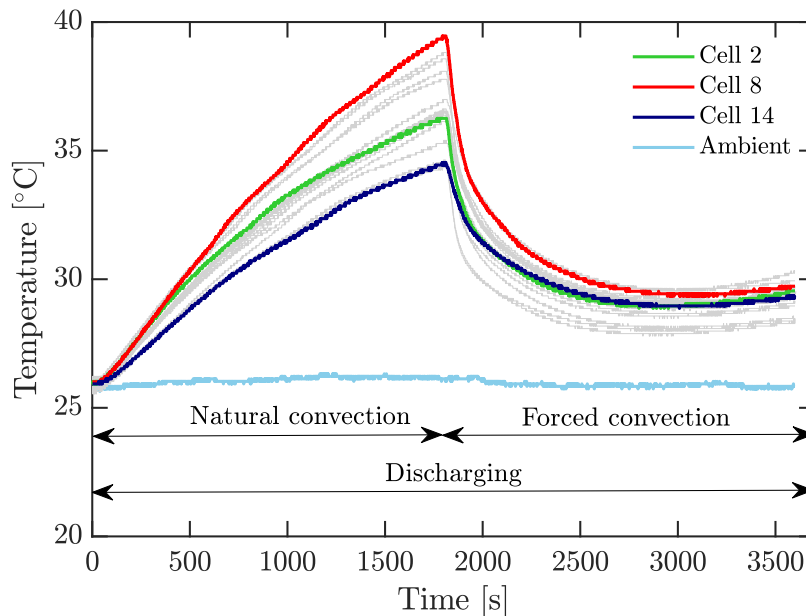
Figure 3.14: Experimental temperature profile of cells under discharging: 1800 s at natural convection and 1800 s at forced convection (air flow speed 1.5 m/s).

Particle filter was implemented for the forced convection stage. Figure 3.15 shows a comparison of thermal performance of cells and parameters during discharging for the string 2 under forced convection at 1.5 m/s. For PF, cell number 2 is taken as observation and the temperature of other cells was estimated. There exist a good agreement among experimental, filtered and CFD simulations of temperature. Moreover, PF estimate the evolution of stretching factor α and thermal time constant τ. These two parameters tent to decrease starting from their initial condition. When air flow speed was 2.7 m/s, there is a similar behavior of parameters as Figure 3.16 shown.

Figure 3.15: Evolution of parameters and temperature estimation by particle filter under 1C discharging rate and 1.5 m/s. Ambient temperature 26 °C.

Figure 3.16: Evolution of parameters and temperature estimation by particle filter under 1C discharging rate and 2.7 m/s. Ambient temperature 26 °C.

Table 3.6 shows the RMS temperature error between experimental and estimated temperature by PF and CFD at two air speed rates. In general, RMS error given by CFD is slightly minor than RSM error obtained by PF. Nevertheless, the estimation of temperature by PF is quite good and take less than one minute while CFD simulations takes many hours. Another advantage of PF is that it can be implemented in real-time applications.

Table 3.6: RMS error between experimental temperature and estimation by particle filtering and CFD during during discharging at 1C-rate. Units °C.

Cell Number	Particle filtering		CFD	
	V 1.5 m/s	V 2.7 m/s	V 1.5 m/s	V 2.7 m/s
1	0.16	0.12	0.29	0.71
2	0.11	0.19	0.88	0.34
3	0.20	0.19	0.33	0.45
4	0.78	0.64	0.30	0.61
5	0.49	0.66	0.53	0.22
6	0.78	0.49	0.24	0.26
7	0.73	0.57	0.36	0.78
8	0.51	0.51	0.46	0.26
9	0.84	0.66	0.29	0.36
10	1.57	0.14	0.31	1.11
11	0.42	0.49	0.60	0.60
12	0.57	0.41	0.32	0.70
13	0.67	0.21	0.20	1.45
14	0.29	1.43	0.70	0.88
15	0.54	0.30	0.23	0.96

3.3.2   Particle filter applied at cooling-down

In this experiment, the battery module with fifteen-cells was discharged under free convection at 0.25C, 0.5C and 1C, and particle filter was applied to estimate the temperature of each cell during the cooling-down process under forced convection (see Figure 3.17). Two speeds were applied to the air flow: 1.5 m/s and 2.7 m/s.

Figures 3.18 and 3.19 display the behavior of cells after discharging them at 0.5C, and cooling-down under 1.5 m/s and 2.7 m/s, respectively. At the air flow speed of 1.5 m/s, the temperature estimated by particle filter and CFD are better than at 2.7 m/s. Nevertheless, in this last case (2.7 m/s), CFD computations show an improvement with respect to filtered temperature. For the rest of the cases, i.e., cell temperature estimations after 0.5C (Figures 3.20 and 3.21) and 1C (Figures 3.22 and 3.23), the cells temperature given by particle filtering and CFD are almost the same and they are in good agreement with experimental data. In the majority of the aforementioned cases, the evolution of parameters α and τ given by PF tend to be decreasing starting from their respective initial value.
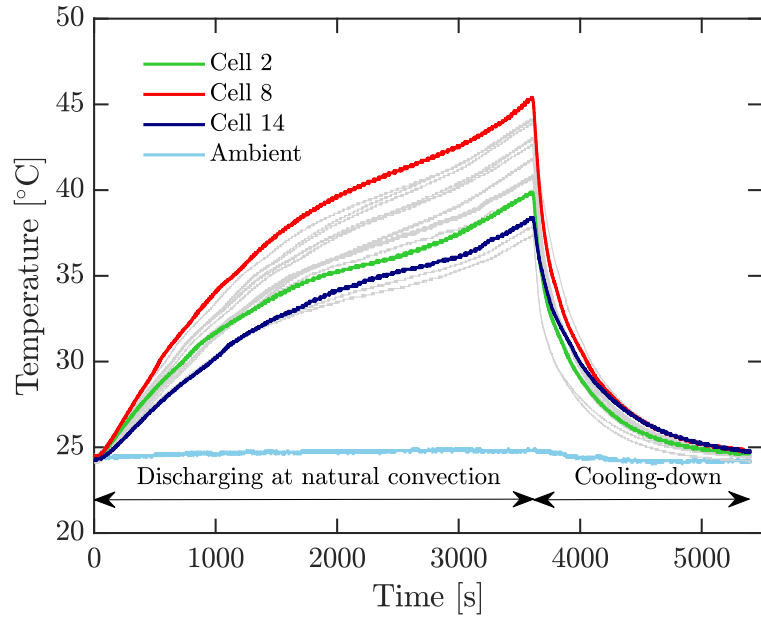
Figure 3.17: Experimental temperature profile of cells discharged at 1C under natural convection and then cooled-down by forced convection (air speed 1.5 m/s).
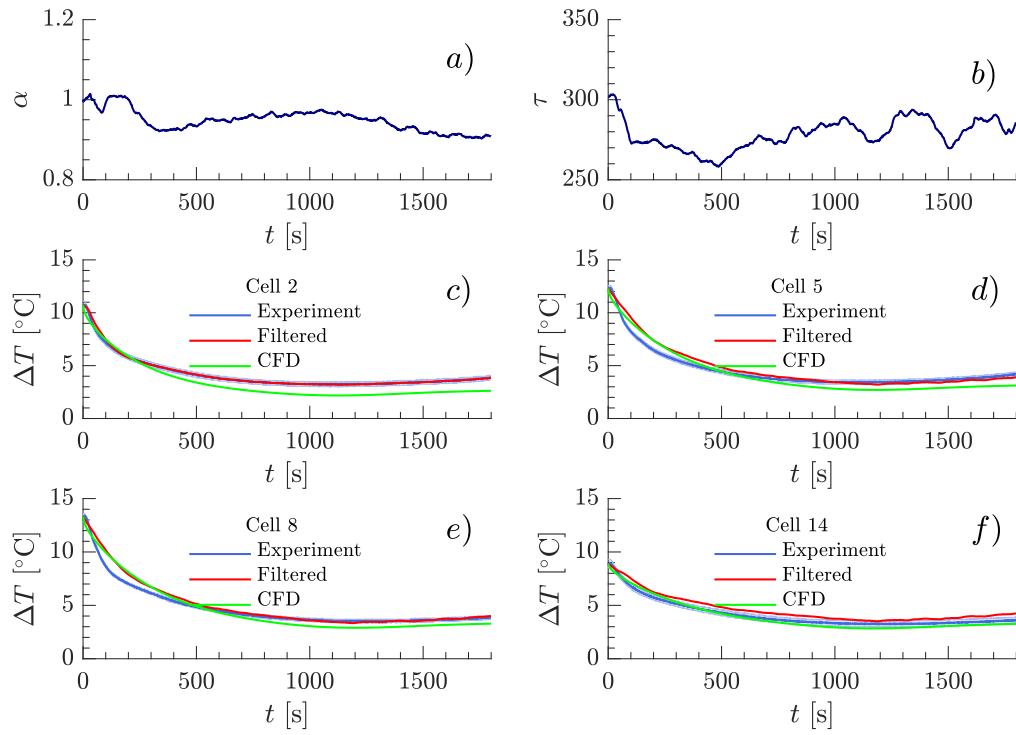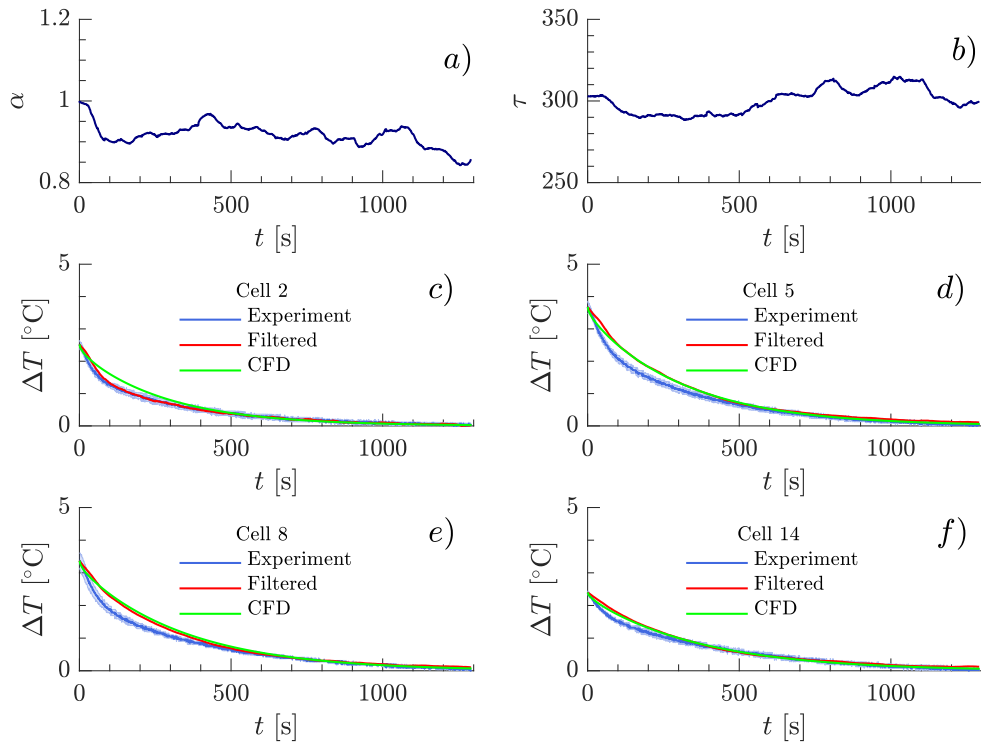

Figure 3.18: Evolution of parameters and temperature estimation by particle filter under 0.25C discharging rate and 1.5 m/s. Ambient temperature 26 °C.
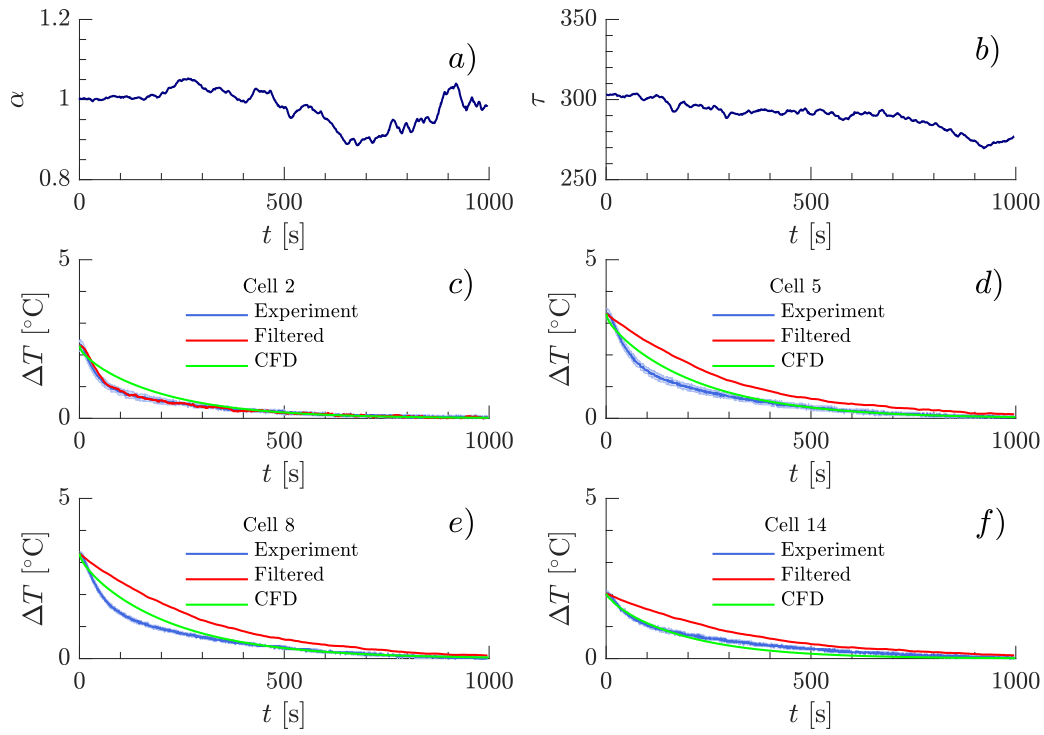
Figure 3.19: Evolution of parameters and temperature estimation by particle filter under 0.25C discharging rate and 2.7 m/s. Ambient temperature 26 °C.
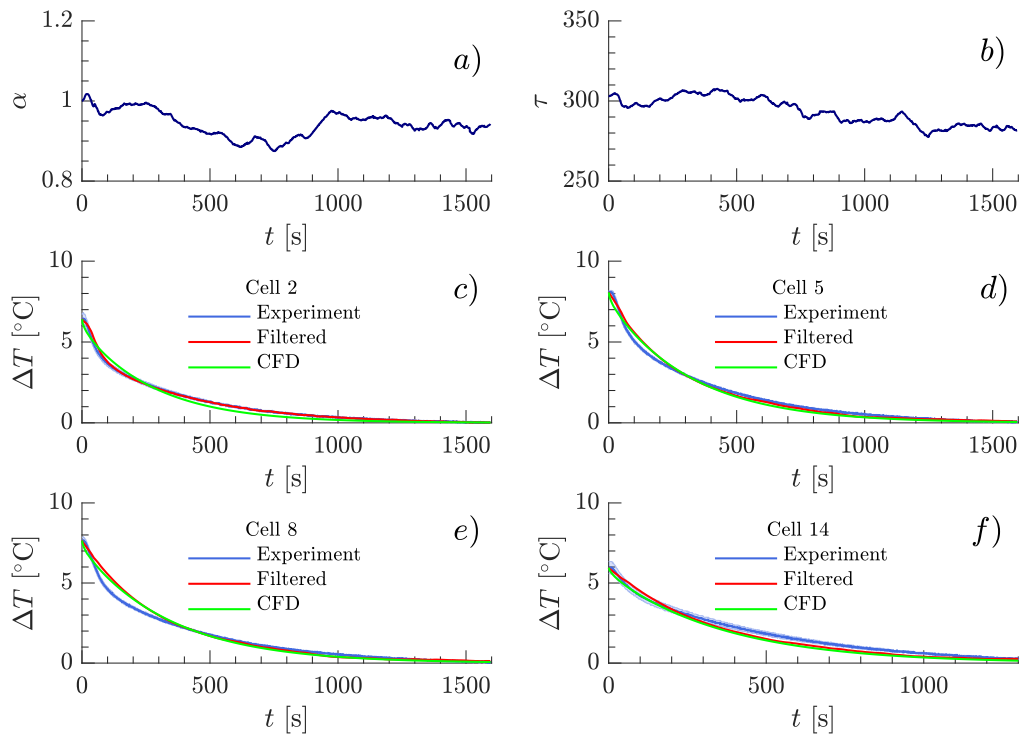
Figure 3.20: Evolution of parameters and temperature estimation by particle filter under 0.5C discharging rate and 1.5 m/s. Ambient temperature 25 °C.
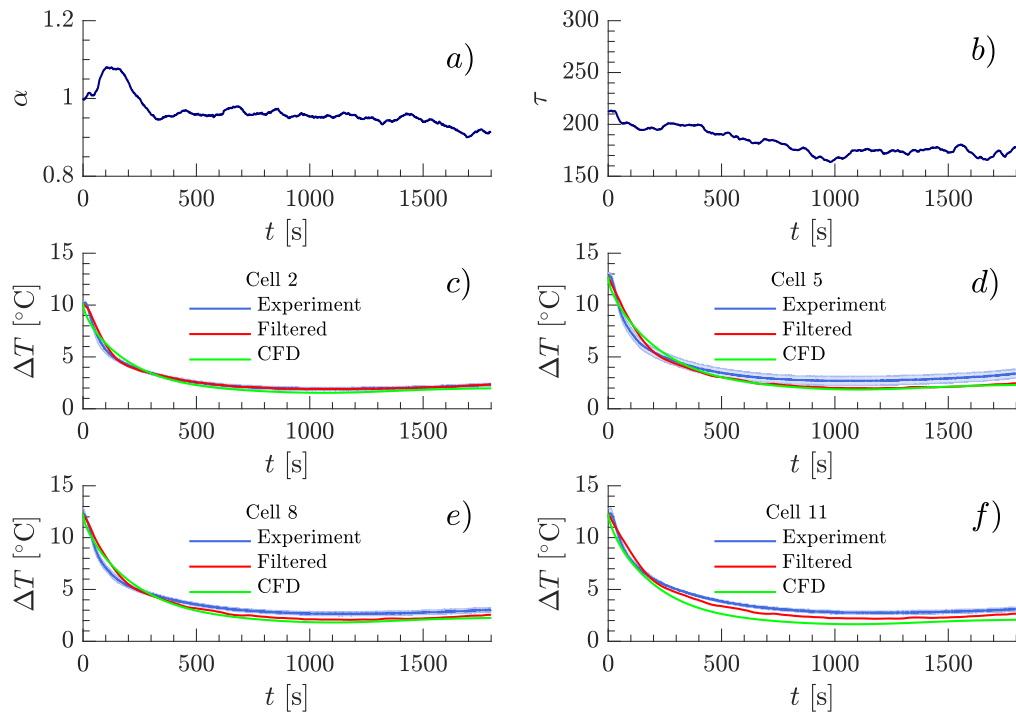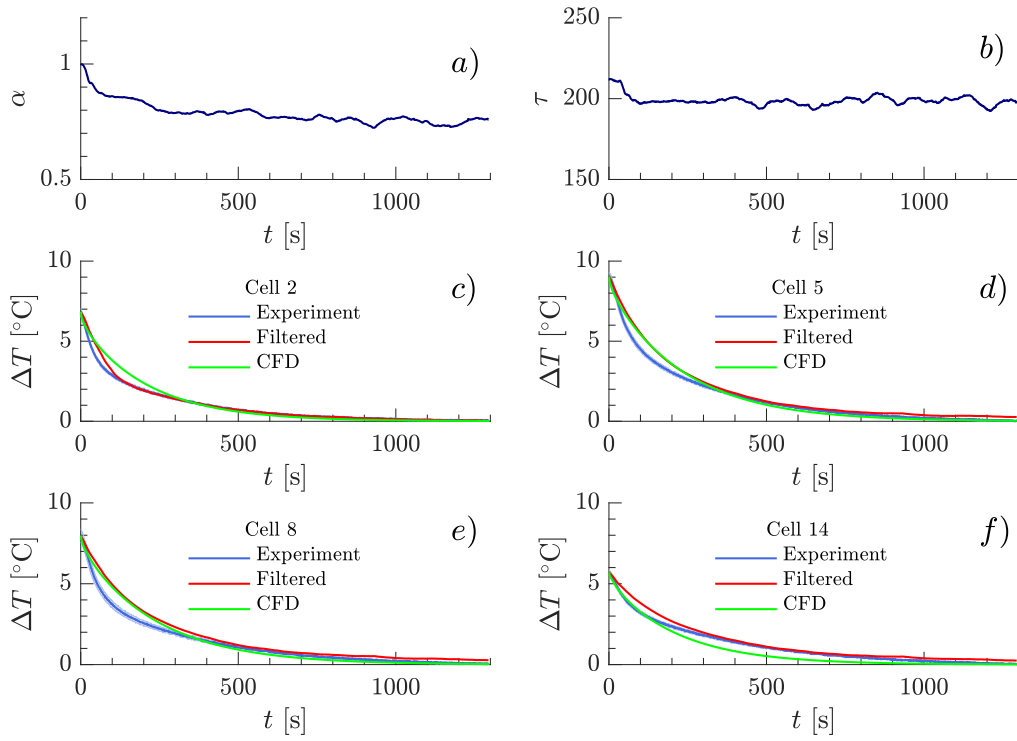
Figure 3.21: Evolution of parameters and temperature estimation by particle filter under 0.5C discharging rate and 2.7 m/s. Ambient temperature 25 °C.
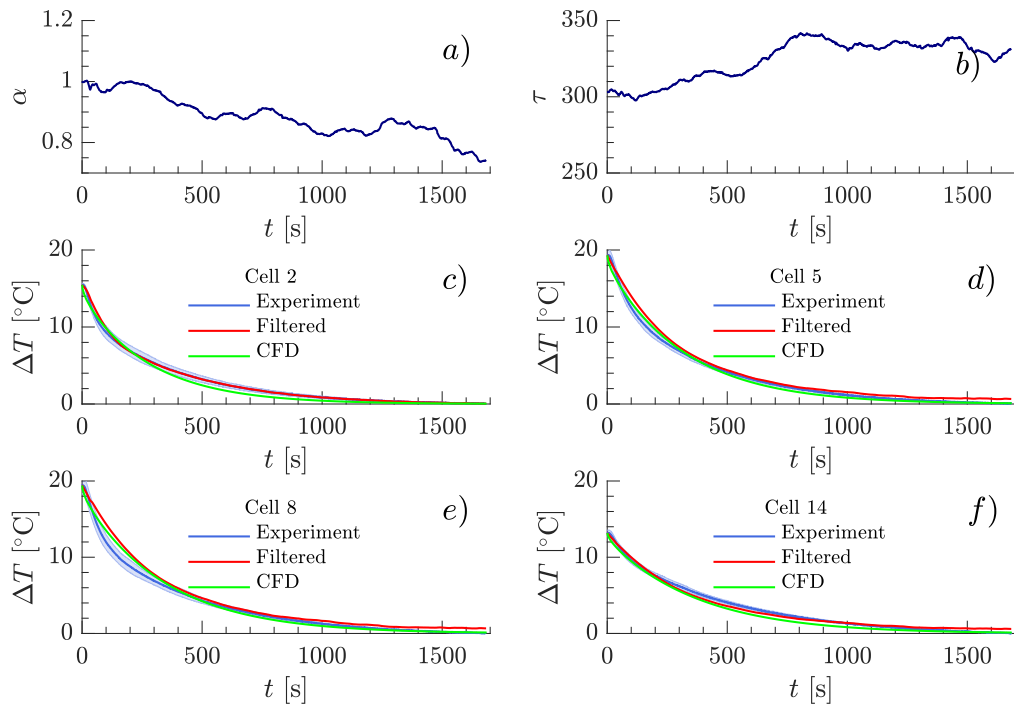
Figure 3.22: Evolution of parameters and temperature estimation by particle filter under 1C discharging rate and 1.5 m/s. Ambient temperature 26 °C.
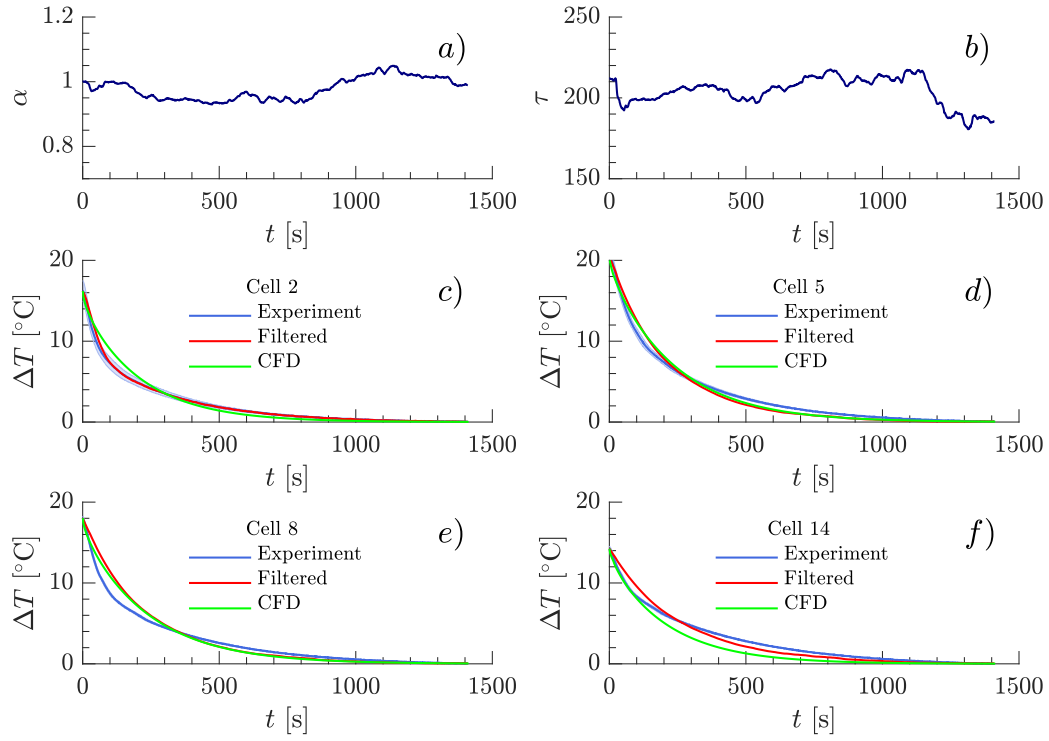
Figure 3.23: Evolution of parameters and temperature estimation by particle filter under 1C discharging rate and 2.7 m/s. Ambient temperature 26 °C.

In order to present a more detailed comparison between experimental temperature and temperature given by particle filter and CFD, RMS error for temperature after discharging at 0.25C (Table 3.7), 0.5C (Table 3.8) and 1C (Table 3.9) was computed. In general, RMS error increases when current discharging rate increases as well. The smaller RMS error was for cells number 1 and 2 at 0.25C and 2.7 m/s air flow while the higher RMS error was for the cell number 9 at 1C and 2.7 m/s air flow rate. In most cases, by increasing the air flow speed, the RMS error slightly increases. Moreover, RMS error given by CFD computation is slightly smaller than PF estimation. Nonetheless, CFD takes many hours to perform simulations and PF takes a few seconds. Another great advantage of PF is that this method can be employed for real-time monitoring of the battery pack temperature.

Table 3.7: RMS error of temperature estimation by particle filtering and CFD under cooling-down after 0.25C discharging rate. Units °C.

Cell Number	Particle filtering		CFD	
	V 1.5 m/s	V 2.7 m/s	V 1.5 m/s	V 2.7 m/s
1	0.11	0.04	0.18	0.14
2	0.05	0.04	0.10	0.15
3	0.04	0.04	0.11	0.17
4	0.29	0.51	0.08	0.27
5	0.20	0.45	0.06	0.32
6	0.26	0.46	0.07	0.25
7	0.24	0.57	0.05	0.37
8	0.18	0.47	0.06	0.32
9	0.30	0.49	0.08	0.30
10	0.10	0.28	0.09	0.39
11	0.21	0.42	0.06	0.40
12	0.24	0.43	0.08	0.43
13	0.14	0.32	0.07	0.36
14	0.12	0.25	0.05	0.32
15	0.17	0.31	0.06	0.31

Table 3.8: RMS error of temperature estimation by particle filtering and CFD under cooling-down after 0.5C discharging rate. Units °C.

Cell Number	Particle filtering		CFD	
	V 1.5 m/s	V 2.7 m/s	V 1.5 m/s	V 2.7 m/s
1	0.06	0.11	0.25	0.19
2	0.07	0.17	0.20	0.23
3	0.08	0.07	0.23	0.29
4	0.39	0.56	0.12	0.11
5	0.18	0.35	0.11	0.24
6	0.33	0.54	0.11	0.15
7	0.37	0.66	0.10	0.23
8	0.29	0.46	0.10	0.28
9	0.34	0.65	0.09	0.19
10	0.11	0.13	0.11	0.32
11	0.23	0.44	0.12	0.44
12	0.24	0.47	0.08	0.27
13	0.12	0.26	0.11	0.43
14	0.20	0.24	0.13	0.50
15	0.10	0.31	0.06	0.33

Table 3.9: RMS error of temperature estimation by particle filtering and CFD under cooling-down after 1C discharging rate. Units °C.

Cell Number	Particle filtering		CFD	
	V 1.5 m/s	V 2.7 m/s	V 1.5 m/s	V 2.7 m/s
1	0.49	0.30	0.63	0.40
2	0.19	0.19	0.51	0.52
3	0.25	0.21	0.46	0.57
4	0.97	1.13	0.43	0.26
5	0.70	0.59	0.73	0.26
6	0.80	1.16	0.47	0.46
7	0.76	1.13	0.32	0.44
8	0.80	0.86	0.56	0.27
9	1.08	1.47	0.55	0.72
10	0.51	0.39	0.39	0.68
11	0.58	0.79	0.54	0.65
12	0.57	1.10	0.40	1.09
13	0.26	0.50	0.43	1.01
14	0.20	0.51	0.48	0.82
15	0.38	0.67	0.39	0.67

PF was applied to estimate seven states during the cooling-down process in a Li-ion battery module: fives states represent the temperature of the cells and two states correspond to a stretching factor and a thermal time constant. In most cases, α decays from 1 to around 0.8 and τ oscillates from 300 s^{-1} to approximately 200 s^{-1}. Moreover, RMS errors increase as discharging rate increases. CFD computations slightly improves the temperature estimation of cells. For example, for the cell number 8 cooled at 2.7 m/s, RMS error decays from 0.47 °C to 0.32 °C at 0.25C, also is reduced from 0.46 °C to 0.28 °C at 0.5C, and from 0.86 °C to 0.27 °C at 1C. The disadvantage of CFD is that this approach takes many hours to simulate the cooling-down process of the cells while the execution of PF algorithm takes a few seconds.

PF was developed to estimate the cell temperature at forced convection while natural convection case could be studied as a future work. It was concluded that PF estimates well the temperature of cells and it can be implemented in online monitoring.

3.4 Results of thermal stability study of a lithium-ion battery

Thermal stability of LIBs is crucial for safety of electric devices and people because at high temperatures or under abuse conditions the cell can explode. The interaction between heat transfer processes and heat generation determines the thermal state of the cell, and the occurrence of thermal runaway (TR) [60]. In this section, the thermal behavior of a 26650 LCO cell under thermal abuse is modeled. A non-dimensional approach is also developed to evaluate thermal runaway conditions.

3.4.1 Characterization of thermal runaway of a single cell by thermal abuse model

Thermal runaway by oven test was modeled solving Eq. 2.32 coupled with the system of Eqs. (2.25-2.29). A numerical simulation was implemented using an adaptive algorithm (ode 15s) in MATLAB that sorts out stiff differential equations. Parameters of the model are detailed in Table 2.11. Firstly, according to Figure 3.24a, natural convection is considered assuming $h_{conv} = 7.17$ Wm^{-2}K^{-1} [109]. Results shows that at ambient temperature $T_{amb} = 145\,°C$, TR does not occur, but at $150\,°C$ it does after 62 min approximately. This time is considerably reduced when T_{amb} is $155\,°C$. Secondly, with regard to 3.24b, forced convection is assumed with $h_{conv} = 100$ Wm^{-2}K^{-1}. In this case, TR does not occur until T_{amb} is $170\,°C$, but when it occurs, it does after about 10 min. At time $t = 0$, the temperature of the cell was assumed to be $35\,°C$ for both cases.
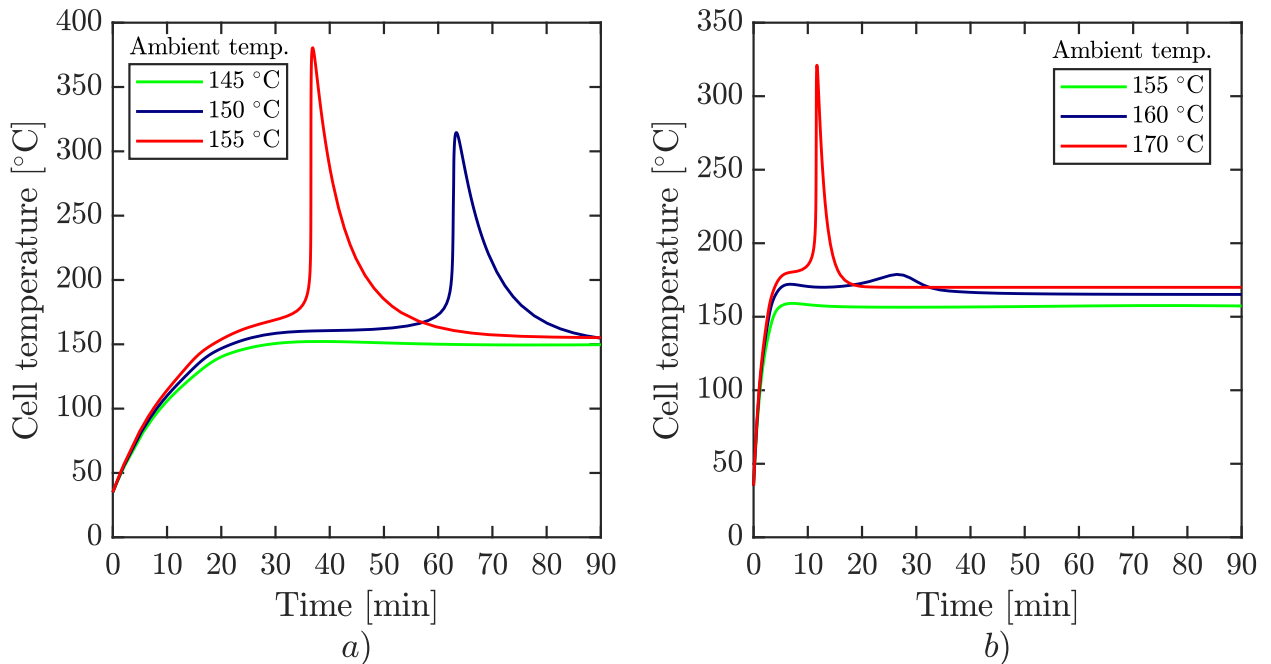
Figure 3.24: Thermal runaway modeling of a 26650 LCO cell at three different ambient temperatures: (**a**) Under natural convection, 7 Wm^{-2}K^{-1}. (**b**) Under forced convection, 100 Wm^{-2}K^{-1}.

In [110], the author found that a heating rate more than 17 °C/min provokes a violent thermal runaway reaction in a cylindrical LCO cell. In this way, thermal runaway time (t_{TR}) is assumed when the thermal reaction reaches this heating rate threshold. Figure 3.25 reveals that t_{TR} modeled for a 26650 LCO cell increases as both ambient temperature and convective coefficient decrease. As described earlier in Figure 3.24a, under natural convection and considering the properties and initial conditions given in Table 2.11, TR does not occur below 145 °C.
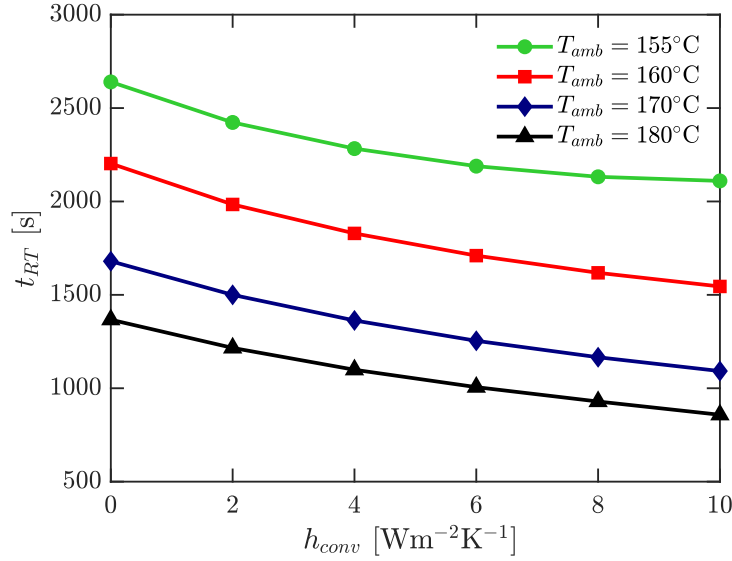
Figure 3.25: Thermal runaway time t_{TR} simulation for a 26650 LCO cell

3.4.2 Qualitative stability analysis

Solutions when Eq. 2.38 is equal to zero are represented in the following plots. The goal is to find fixed points, specially the unstable ones.

First, recalling the dimensionless Eq. 2.38 to evaluate the thermal runaway occurrence of a cell:

$$\frac{\mathrm{d}T^*}{\mathrm{d}t^*} = \alpha + \exp\left(-\frac{1}{T^*}\right) - \beta T^* - \gamma T^{*4},$$
$$= f\left(T^*\right),$$

where α, β and γ mainly represent the effect of heat generation, convection, and radiation, respectively on the cell.

Figure 3.26 shows the phase portrait of $f(T^*)$ for two values of the parameter α. For $\alpha = 0.1$ (Figure 3.26a) there exist two fixed points (when $f(T^*) = 0$) named A and B which are stable points. When $\alpha = 0.01$ (Figure 3.26b), there exist also two fixed points named C and D, which are unstable and stable points, respectively. The point C represents the conditions that cause the battery to undergo thermal runaway and it is given for $\beta = 0.2$. Moreover, considering that 2.38 represents a one-dimensional or first-order system, points A, B and D are attractors (or sinks) while point C is a repeller (or source).
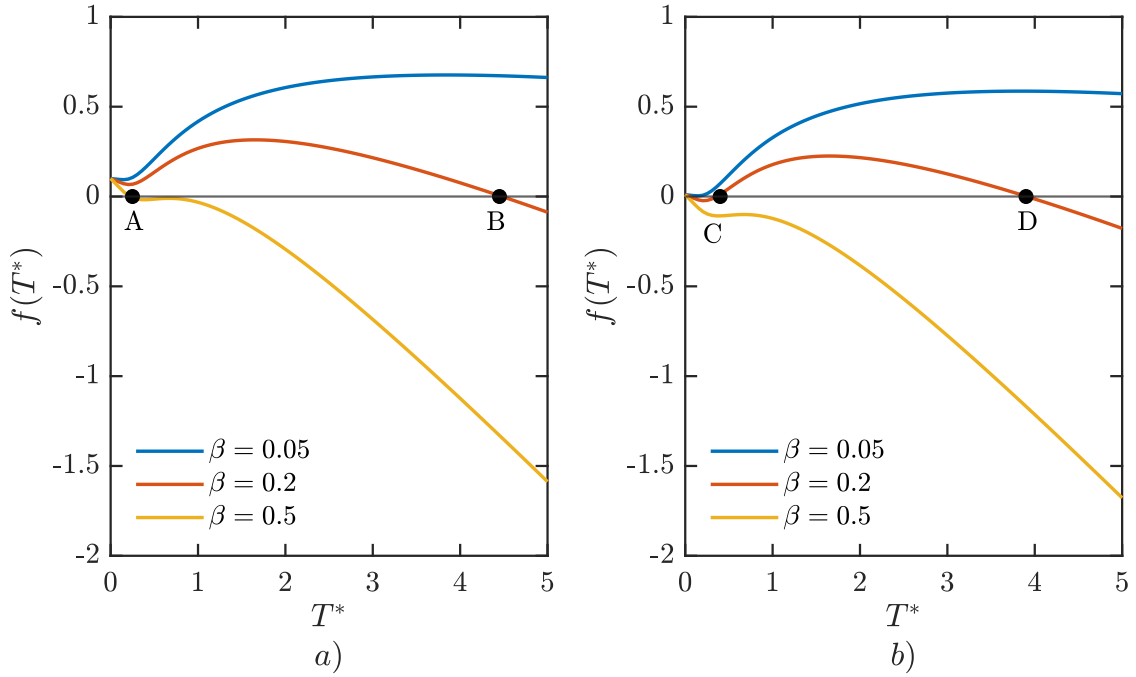
Figure 3.26: Evaluation of $f(T^*)$ for $\gamma = 10^{-5}$. (**a**) With $\alpha = 0.1$. (**b**) With $\alpha = 0.01$.
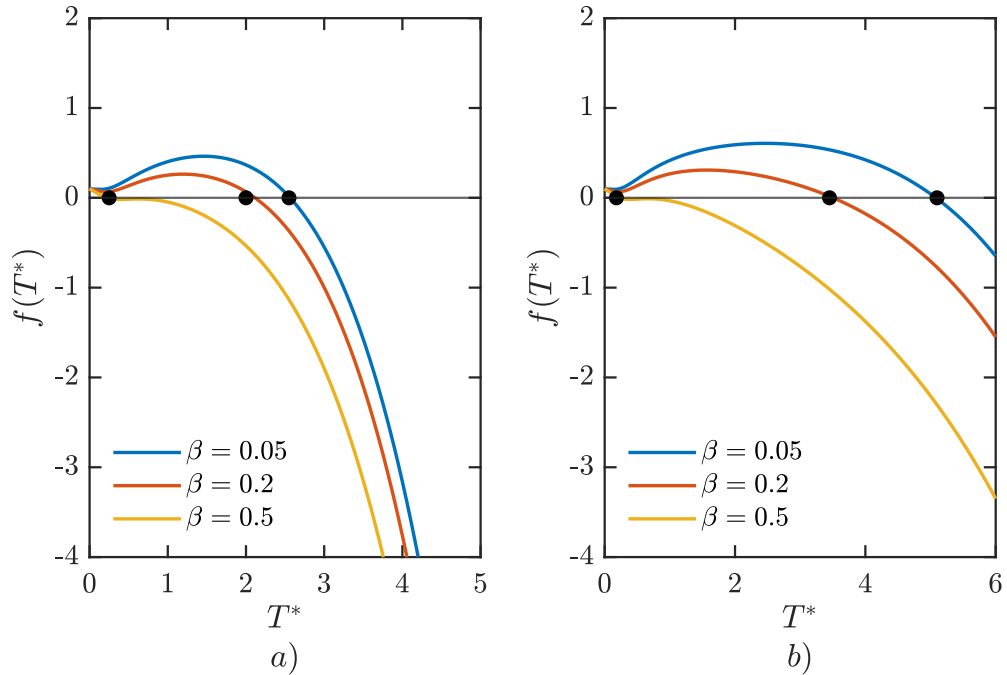
Figure 3.27: Evaluation of $f(T^*)$ for $\alpha = 0.1$. (**a**) With $\gamma = 0.015$. (**b**) With $\gamma = 0.001$.

Another scenario is evaluated by varying the parameter γ. Figure 3.27a and Fig 3.27b display the behavior of $f(T^*)$ for $\gamma = 0.015$ and $\gamma = 0.001$, respectively. In both cases there exist only stable fixed points (attractors or sinks) which do not cause thermal runaway. This behavior means that the radiation can be important factor but it is not a critical parameter to consider in terms of the thermal runaway occurrence.

71

Solutions for steady state when $f(T^*) = 0$ are presented in Figure 3.28. For low values of β, T^* takes values near to 1 and when β increases, T^* tends to decrease.
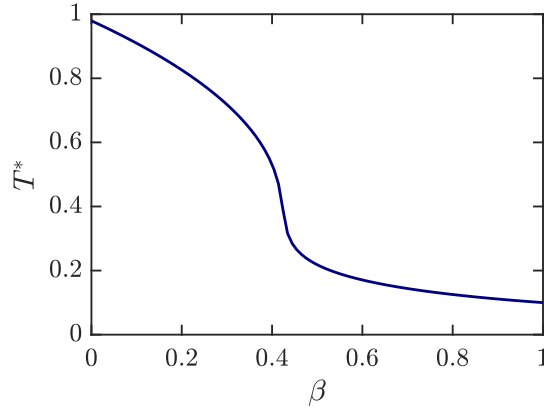
Figure 3.28: Dimensionless temperature T^* when $f(T^*) = 0$ under different values of β with $\alpha = 0.1$ and $\gamma = 0.5$.

Mechanisms to prevent thermal runaway in Li-ion batteries should be focused on the cooling system. Moreover, ambient temperature and heat generation rate are crucial parameters that also should be controlled.

Thermal runaway is caused by many factors. In this case we studied the thermal abuse model which takes into consideration the heat reaction that take place in the distinct components of the battery. In general terms, TR occurs when the rate of heat generation in the cell is greater than the released heat. Onset temperature of TR mainly depends on the type of cell, ambient temperature and cooling mechanism. Dimensionless parameters that take into account those factors were described.

Conclusions

Concluding remarks

The temperature profile of a LCO 26650 lithium-ion battery module was evaluated. Thermal performance of a Li-ion battery is mainly influenced by the discharging current, heat generation rate, and cooling mechanism. First, there were compared three of the most used methods to study the thermal behavior of LIBs: a lumped model, 3D-CFD approach and an electrochemical method based on NTGK with dual potential approach.

In general, NTGK model has the best performance over the rest of the studied models due to that it is capable to solve temperature, voltage, heat generation and other properties. This approach provides the lower temperature error at rates of 0.5C and 1C. Nevertheless, this model presents the higher RMS error at 1.5C, where the maximum temperature increase of the cell was 18.1 °C.

Lumped model is suitable to be used satisfactorily in a wide range of LIB operating conditions and it presents a very similar temperature profile as 3D formulation since both models depend on the same heat generation rate and thermal parameters.

A 3D formulation was used to evaluate the thermal performance of a battery module. It was observed that the temperature rises as the current increases and the central zone of the module reached the higher temperature at the end of the discharging process.

A bayesian approach named particle filter was applied in a Li-ion battery pack under air forced convection. PF predicts well the temperature of cells and it can be implemented in online monitoring. PF also performs the artificial evolution of two parameters in the model: a fractal time parameter and a thermal time constant. Applying CFD computations slightly improves the temperature estimation of cells, but this approach takes many hours of simulation.

Thermal runaway in a Li-ion battery was studied using a non-linear the thermal abuse model. In general, thermal runaway occurs when the heat generation rate in the cell is greater than the rate of heat transfer between the cell and the environment. Dimensionless parameters were described and the main factors that cause TR are the type of cell, ambient temperature and cooling mechanism.

Suggestions for future work

This work pave the way for many other contributions that can be done as a future work in the field of thermal management of lithium-ion batteries.

A study about natural convection in a battery pack would be appropriate to extend the comprehension of thermal behavior of Li-ion cells. Numerical simulations can be done for many cell configurations in a bank varying geometric characteristics and initial conditions, Moreover, the impact of Von Karman Vortices on a battery arrangement could be analyzed. Besides, another type of cooling methods such as phase change materials can be used.

Particle filter can be implemented using many others current profiles and flow rates of coolant. It would be interesting to evaluate the particle filtering applying more experiments during the discharging process under different cooling rates and cell arrangements such as staggered configuration of LIBS. It would also be interesting to study a fractional formulation as a process model. Moreover, aging effect on thermal performance of a cell could be studied.

Thermal runaway should be tested in the laboratory using precise equipment such as an accelerating rate calorimeter. This kind of equipment could also be used to determine thermal parameters. Besides, TR stability can be studied triggering it by another type of mechanism such as nail penetration, short-circuit, overdischarge, etc.

Glossary

Charging It is defined as the process when a battery is connected to any source of energy in order to be re-charged.

Depth-of-discharge It represents the percentage of energy extracted from the battery. This is the inverse of SOC (0% of DOD = full charged; 100% of DOD = discharged).

Discharging A process when a battery supplies energy to any load (device) that is connected to the terminals of the battery.

Open circuit voltage It is the voltage between battery terminals without any load connected.

Particle filter It is a technique for implementing a method to estimate hidden process states in real-time by combining the power of Monte Carlo methods with the Bayesian inference.

State-of-charge It is the percentage of energy (Ah) available in a battery (100% of SOC = full charged; 0% of SOC = discharged). SOC plays the role as fuel gauge does in a gasoline-driven automobile.

State-of-health It defines the physical condition of the battery. Generally, this term is linked to the battery aging.

Thermal runaway A chain of exothermic reactions that happen swiftly when a cell undergoes abuse conditions. It may cause explosions and fire.

Bibliography

[1] G. E. Blomgren, "The Development and Future of Lithium Ion Batteries," *Journal of The Electrochemical Society*, vol. 164, no. 1, pp. A5019–A5025, 2017.

[2] G. Qian, B. Zhu, X. Liao, H. Zhai, A. Srinivasan, N. J. Fritz, Q. Cheng, M. Ning, B. Qie, and Y. Li, "Bioinspired , Spine-Like , Flexible , Rechargeable Lithium-Ion Batteries with High Energy Density," *Advances Materials*, vol. 1704947, pp. 1–8, 2018.

[3] T. M. Bandhauer, S. Garimella, and T. F. Fuller, "A Critical Review of Thermal Issues in Lithium-Ion Batteries," *Journal of The Electrochemical Society*, vol. 158, no. 3, p. R1, 2011.

[4] G. Xia, L. Cao, and G. Bi, "A review on battery thermal management in electric vehicle application," *Journal of Power Sources*, vol. 367, pp. 90–105, 2017.

[5] W. Tong, K. Somasundaram, E. Birgersson, A. S. Mujumdar, and C. Yap, "Thermo-electrochemical model for forced convection air cooling of a lithium-ion battery module," *Applied Thermal Engineering*, vol. 99, pp. 672–682, 2016.

[6] X. Hu, S. Lin, S. Stanton, and W. Lian, "A Foster network thermal model for HEV/EV battery modeling," *IEEE Transactions on Industry Applications*, vol. 47, no. 4, pp. 1692–1699, 2011.

[7] N. Tian, H. Fang, and Y. Wang, "3-D Temperature Field Reconstruction for a Lithium-Ion Battery Pack: A Distributed Kalman Filtering Approach," 2017.

[8] T. D. Hatchard, D. D. MacNeil, A. Basu, and J. R. Dahn, "Thermal Model of Cylindrical and Prismatic Lithium-Ion Cells," *Journal of The Electrochemical Society*, vol. 148, no. 7, p. A755, 2001.

[9] G. H. Kim, A. Pesaran, and R. Spotnitz, "A three-dimensional thermal abuse model for lithium-ion cells," *Journal of Power Sources*, vol. 170, no. 2, pp. 476–489, 2007.

[10] J. W. Choi and D. Aurbach, "Promise and reality of post-lithium-ion batteries with high energy densities," *Nature Reviews Materials*, vol. 1, 2016.

[11] S. J. An, J. Li, C. Daniel, D. Mohanty, S. Nagpure, and D. L. Wood, "The state of understanding of the lithium-ion-battery graphite solid electrolyte interphase (SEI) and its relationship to formation cycling," *Carbon*, vol. 105, pp. 52–76, 2016.

[12] M. Farag, H. Sweity, M. Fleckenstein, and S. Habibi, "Combined electrochemical, heat generation, and thermal model for large prismatic lithium-ion batteries in real-time applications," *Journal of Power Sources*, vol. 360, pp. 618–633, 2017.

[13] X. Yuan, H. Liu, and J. Zhang, *Lithium - Ion Batteries: Advanced Materials and Technologies*. Ohio: CRC Press, 2011.

[14] K. Xu, "Nonaqueous Liquid Electrolytes for Lithium-Based Rechargeable Batteries Nonaqueous Liquid Electrolytes for Lithium-Based Rechargeable Batteries," *Chemical Reviews*, vol. 104, no. September, p. 4303, 2004.

[15] J. B. Goodenough and Y. Kim, "Challenges for rechargeable Li batteries," *Chemistry of Materials*, vol. 22, no. 3, pp. 587–603, 2010.

[16] X. Zhang, "Thermal analysis of a cylindrical lithium-ion battery," *Electrochimica Acta*, vol. 56, no. 3, pp. 1246–1255, 2011.

[17] S. Santhanagopalan, K. Smith, J. Neubauer, G. H. Kim, M. Keyser, and A. Pesaran, *Design and analysis of large lithium-ion battery systems*. Boston: Artech House, 2015.

[18] J. Jiang and C. Zhang, *Fundamentals and Applications of Lithium-Ion Batteries in Electric Drive Vehicles*. Pondicherry: John Wiley & Sons Singapore Pte. Ltd., 2015.

[19] L. H. Saw, Y. Ye, and A. A. Tay, "Integration issues of lithium-ion battery into electric vehicles battery pack," *Journal of Cleaner Production*, vol. 113, pp. 1032–1045, 2016.

[20] G. Karimi and X. Li, "Thermal management of lithium-ion batteries for electric vehicles," *International Journal of Energy Research*, vol. 37, no. 4, pp. 13–24, 2012.

[21] Z. Rao and S. Wang, "A review of power battery thermal energy management," *Renewable and Sustainable Energy Reviews*, vol. 15, no. 9, pp. 4554–4571, 2011.

[22] L. Lu, X. Han, J. Li, J. Hua, and M. Ouyang, "A review on the key issues for lithium-ion battery management in electric vehicles," *Journal of Power Sources*, vol. 226, pp. 272–288, 2013.

[23] C. Zhao, W. Cao, T. Dong, and F. Jiang, "Thermal behavior study of discharging/charging cylindrical lithium-ion battery module cooled by channeled liquid flow," *International Journal of Heat and Mass Transfer*, vol. 120, pp. 751–762, 2018.

[24] a. a. Pesaran, "<Battery thermal models for hybrid vehicle simulations.pdf>," *Journal of Power Sources*, vol. 110, no. 2, pp. 377–382, 2002.

[25] H. Liu, Z. Wei, W. He, and J. Zhao, "Thermal issues about Li-ion batteries and recent progress in battery thermal management systems: A review," *Energy Conversion and Management*, vol. 150, no. August, pp. 304–330, 2017.

[26] A. Mills and S. Al-Hallaj, "Simulation of passive thermal management system for lithium-ion battery packs," *Journal of Power Sources*, vol. 141, no. 2, pp. 307–315,

2005.

[27] Q. Yue, C. He, M. Wu, and T. Zhao, "Advances in thermal management systems for next-generation power batteries," *International Journal of Heat and Mass Transfer*, vol. 181, p. 121853, 2021.

[28] B. Mondal, C. F. Lopez, A. Verma, and P. P. Mukherjee, "Vortex generators for active thermal management in lithium-ion battery systems," *International Journal of Heat and Mass Transfer*, vol. 124, pp. 800–815, 2018.

[29] I. A. Hunt, Y. Zhao, Y. Patel, and J. Offer, "Surface Cooling Causes Accelerated Degradation Compared to Tab Cooling for Lithium-Ion Pouch Cells," *Journal of The Electrochemical Society*, vol. 163, no. 9, pp. A1846–A1852, 2016.

[30] ANSYS Inc., *ANSYS Fluent Theory Guide (Release 18.0)*, 2017.

[31] C. Forgez, D. Vinh Do, G. Friedrich, M. Morcrette, and C. Delacourt, "Thermal modeling of a cylindrical LiFePO4/graphite lithium-ion battery," *Journal of Power Sources*, vol. 195, no. 9, pp. 2961–2968, 2010.

[32] T. S. Bryden, B. Dimitrov, G. Hilton, C. Ponce de León, P. Bugryniec, S. Brown, D. Cumming, and A. Cruden, "Methodology to determine the heat capacity of lithium-ion cells," *Journal of Power Sources*, vol. 395, pp. 369–378, 2018.

[33] J. Sun, G. Wei, L. Pei, R. Lu, K. Song, C. Wu, and C. Zhu, "Online internal temperature estimation for lithium-ion batteries based on Kalman filter," *Energies*, vol. 8, no. 5, pp. 4400–4415, 2015.

[34] T. Bergman and A. Lavine, *Fundamentals of heat and mass transfer*. John Wiley & Sons, Inc., eighth ed., 2017.

[35] D. Bernardi, "A General Energy Balance for Battery Systems," *Journal of The Electrochemical Society*, vol. 132, no. 1, p. 5, 1985.

[36] E. Jiaqiang, M. Yue, J. Chen, H. Zhu, Y. Deng, Y. Zhu, F. Zhang, M. Wen, B. Zhang, and S. Kang, "Effects of the different air cooling strategies on cooling performance of a lithium-ion battery module with baffle," *Applied Thermal Engineering*, vol. 144, no. August, pp. 231–241, 2018.

[37] Y. Kim, S. Mohan, J. B. Siegel, A. G. Stefanopoulou, and Y. Ding, "The estimation of temperature distribution in cylindrical battery cells under unknown cooling conditions," *IEEE Transactions on Control Systems Technology*, vol. 22, no. 6, pp. 2277–2286, 2014.

[38] A. Barai, G. H. Chouchelamane, Y. Guo, A. Mcgordon, and P. Jennings, "A study on the impact of lithium-ion cell relaxation on electrochemical impedance spectroscopy," *Journal of Power Sources*, vol. 280, pp. 74–80, 2015.

[39] D.-I. Stroe, M. Swierczynski, A.-I. Stroe, and S. Knudsen KÃ̧er, "Generalized characterization methodology for performance modelling of lithium-ion batteries," *Batteries*,

vol. 2, p. 37, Dec 2016.

[40] A. Barai, K. Uddin, W. D. Widanage, A. McGordon, and P. Jennings, "A study of the influence of measurement timescale on internal resistance characterisation methodologies for lithium-ion cells," *Scientific Reports*, vol. 8, no. 1, pp. 1–13, 2018.

[41] K. H. Kwon, C. B. Shin, T. H. Kang, and C.-S. Kim, "A two-dimensional modeling of a lithium-polymer battery," *Journal of Power Sources*, vol. 163, no. 1, pp. 151–157, 2006.

[42] P. V. Chombo and Y. Laoonual, "A review of safety strategies of a li-ion battery," *Journal of Power Sources*, vol. 478, p. 228649, 2020.

[43] A. Melcher, C. Ziebert, M. Rohde, and H. J. Seifert, "Modeling and simulation of the thermal runaway behavior of cylindrical Li-ion cells-computing of critical parameters," *Energies*, vol. 9, no. 4, pp. 1–19, 2016.

[44] X. Feng, M. Ouyang, X. Liu, L. Lu, Y. Xia, and X. He, "Thermal runaway mechanism of lithium ion battery for electric vehicles: A review," *Energy Storage Materials*, vol. 10, no. May 2017, pp. 246–267, 2018.

[45] R. Spotnitz and J. Franklin, "Abuse behavior of high-power, lithium-ion cells," *Journal of Power Sources*, vol. 113, no. 1, pp. 81–100, 2003.

[46] J. Xu, C. Lan, Y. Qiao, and Y. Ma, "Prevent thermal runaway of lithium-ion batteries with minichannel cooling," *Applied Thermal Engineering*, vol. 110, pp. 883–890, 2017.

[47] A. Hofmann, N. Uhlmann, C. Ziebert, O. Wiegand, A. Schmidt, and T. Hanemann, "Preventing Li-ion cell explosion during thermal runaway with reduced pressure," *Applied Thermal Engineering*, vol. 124, pp. 539–544, 2017.

[48] S. Wilke, B. Schweitzer, S. Khateeb, and S. Al-Hallaj, "Preventing thermal runaway propagation in lithium ion battery packs using a phase change composite material: An experimental study," *Journal of Power Sources*, vol. 340, pp. 51–59, 2017.

[49] P. T. Coman, E. C. Darcy, C. T. Veje, and R. E. White, "Modelling Li-Ion Cell Thermal Runaway Triggered by an Internal Short Circuit Device Using an Efficiency Factor and Arrhenius Formulations," *Journal of The Electrochemical Society*, vol. 164, no. 4, pp. A587–A593, 2017.

[50] P. T. Coman, S. Rayman, and R. E. White, "A lumped model of venting during thermal runaway in a cylindrical Lithium Cobalt Oxide lithium-ion cell," *Journal of Power Sources*, vol. 307, pp. 56–62, 2016.

[51] C. Qi, Y. Zhu, F. Gao, K. Yang, and Q. Jiao, "Mathematical model for thermal behavior of lithium ion battery pack under overcharge," *International Journal of Heat and Mass Transfer*, vol. 124, pp. 552–563, 2018.

[52] C. F. Lopez, J. A. Jeevarajan, and P. P. Mukherjee, "Experimental Analysis of Thermal

Runaway and Propagation in Lithium-Ion Battery Modules," *Journal of the Electro-chemical Society*, vol. 162, no. 9, pp. A1905–A1915, 2015.

[53] T. Wu, H. Chen, Q. Wang, and J. Sun, "Comparison analysis on the thermal runaway of lithium-ion battery under two heating modes," *Journal of Hazardous Materials*, vol. 344, pp. 733–741, 2018.

[54] D. Ouyang, Y. He, M. Chen, J. Liu, and J. Wang, "Experimental study on the thermal behaviors of lithium-ion batteries under discharge and overcharge conditions," *Journal of Thermal Analysis and Calorimetry*, vol. 132, no. 1, pp. 65–75, 2018.

[55] D. P. Abraham, E. P. Roth, R. Kostecki, K. McCarthy, S. MacLaren, and D. H. Doughty, "Diagnostic examination of thermally abused high-power lithium-ion cells," *Journal of Power Sources*, vol. 161, no. 1, pp. 648–657, 2006.

[56] A. Kvasha, C. Gutiérrez, U. Osa, I. de Meatza, J. A. Blazquez, H. Macicior, and I. Urdampilleta, "A comparative study of thermal runaway of commercial lithium ion cells," *Energy*, vol. 159, pp. 547–557, 2018.

[57] A. W. Golubkov, D. Fuchs, J. Wagner, H. Wiltsche, C. Stangl, G. Fauler, G. Voitic, A. Thaler, and V. Hacker, "Thermal-runaway experiments on consumer Li-ion batteries with metal-oxide and olivin-type cathodes," *RSC Advances*, vol. 4, no. 7, pp. 3633–3642, 2014.

[58] V. Ruiz, A. Pfrang, A. Kriston, N. Omar, P. Van den Bossche, and L. Boon-Brett, "A review of international abuse testing standards and regulations for lithium ion batteries in electric and hybrid electric vehicles," *Renewable and Sustainable Energy Reviews*, vol. 81, no. May 2017, pp. 1427–1452, 2018.

[59] Q. Wang, P. Ping, and J. Sun, "Catastrophe analysis of cylindrical lithium ion battery," *Nonlinear Dynamics*, vol. 61, no. 4, pp. 763–772, 2010.

[60] K. Shah, D. Chalise, and A. Jain, "Experimental and theoretical analysis of a method to predict thermal runaway in Li-ion cells," *Journal of Power Sources*, vol. 330, pp. 167–174, 2016.

[61] Y. Feng, Z Zhang, "Thermal runaway due to symmetry breaking in parallel- connected battery cells," *International journal of energy research*, vol. 38, no. 6, pp. 813–821, 2013.

[62] A. Smyshlyaev, M. Krstic, N. Chaturvedi, J. Ahmed, and A. Kojic, "PDE Model for Thermal Dynamics of a Large Li-Ion Battery Pack," in *American Control Conference*, (San Francisco, CA), pp. 959–964, IEEE, 2011.

[63] M. Parhizi, M. B. Ahmed, and A. Jain, "Determination of the core temperature of a Li-ion cell during thermal runaway," *Journal of Power Sources*, vol. 370, pp. 27–35, 2017.

[64] S. H. Strogatz, *Nonlinear Dynamics and Chaos: With Applications to Physics, Biology,*

Chemistry, and Engineering. CRC Press, 2nd ed., 2015.

[65] A. Pérez, M. Benavides, H. Rozas, S. Seria, and M. Orchard, "Guidelines for the Characterization of the Internal Impedance of Lithium-Ion Batteries in PHM Algorithms," *International Journal of Prognostics and Health Management*, vol. 9, pp. 1–10, 2018.

[66] W. Waag, S. Käbitz, and D. U. Sauer, "Experimental investigation of the lithium-ion battery impedance characteristic at various conditions and aging states and its influence on the application," *Applied Energy*, vol. 102, pp. 885–897, 2013.

[67] J. Huang, Z. Li, H. Ge, and J. Zhang, "Analytical Solution to the Impedance of Electrode/Electrolyte Interface in Lithium-Ion Batteries," *Journal of The Electrochemical Society*, vol. 162, no. 13, pp. A7037–A7048, 2015.

[68] Q. Wang, B. Jiang, B. Li, and Y. Yan, "A critical review of thermal management models and solutions of lithium-ion batteries for the development of pure electric vehicles," *Renewable and Sustainable Energy Reviews*, vol. 64, pp. 106–128, 2016.

[69] A. Jossen, "Fundamentals of battery dynamics," *Journal of Power Sources*, vol. 154, no. 2, pp. 530–538, 2006.

[70] A. Berrueta, A. Urtasun, A. Ursúa, and P. Sanchis, "A comprehensive model for lithium-ion batteries: From the physical principles to an electrical model," *Energy*, vol. 144, pp. 286–300, 2018.

[71] H. He, R. Xiong, and J. Fan, "Evaluation of lithium-ion battery equivalent circuit models for state of charge estimation by an experimental approach," *Energies*, vol. 4, no. 4, pp. 582–598, 2011.

[72] Y. Jiang and Z. Chen, "Adaptive temperature estimation for lithium-ion batteries," in *2019 IEEE 3rd International Electrical and Energy Conference (CIEEC)*, pp. 1066–1070, 2019.

[73] R. R. Richardson and D. A. Howey, "Sensorless battery internal temperature estimation using a kalman filter with impedance measurement," *IEEE Transactions on Sustainable Energy*, vol. 6, no. 4, pp. 1190–1199, 2015.

[74] S. Rath, E. Hoedemaekers, and S. Wilkins, "Core temperature estimation for a cylindrical cell battery module," in *2020 Fifteenth International Conference on Ecological Vehicles and Renewable Energies (EVER)*, pp. 1–10, 2020.

[75] A. Tulsyan, R. Bhushan Gopaluni, and S. R. Khare, "Particle filtering without tears: A primer for beginners," *Computers & Chemical Engineering*, vol. 95, pp. 130 – 145, 2016.

[76] M. S. Arulampalam, S. Maskell, N. Gordon, and T. Clapp, "A tutorial on particle filters for online nonlinear/non-gaussian bayesian tracking," *IEEE Transactions on Signal Processing*, vol. 50, no. 2, pp. 174–188, 2002.

[77] J. Liu and M. West, *Combined Parameter and State Estimation in Simulation-Based Filtering*, pp. 197–223. New York, NY: Springer New York, 2001.

[78] O. Cappe, S. J. Godsill, and E. Moulines, "An overview of existing methods and recent advances in sequential Monte Carlo," *Proceedings of the IEEE*, vol. 95, no. 5, pp. 899–924, 2007.

[79] A. Pervan and T. Murphey, "9 - algorithmic materials: Embedding computation within material properties for autonomy," in *Robotic Systems and Autonomous Platforms* (S. M. Walsh and M. S. Strano, eds.), Woodhead Publishing in Materials, pp. 197–221, Woodhead Publishing, 2019.

[80] N. Damay, C. Forgez, M. P. Bichat, and G. Friedrich, "A method for the fast estimation of a battery entropy-variation high-resolution curve âĂŞ Application on a commercial LiFePO4/graphite cell," *Journal of Power Sources*, vol. 332, pp. 149–153, 2016.

[81] Y. Zhang, W. Song, and Z. Feng, "An energy efficiency evaluation research based on heat generation behavior of lithium-ion battery," *Journal of the Electrochemical Society*, vol. 160, no. 11, pp. 1927–1930, 2013.

[82] Q. Li, C. Yang, and A. Pesaran, "Thermal runaway propagation modeling in lithium ion modules with and without PCM," tech. rep., International Battery Seminar & Exhibit, Florida, 2017.

[83] P. Pritchard and J. Mitchell, *Fox and McDonald's Introduction to Fluid Mechanics*. John Wiley & Sons, Inc., 9th ed., 2015.

[84] Atlanta, GA: ASHRAE, *ASHRAE HandbookâĂŤFundamentals*, ch. 36, Measurement and instruments. Atlanta, GA: ASHRAE, 2017.

[85] X. M. Xu and R. He, "Research on the heat dissipation performance of battery pack based on forced air cooling," *Journal of Power Sources*, vol. 240, pp. 33–41, 2013.

[86] L. H. Saw, Y. Ye, A. A. Tay, W. T. Chong, S. H. Kuan, and M. C. Yew, "Computational fluid dynamic and thermal analysis of Lithium-ion battery pack with air cooling," *Applied Energy*, vol. 177, pp. 783–792, 2016.

[87] J. Smith, M. Hinterberger, P. Hable, and J. Koehler, "Simulative method for determining the optimal operating conditions for a cooling plate for lithium-ion battery cell modules," *Journal of Power Sources*, vol. 267, pp. 784–792, 2014.

[88] Q. Xia, Z. Wang, Y. Ren, B. Sun, D. Yang, and Q. Feng, "A reliability design method for a lithium-ion battery pack considering the thermal disequilibrium in electric vehicles," *Journal of Power Sources*, vol. 386, no. November 2017, pp. 10–20, 2018.

[89] D. C. Erb, S. Kumar, E. Carlson, I. M. Ehrenberg, and S. E. Sarma, "Analytical methods for determining the effects of lithium-ion cell size in aligned air-cooled battery packs," *Journal of Energy Storage*, vol. 10, pp. 39–47, 2017.

[90] K. Chen, S. Wang, M. Song, and L. Chen, "Configuration optimization of battery pack in parallel air-cooled battery thermal management system using an optimization strategy," *Applied Thermal Engineering*, vol. 123, pp. 177–186, 2017.

[91] X. Lin, A. Stefanopoulou, J. Siegel, and S. Mohan, "Temperature estimation in a battery string under frugal sensor allocation," in *Proceedings of the ASME 2014 Dynamic Systems and Control Conference*, vol. 1, 10 2014.

[92] J. Reyes-Marambio, F. Moser, F. Gana, B. Severino, W. R. Calderón-Muñoz, R. Palma-Behnke, P. A. Estevez, M. Orchard, and M. Cortés, "A fractal time thermal model for predicting the surface temperature of air-cooled cylindrical Li-ion cells based on experimental measurements," *Journal of Power Sources*, vol. 306, pp. 636–645, 2016.

[93] W. Chen, H. Sun, X. Zhang, and D. Koroǎak, "Anomalous diffusion modeling by fractal and fractional derivatives," *Computers & Mathematics with Applications*, vol. 59, no. 5, pp. 1754 – 1758, 2010. Fractional Differentiation and Its Applications.

[94] M. Sen, *Analytical heat transfer*. University of Notre Dame, 2017.

[95] G. Li and S. Li, "Physics-based CFD simulation of lithium-ion battery under the FUDS driving cycle," *ECS Transactions*, vol. 64, no. 33, pp. 1–14, 2015.

[96] Y. Kim, J. B. Siegel, and A. G. Stefanopoulou, "A computationally efficient thermal model of cylindrical battery cells for the estimation of radially distributed temperatures," in *2013 American Control Conference*, pp. 698–703, IEEE, 2013.

[97] S. S. Madani, M. Swierczynski, and S. Kær, "Cooling simulation and thermal abuse modeling of lithium-ion batteries using the Newman, Tiedemann, Gu, and Kim (NTGK) model," *ECS Transactions*, vol. 81, pp. 261–270, 12 2017.

[98] W. Allafi, C. Zhang, K. Uddin, D. Worwood, T. Q. Dinh, P. A. Ormeno, K. Li, and J. Marco, "A lumped thermal model of lithium-ion battery cells considering radiative heat transfer," *Applied Thermal Engineering*, vol. 143, pp. 472–481, 2018.

[99] F. Bahiraei, M. Ghalkhani, A. Fartaj, and G.-A. Nazri, "A pseudo 3D electrochemical-thermal modeling and analysis of a lithium-ion battery for electric vehicle thermal management applications," *Applied Thermal Engineering*, vol. 125, pp. 904–918, 2017.

[100] S. Madani, E. Schaltz, and S. Knudsen Kær, "Review of parameter determination for thermal modeling of lithium ion batteries," *Batteries*, vol. 4, p. 20, Apr 2018.

[101] X. Gao, Y. Ma, and H. Chen, "Active thermal control of a battery pack under elevated temperatures," *IFAC-PapersOnLine*, vol. 51, no. 31, pp. 262–267, 2018.

[102] L. Calearo, A. Thingvad, and M. Marinelli, "Modeling of battery electric vehicles for degradation studies," in *2019 54th International Universities Power Engineering Conference (UPEC)*, pp. 1–6, 2019.

[103] E. Gümüǎsu, Ö. Ekici, and M. Köksal, "3-D CFD modeling and experimental test-

ing of thermal behavior of a Li-Ion battery," *Applied Thermal Engineering*, vol. 120, pp. 484–495, 2017.

[104] A. Celik, H. Coban, S. GÃúÃğmen, M. Ezan, A. Goren, and A. Erek, "Passive thermal management of the lithiumâĂŘion battery unit for a solar racing car," *International Journal of Energy Research*, vol. 43, pp. 3681–3691, 04 2019.

[105] Y. Li, Z. Zhou, and W.-T. Wu, "Three-dimensional thermal modeling of li-ion battery cell and 50 V Li-ion battery pack cooled by mini-channel cold plate," *Applied Thermal Engineering*, vol. 147, pp. 829–840, 2019.

[106] T. Wang, K. J. Tseng, and J. Zhao, "Development of efficient air-cooling strategies for lithium-ion battery module based on empirical heat source model," *Applied Thermal Engineering*, vol. 90, pp. 521–529, 2015.

[107] X. Na, H. Kang, T. Wang, and Y. Wang, "Reverse layered air flow for Li-ion battery thermal management," *Applied Thermal Engineering*, vol. 143, no. July, pp. 257–262, 2018.

[108] I. Ikpotokin and C. Osueke, "Heat transfer and fluid flow characteristics study for in-line tube bank in cross-flow," *International Journal of Mechanical and Mechatronics Engineering*, vol. 14, pp. 93–105, 01 2014.

[109] T. D. Hatchard, "Importance of Heat Transfer by Radiation in Li-Ion Batteries during Thermal Abuse," *Electrochemical and Solid-State Letters*, vol. 3, no. 7, p. 305, 2000.

[110] M. Karp, "Thermal runaway initiation methods for lithium batteries," Tech. Rep. DOT/FAA/TC-20/12, U.S. Department of Transportation, Federal Aviation Administration, New Jersey, July 2019.

Annexed: Implemented codes

MATLAB Code to read temperature from Arduino DAQ

```matlab
1  %%%%%%%%%%%%%%%%%%%%%%%%%%%%%%%%%%%%%%%%%%%%%%%%%%%%%%%%%%%%%%%%%%%%%%%
2  % Temperature reading from two  sensor by Arduino eacht 1 second    %
3  % Programm stops when the red STOP buttom is clicked               %
4  % Input: Number of sensors (Ns); samples to save (Ns), name of file %
5  % Output vector: 'Temperatures'                                    %
6  %%%%%%%%%%%%%%%%%%%%%%%%%%%%%%%%%%%%%%%%%%%%%%%%%%%%%%%%%%%%%%%%%%%%%%%
7
8  clc
9  close all
10 clear all
11 question='Enter the name of the experiment\n';
12 name=input(question,'s');                 %Name fo measurement
13 Ns=2;                                     %Number of sensors
14 Fs=1;                                     %Sample time
15 N=3600;                                   %Number of samples to save
16 a2=arduino('COM3'); %3                    %Select COM port for Arduino device
17 line1 = line(nan,nan,'color','red');   %Line for the 1st sensor A1
18 line2 = line(nan,nan,'color','blue');  %Line for the 2dn sensor A2
19 grid;                                     %Activate grid plot
20 ylim([15 55]);                            %Plot limits y axis
21 i=0;                                      %Counter
22 Stop=1;                                   %Stop
23
24 %Control Buttom for stopping
25 uicontrol('Style','Pushbutton','String','STOP','Callback','Stop=0;',...
26          'BackgroundColor','r','FontWeight','bold')
27
28 t=linspace(0,(N-1)/Fs,N);
29
30 tic
31 Temp_exp=zeros(N,Ns);                      %Create matrix containing ...
       temperaturesÂt'
32 while Stop
33     if toc>1/Fs
34     tic;
35 %Read voltages from devices
36 V1=readVoltage(a2,'A1');
37 V2=readVoltage(a2,'A2');
38
39 %Convert voltage to temperature
```

```matlab
40  T1=Measured_temp(V1)-0.2;   %0.2 is to calibrate sensor
41  T2=Measured_temp(V2)-0.3;   %0.3 is to calibrate sensor
42
43
44  %Display measured temperatures
45  Online_temperature=[T1 T2]
46  Temp_exp(i+1,:)=Online_temperature;    %save the measured temperatures ...
        in matrix y
47
48  %Real time plot of some sensors
49  x1=get(line1,'xData');
50  y1=get(line1,'yData');
51  x2=get(line2,'xData');
52  y2=get(line2,'yData');
53
54
55  x1=[x1 i]; y1=[y1 T1];
56  x2=[x2 i]; y2=[y2 T2];
57
58  i=i+1;
59  set(line1, 'xData',x1,'yData',y1);
60  set(line2, 'xData',x2,'yData',y2);
61
62  legend('Tamb,int','Tcell')
63  xlabel('Time s'); ylabel('Temperature ÂřC')
64  drawnow
65
66  end
67  end
68  save(name,'Temp_exp')
```

C Code for a UDF to estimate heat generation at 1C-rate in Fluent

```c
/**************************************************************************
UDF for time dependent volumetric heat generation of 26650 cell
Heat generation at 1.0C for a fresh battery
Ohmic resistance is taken as a mediuam value, 24ÅřC
**************************************************************************/
#include "udf.h"

//0-1s        Qgen(t) = p0*t
#define p1 2.809e+04

//1s-3600
//a0 + a1*cos(x*w) + b1*sin(x*w) +
//a2*cos(2*x*w) + b2*sin(2*x*w) + a3*cos(3*x*w) + b3*sin(3*x*w) +
//a4*cos(4*x*w) + b4*sin(4*x*w) + a5*cos(5*x*w) + b5*sin(5*x*w) + ...

#define a0 2.92e+04
#define a1 6340
#define b1 -6126
#define a2 -2859
#define b2 -3851
#define a3 -2273
#define b3 -1828
#define a4 -2095
#define b4 1141
#define a5 -250.6
#define b5 1503
#define a6 -5.554
#define b6 75.5
#define a7 266.2
#define b7 371
#define w 0.00119

DEFINE_SOURCE(Qg_4Ajr3,c,t,dS,eqn)
{
    real source;
    real Qgen;
    real time;
    real derivative;
    time = CURRENT_TIME;       //taking time value

    if (time <= 1){
        Qgen = p1*time;

    }

    else if ((time > 1) && (time <= 3600)){
        Qgen=a0 + a1*cos(time*w) + b1*sin(time*w) + a2*cos(2*time*w) + ...
            b2*sin(2*time*w)
        + a3*cos(3*time*w) + b3*sin(3*time*w) + a4*cos(4*time*w) + ...
            b4*sin(4*time*w)+
        a5*cos(5*time*w)+ b5*sin(5*time*w)+ a6*cos(6*time*w)+ ...
            b6*sin(6*time*w)+
```

```
50          a7*cos(7*time*w)+b7*sin(7*time*w);
51
52      }
53      else {
54          Qgen = 0.0;
55      }
56      source = Qgen;
57      dS[eqn] = 0.0;
58
59      return source;
60  }
```

Optimizer to find cell parameters

```matlab
1  %% Execute the main script.-
2  clear
3  clc
4  tic
5
6  Eo = C1_Init;
7
8  % Load datas 1.-
9  load('DTp5.mat');                    % Experimental Temperature data
10 DTp5=DTp5(1:2700);                   % Select time interval
11 Ts_exp = DTp5 + Eo.Tamb;             % Exp. temperature at surface of ...
       the cell
12
13 load('Pulse5_N21P1.mat');            % Load temperature by current pulses
14 Tamb=(Pulse5_N21P1(1:2700,1));
15
16 % -------------------------------------------------------------------------
17 load('Ip5.mat')                      % Current profile
18 Ip5=Ip5(1:2700);
19 Eo.SOC1 = 1-cumsum(Ip5*1/(3600*Eo.C0)); % State of charge (Counting ...
       Coulomb)
20 Eo.I1   = Ip5;
21 % -------------------------------------------------------------------------
22
23 % Fitting
24
25 [A,resnorm,residual,exitflag,output,lambda,jacobian] = ...
       lsqcurvefit(@(A,t) ...
       C2_lumped(A,t,Eo),Eo.A0,Eo.tpo,Ts_exp,Eo.lb,Eo.ub,Eo.options);
26
27 Eo.outP = 1;
28 FitData = C2_lumped(A,Eo.tpo,Eo);
29
30 y1      = FitData(:,1);              % Temperature of the cell
31 A                                    % Vector of results
32 Cp = A(1)/Eo.mass                    % Heat capacity
33 err_f = sum(((DTp5+Eo.Tamb) - y1(1:end,1)).^2) ./ size(y1,1)
34 epsilon=0.9;
35 sigma=5.67e-8;
36 toc
37
38 % Plot results----------------------------------------------------------
39 figure
40 plot(Ts_exp-273,'color',rgb('Navy'),'LineWidth',1.5); hold on
41 plot(y1-273,'color',rgb('Red'),'LineWidth',1.5)
42 plot(Tamb,'color',rgb('Black'),'LineWidth',1.5)
43 hold off
44
45 leg=legend('Measured temperature','Fitted temperature','Ambient ...
       temperature','location','northwest');
46 xlabel('Time [s] '); ylabel('TemperatureÂt')
```

```
1  %% Initialize.-
2
3  function Eo = C1_Init()
4
5  % To define a structure.-
6  Eo = struct;
7
8  tdis     = 2699;                          % Discharging time
9  Eo.Tamb  = 23.3+273;                      % Ambient temperature
10
11 Eo.Asurf = pi*0.026*0.065+(2*pi*0.013^2); % Cell Surface area
12
13 Eo.A0    = [130; 2.5];                    % Initial condition of parameters
14 Eo.lb    = [100 1];                       % [Cp Rin] Lower bound (Evoid ...
       0->diverges)
15 Eo.ub    = [140 5];                       % Upper bound of parameters
16
17
18 % From experiment
19 Eo.tpo   = 0:1:tdis;                      % dischargig time
20
21 % Set options to avoid stop the curvefit before to reach optim parameters.-
22 Eo.options = optimoptions('lsqcurvefit');
23 Eo.options.MaxIterations = 1000;          % Default 400
24 Eo.options.MaxFunctionEvaluations = 5000; % Default 200
25 % ----------------------------------------------------------------------
26
27 Eo.h      = 1;                            % Step for Runge Kutta ...
       (RK4)solver
28 Eo.tspan  = [0 tdis];                     % Time span for RK4 solver
29 Eo.tspan2 = (Eo.tspan(1):Eo.h:Eo.tspan(2));
30 Eo.C0     = 4.368;                        % Capacity of the cell Ah
31 Eo.y0     = [Eo.Tamb];                    % Cell temp. at t=0
32 % ----------------------------------------------------------------------
33 Eo.R    = 0.058;         % Resistance of the battery [ohm]  0.06391;
34 Eo.mass = 0.0875;        % mass of the cell [kg]
35 % ----------------------------------------------------------------------
36 %Eo.outP = 0;                             % 0: Resuelve el ...
       optimizador. 1: Entrega dos Temperaturas.-
```

```
1  % Function for a lumped model
2
3  function S = C2_lumped(A,t,Eo)
4
5  Eo.A = A;
6  [time, T] = C3_RK(@C4_DifEq, Eo.tspan, Eo.y0, Eo.h, Eo);
7  %if Eo.outP == 0
8      %S = T(:,1);
9  %else
10     S = T;
11 %end
12 end
```

90

```matlab
% Differential equation for cell tememperature
function dy = C4_DifEq(t,y,Eo)

SOC = interp1(Eo.tspan2,Eo.SOC1,t);
I   = interp1(Eo.tspan2,Eo.I1,t);

dydt    = zeros(1,1);
dydt(1)= (Eo.Tamb - y(1))/(Eo.A(1)*(Eo.A(2)+14.14))+...
    (Resistance21ct(SOC,y(1))*I^2-I*y(1).*EntropyfunN21(SOC)*1e-3)*14.14/...
    (Eo.A(1)*(Eo.A(2)+14.14));

dy      = dydt;

end
```

```matlab
%Cell entropy
function y = C5_Entropy(SOC)

SoC   = 0:0.1:1;
Smean = [-0.1467 -0.0143 0.0257 0.1890 0.1690 0.1557 0.039 0.031 0.0303...
         0 -0.0093];
if ((SOC≥0) && (SOC≤1))
    y = interp1(SoC,Smean,SOC,'spline');
else
    disp('Error: SOC must be beetween [0 1]');
end
```